Fabrication of Zeolite MFI Membranes on Low Cost Polymer Supports

A Dissertation
SUBMITTED TO THE FACULTY OF
UNIVERSITY OF MINNESOTA
BY

Han Zhang

IN PARTIAL FULFILLMENT OF THE REQUIREMENTS
FOR THE DEGREE OF
DOCTOR OF PHILOSOPHY

Advised by Prof. Michael Tsapatsis and Prof. Christopher W. Macosko

July 2017

Acknowledgements

I want to sincerely thank Prof. Michael Tsapatsis and Prof. Christopher W. Macosko for the opportunity to study in their groups. I really appreciate the trust from Michael when I approached him to express my research idea for this challenging project. His meticulous and cautionary attitude to research has shaped and guided my research into the right direction. His continuous support and help, especially after long time failures, took me into the correct pathway. Chris has been a great mentor for my research. He is always ready to help, and especially, his words cheered me up when I was down. I also want to thank Prof. Alon McCormick, Prof. Paul Dauenhauer, and Prof. Ilja Siepmann for agreeing to serve on my committee.

I am very grateful to have the opportunity to work with the colleagues in Tsapatsis and Macosko groups. Visiting scholars Prof. Qiang Xiao, Prof. Xianghai Guo and Prof. Najun Li have made significant contribution to my research. Qiang's experiments in piranha solution treatment was the pivot to the open-pore nanosheets. Xianghai and Najun have made a lot of efforts in multilamellar MFI synthesis and provided me valuable materials. Dr. Neel Rangnekar helped me a lot for membrane tests. Dr. Kumar Varoon Agraval and Dr. Berna Topuz have taught me how to synthesize and characterize MFI membranes and provided valuable discussions. Prashant Kumar has spent long time in high resolution TEM imaging of MFI nanosheets. Xuekui Duan has worked with me for fabrication and characterization of PBI hollow fibers. Industrial consultant Dr. Frank Onorato has provided valuable suggestion for PBI membrane fabrication. Dr. David Giles has provided help with polymer sample characterization and valuable discussion. June Xue has provided polystyrenes for zeolite exfoliation. Undergraduate students Levi Paul and Ngan Tran have worked on the flat polymer support fabrication. Undergraduate student David Lundberg has contributed significantly to the study of melt compounding exfoliation of layered zeolites. Dr. Donglin Tang, Dr. Zaifei Wang, Dr. Luca Martinetti, Dr. Limin Ren, Dr. Qiang, Dr. Mi Young Jeon, Nitish Mittal, Dr. Garrett Swindlehurst, Dr. Xueyi Zhang, Dr. Bahman Elyassi, Dr. Dorita Politi, Dr. Zhendong Liu, and Dr. Xiaoli Ma have provided important suggestions for my research. I would also want to

thank the University of Minnesota Characterization staff including Dr. Nick Seaton, Dr. Bing Luo and Dr. Jason Myers for their help with sample characterization. I also would like to express my appreciation to the CEMS staff Julie Prince, Teresa Bredahl, Daniel Williams, Susan Wermager, Ted Butler, and Mary Kosowski for their kind help.
I also want to express my gratitude to Guanda Wu, Bingzhe Li, Qiannan Li, Jing Liu, Bin Li, Peng Liu, Jiaming Zheng who have spent joyful time with me especially in the beginning when I came to US. At last, but definitely not the least, my parents, who are always my supporters, have provided encouragement and blessings which helped me step out of the difficulties.

Dedication

To my family and friends

Abstract

About 10~15% of total energy consumption in US is attributed to energy intensive chemical separation processes, such as distillation. The alternative membrane-based separation could save up to 90% energy consumption with outstanding separation performance. Zeolite MFI membranes have been demonstrated for xylene and butane isomer separations with high separation factors and permeances. However, high cost and scale-up difficulty prevent the commercialization of MFI membranes in industries.

This dissertation attempts to explore the methods for MFI membranes supported on low cost polymer supports. The major challenge is the stability of polymer support during the detemplation treatment of the MFI membrane after secondary growth. Two mild detemplation methods, thermal treatment at 280 °C and UV/ozone treatment, were identified with sub-100 nm MFI membranes supported on quartz supports. These two methods were then applied to MFI membranes supported on mesh-polyethersulfone (PES) supports and MFI membranes supported on mesh-polybenzimidazole supports. However, cracks formed after the treatments due to the damage of polymer layer by UV light and the mismatch of linear thermal expansion co-efficient, respectively.

Another approach, which utilizes the open-pore MFI nanosheets, have been demonstrated. The organic structure directing agents (OSDA) occluded inside the micropores of nanosheets were removed by successive piranha solution treatment, while the crystallinity and morphology were still preserved that confirmed by X-ray diffraction(XRD), transmission electron microscopy (TEM), scanning electron microscopy (SEM), and gas adsorption. The simple deposition of such open-pore MFI nanosheets on porous PBI support, without the need of secondary growth and detemplation, exhibited *n*-/*iso*-butane ideal selectivity of 5.4 with *n*-butane permeance of 3.5×10^{-7} mol/m^2-s-Pa.

In addition, the nanosheet exfoliation yield was significantly improved by an oligomeric polystyrene resin. Ultrafiltration polymer hollow fibers were also prepared as suitable supports for nanosheet coating.

Table of Contents

List of Tables

List of Figures

Chapter 1. Introduction to zeolites and zeolite membranes

1.1 Zeolites and zeolite membranes

Zeolites are microporous aluminosilicate minerals consisting of inter-connected tetrahedra of silica (SiO_4) and alumina (AlO_4). As of June 2017, there are 232 unique frameworks identified by International Zeolite Association.[1] Zeolite crystals have uniformly and precisely defined pores and channels on the scale of molecular size ranging from ca. 0.3~1.5 nm, which could accommodate guest molecules in their frameworks with shape and size selectivity. This molecular sieving property, together with their acidic forms, make them ideal materials for adsorptions, ion-exchanges, catalytic reactions, and membrane separations.[2,3]

Membrane-based separations are important because they provide an energy efficient, sustainable route to separate chemicals compared with traditional energy-intensive separation methods such as distillation, crystallization, and pressure swing adsorption. As indicated in **Figure 1.1**, industrial energy consumption accounts for 32% of the total energy consumption in US, and about 45~55% of industrial energy consumption is from chemical separation processes.[4] Membrane-based separation processes, on the other hand, would use 90% less energy than distillation.[5] Zeolite membranes, in contrast to polymer membranes or mix matrix membranes, possess superior thermal and mechanical properties, as well as ultra-high separation factors relying on their molecular sieving properties. Over the past two decades, zeolite membranes have been demonstrated the ability for gas separation (CO_2[6–8], H_2[9–12], butane isomers[13–15]), solvent dehydration[16,17], alcohols from water[18,19], and organic vapors[20–22].

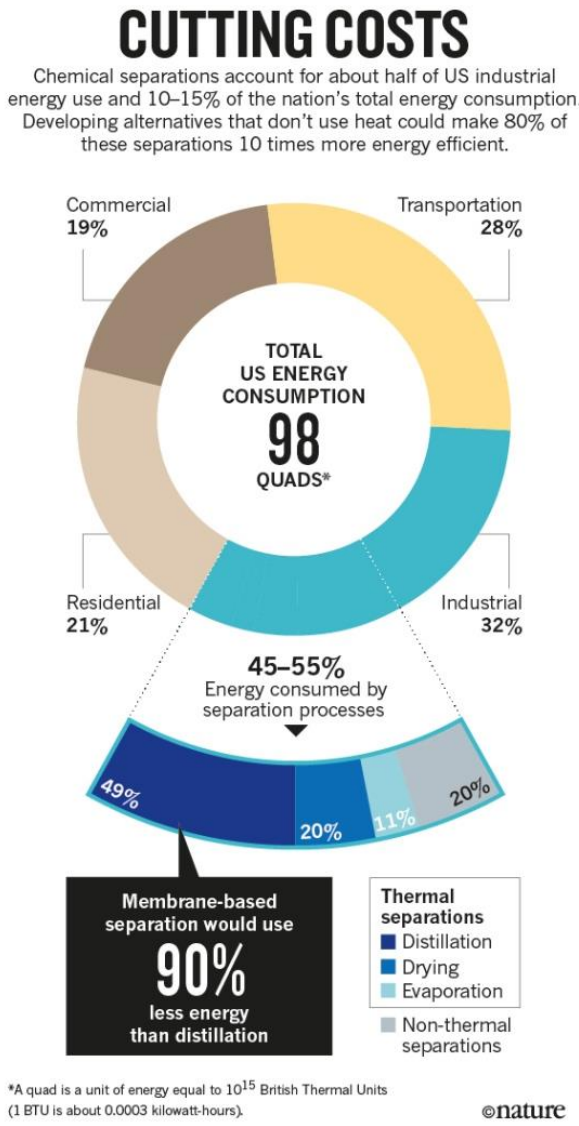

Figure 1.1. The energy consumption of US. This image is adapted from reference 5.

Generally, zeolite membranes were made on porous ceramic supports by the so-called seeded secondary growth method. **Figure 1.2** illustrated the microstructure control by crystal-shape design, deposition, and growth using crystal-shape modifier.[23] The seed crystals could be synthesized by either direct (bottom-up) or top-down synthetic approaches. For direct synthesis approach, typically, a synthesis gel containing

silica/alumina source, an organic structure directing agent (OSDA), and water is formed and crystalized under hydrothermal conditions. The shape of zeolite crystals with favorable growth in certain directions could be controlled by the type of OSDA[24] and the hydrothermal growth conditions[23]. Top-down approach for zeolite crystals involves the breakdown of aggregates or assembly of zeolite crystals to obtain smaller sized crystals. Uniformly shaped MFI crystals with tunable size from 10 to 40 nm were synthesized within porous 3Dom carbon and disassembled by a fragmentation method for thin zeolite membrane fabrication.[25,26] Another top-down approach example is the exfoliation of multilamellar MFI zeolite by polymer melt-compounding[21,27] or piranha solution treatment[28]. The exfoliated nanosheets have been used as promising seeds for ultra-thin sub-100 nm zeolite membranes for gas separation.[13,21]

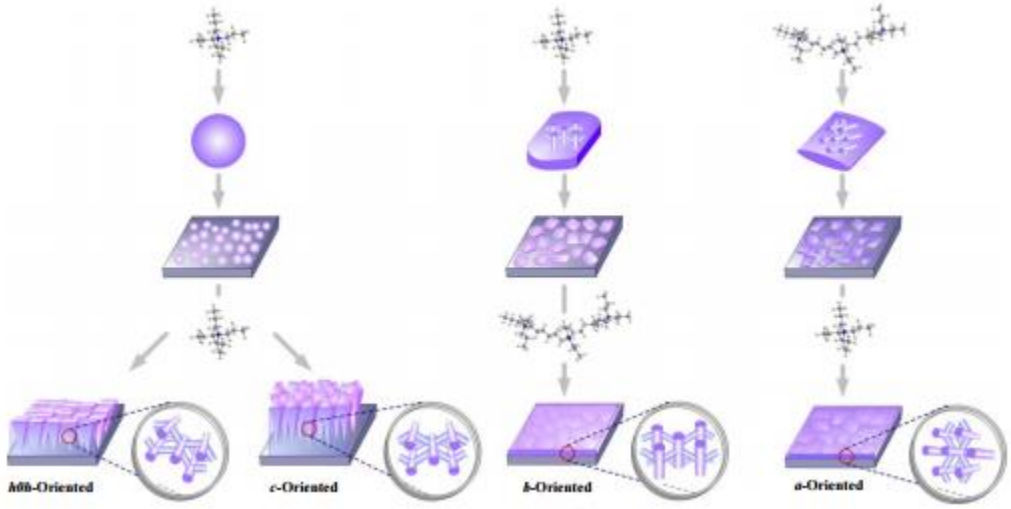

Figure 1.2. Scenarios of microstructure control by crystal-shape design, deposition, and growth using crystal-shape modifiers. Adapted from reference 23.

The seed crystals could be assembled onto the substrate surface via various techniques including manually rubbing and self-assembly[29], Langmuir-blodgett and Langmuir-

Schaefer assemble[30,31], and hot dip coating. Manually rubbing and self-assembly usually rely on the substrate surface modification with functional groups to provide sufficient bonding between substrate and seed crystals. High coverage, close packing, uniform orientation monolayer assembly of aminopropyl-tethering zeolite-A crystals were coated on 3-(2,3-epoxypropoxy)propylsilyl (EP)-coated glass plates, via the amine-alcohol linkage formation.[32] Langmuir-Schaefer deposition of 3 nm thick MFI nanosheet on silicon wafer was demonstrated.[31] The coated nanosheets were then subjected to secondary growth to obtain sub-12 nm thin film, which was the thinnest intergrown MFI film reported.

After seeding on support, typically, a hydrothermal secondary growth was performed for seed crystal growth and gap closing to eliminate the non-zeolitic diffusion pathways in the film. The gel-based secondary growth was widely used, in which the seeded support was immersed in a gel containing silica/alumina source, OSDA (or not), and water. Except some zeolite membranes which do not require OSDA during the growth, the structure and concentration of OSDA are crucial for the microstructure of the membranes.[20,33] Gel-based secondary growth usually required complex steps (gel preparation, waste handling). Recently, gel-less secondary growth for oriented MFI membranes have been developed by Yoon's group.[34] This method utilizes a layer of 50 nm silica spheres coated on the support surface as silica source. The OSDA was introduced into the support by soaking the seeded support in a dilute aqueous OSDA solution. The support was then put into an autoclave for thermal treatment. This method is much simpler, results in less wastes, preserves the orientation of the seed layer, and

thus favorable for large scale fabrication.

1.2 Exfoliated MFI nanosheets

Dispersible exfoliated zeolite nanosheets of silicalite-1 (all silica form MFI zeolite) and ITQ-2 with nanometer sized thickness and high aspect ratio were synthesized by the Tsapatsis group in 2011.[21] These nanosheets were fabricated starting from their corresponding layered precursors. The multilamellar MFI zeolite were synthesized with a special OSDA consisting of di-quaternary ammonium head groups and a long chain alkyl hydrophobic tail.[35] The di-quaternary head groups directed the formation of MFI framework, while the long hydrophobic tail prevented the thickening of the zeolite crystal, resulting in high aspect ratio MFI nanosheets assembled together by the Van der Waals force between the alkyl tails. The exfoliated silicalite-1 nanosheets were then obtained via melt compounding of multilamellar silicalite-1 and polystyrene between 120 and 200 °C followed by dissolution of the nanocomposite in toluene for polymer removal by washing. Low magnification transmission electron microscopy (TEM) in **Figure 1.3** reveals the flake-like morphology of the exfoliated nanosheets with high aspect ratio. The uniform contrast of the nanosheets demonstrates the uniform thickness, while the darker areas are assigned to the overlapping of the neighboring nanosheets. Despite that the lattice fringes are not easily visible by high-resolution TEM image in **Figure 1.3B**, the electron diffraction (ED) proves high crystallinity of the nanosheets. Furthermore, atomic force microscopy (AFM) results show that the thickness of the silicalite-1 nanosheets with SDA imbedded in the lamellae is around 3.2 nm.

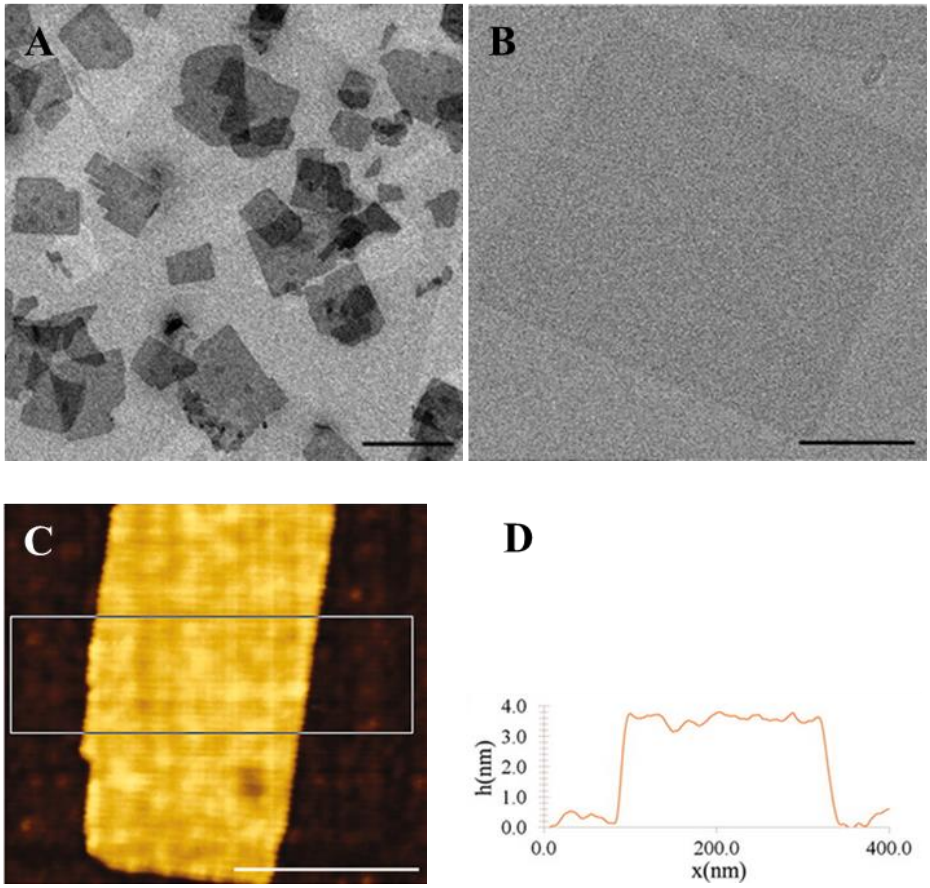

Figure 1.3. Low magnification TEM (A) and HRTEM (B) of exfoliated silicalite-1 nanosheets. AFM (tapping mode) topographical images of silicalite-1 nanosheets (C). The average step-height (h) data of the area highlighted in (C) are plotted in (D). Scale bars: (A) and (C) 200 nm, (B) 50 nm. Adapted from reference 21.

The obtained zeolite nanosheet suspension was then purified by density gradient centrifugation (DGC) to remove the non-exfoliated particles which are detrimental for thin membrane growth.[36] The purified nanosheets were further utilized as building blocks for the formation of *b*-oriented, ultra-thin zeolite MFI membranes that exhibited recorded high permeances for xylene and butane isomers.[13]

1.3 Limitations of zeolite membrane commercialization

Although almost three decades passed since the first report of zeolite membrane[37], only a few examples exist for large scale fabrication and application.[38–41] The limitations regarding the commercialization of zeolite membranes include complex and high cost processing steps (seeding, secondary growth, high temperature calcination), high cost materials (OSDA, ceramic supports), scale-up difficulties, and poor reproducibility.[42] The cost for a zeolite membrane module in the year 2000 were about $3000 per square meter of installed membrane area and most of the cost was attributed to the module, while only 10-20% to the zeolite membrane layer itself.[43] Additionally, the current methods for inorganic support fabrication are not practical to scale-up, which involve complicated multi-stage processes and surface treatments. This also contributes to the high cost of traditional zeolite membranes. Another concern is the deposition methods of zeolite membranes. Cracks are usually formed during the hydrothermal intergrowth of zeolite seeds due to the residual stresses or stress created during the calcination step due to the mismatch of thermal expansion coefficients between zeolite layer and support. In addition, the current membrane fabrication technologies result in zeolite membranes with thicknesses of several micrometers, which decrease the permeate flux and consequently large membrane area is required to meet the industrial production rates. Such thick zeolite membranes originate from the surface roughness of conventionally used supports and big size zeolite seeds.

1.4 Thesis outline

This dissertation describes the attempt for low cost and scalable MFI zeolite membranes

supported on polymer supports. Chapter 2 discusses the alternative mild detemplation methods for MFI membranes with membranes supported on quartz supports as models to study the treatment conditions and efficiency. Chapter 3 reports the MFI membrane growth on polymer supports and the following mild detemplation treatments. Chapter 4 describes the fabrication of open-pore MFI nanosheets and their deposit on polybenzimidazole support as selective membrane without the need of secondary growth. Chapter 5 discusses the fabrication of polybenzimidazole ultrafiltration hollow fibers. Chapter 6 reports the nanosheet exfoliation with improved yield via oligomeric polystyrene at low temperature and the clay exfoliation by polystyrene melt compounding with various molecular weights and viscosities.

Chapter 2. Mild detemplation of sub-micron silicalite-1 membranes for xylene and butane isomer separation

*To be submitted.

2.1 Introduction

Membrane separation is an energy-efficient and environmentally friendly technique, especially when applied for the separation of close-boiling point mixtures and organic isomers. Zeolite membranes, possessing precisely controlled molecular-size micropores, excellent mechanical, thermal and chemical stabilities, have attracted extensive interests[42]. ZSM-5 (structure type MFI) membranes are widely studied due to their 5.5 Å straight channels which are applicable for the chemical separations in petrochemical industries[44]. The ZSM-5 membranes have been proved to be selective for xylene isomer, butane isomer, water/alcohol, and other hydrocarbon separations.

Although more than two decades passed since the first report[37], the large-scale commercialization of zeolite membranes is still unsuccessful. There is only one report for the large-scale pervaporation plant using tubular-type module with zeolite NaA membranes for the continuous dehydration of water/organic solvents[45]. One of the key limitations regarding the commercialization of zeolite membranes is the high cost zeolite membrane module. The cost for a zeolite membrane module in the year 2000 was about $3000 per square meter installed membrane area and most of the cost was attributed to the module, while only 10-20% to the zeolite membrane layer itself.[43] The traditional inorganic supports contribute largely to the high module cost due to the complex fabrication processes and their difficulty to scale-up. On the other hand, due to the low cost and facile scale-up process, porous polymer flat sheets or hollow fibers are

alternative supports for the commercialization of the zeolite membranes. However, calcination at high temperatures up to 450 °C is a traditional way to activate the zeolite membranes, which precludes the application of polymer supports. In addition, cracks/defects are easily formed during the high temperature calcination treatment due to the mismatched linear thermal expansion coefficients between zeolite membrane layer and the support. Thus, it is highly demanded to investigate alternative mild conditions for template removal from the zeolite membranes.

Previous study of thermal detemplation of micron-size high silica ZSM-5 crystals demonstrated the partial detemplation at 280 °C for 24 h[46]. However, to the best of our knowledge, the low temperature calcination has never been reported for zeolite MFI membranes. Another mild detemplation method is UV/ozone treatment, which has been proved as an efficient way to remove the templates from the MFI film[47] and MFI powder crystals[48]. The micron-size MFI membrane was detemplated by UV/ozone treatment to avoid the cracks formation.[49] But the authors only reported the nitrogen and trimethylbenzene permeances of the treated membrane. Here, with the *b*-oriented MFI thin membrane as the model, we studied two mild detemplation methods: (i) low temperature thermal and (ii) UV/ozone treatment. The corresponding xylene isomer and butane isomer separation performances were investigated to evaluate the efficiency of template removal.

2.2 Experimental

2.2.1 Membrane fabrication

The detailed procedures of exfoliated nanosheets, quartz supports and membrane

synthesis were according to our previous report.[13] Typically, the sintered silica fiber (SSF) supports were made by sintering of the powdered silica fibers (quartz wool, purchased from Technical Glass Products), followed by surface rubbing with 500 nm and 50 nm Stöber silica spheres.[50] The purified MFI-nanosheet suspension in *n*-octanol[36] was used as MFI seed suspension to coat the SSF support via vacuum filtration. The MFI-nanosheets coated on SSF support were dried at 150 °C for 6 h and calcined at 400 °C for 6 h with heating and cooling rates of 1 °C/min. The gel-less secondary growth was carried out by impregnating an aqueous solution containing 0.075 M of tetrapropyl ammonium bromide (TPABr) and 0.075 M of potassium hydroxide (KOH) into the coated SSF support. The impregnated nanosheets-coated support was horizontally put into a Teflon-lined stainless-steel autoclave (45 ml in volume) followed by heating at 190 °C for 16 h. After the secondary growth, the membrane was soaked in fresh DI water for 1 day to remove the remaining chemicals. The DI water was replaced with fresh DI water after 4 h soaking. Then, the membrane was dried at 70 °C for 4 h for further detemplation study with either low temperature thermal calcination or UV/ozone treatment. For low temperature calcination, the membrane was heated in a tubular furnace with an air flow of 110 ml/min at a desired temperature for 8 h with heating and cooling rates of 0.5 °C/min. For UV/ozone treatment, the membrane was put into a UVO-Cleaner (Model 42, Jelight Company Inc.) at room temperature with the distance between the membrane surface and the UV lamp of 6 mm.

2.2.2 Characterization

The TEM images were obtained with an FEI Tecnai T12 TEM operating at 120 kV. The

SEM was performed using JEOL 6700 microscope operating at 1.5 kV. The membrane cross-section for SEM was cut with Ga focused ion beam (FIB) at 30 kV (Quanta 3D DualBeam) after sputter coating of Au onto the membrane with thickness of ~300 nm.

2.2.3 Gas permeation test

The mixed xylene isomer or butane isomer gases permeance was measured with Wicke-Kallenbach (WK) mode as described previously[51]. Typically, equimolar xylene isomer or butane isomer gases at atmospheric pressure were introduced into the membrane side with helium as carrier and sweep gas. The compositions of feed and permeate were analyzed with a gas chromatography (GC, Agilent 7890B). The xylene isomer gases were analyzed with a capillary column (DB-WAXetr, Chrom Tech) and a flame ionization detector (FID). The butane isomer gases were analyzed with a packed column (30% DC-200 on Chromosorb PAW packing, Agilent) and a thermal conductivity detector (TCD). Single-gas permeation tests of *n*-butane or *iso*-butane were performed with pressure gradient mode by recording the pressure change in the closed side with fixed volume initially maintained at vacuum.

2.3 Results and discussion

2.3.1 Membrane fabrication

We have previously demonstrated that the *b*-out-of-plane MFI-nanosheets are desirable to fabricate *b*-oriented MFI membranes since the straight *b*-direction channels (~5.5 Å) are perpendicular to the nanosheet surface[13,36,21], which is favorable for the molecular transport. The nanosheets were produced by exfoliation of the multilamellar MFI zeolite via melt-compounding with polystyrene[21], followed by purification of the exfoliated

nanosheets through density gradient centrifugation (DGC)[36]. The transmission electron microscopy (TEM) image shown in **Figure 2.1a** revealed that the maximum lateral size of the nanosheets was as high as 400 nm. The nanosheet thickness was proved to be 3.2 nm (1.5 unit-cells thick)[36,21], which indicated an aspect ratio of ~270. The MFI nanosheet suspension will be used to coat the porous SSF support to fabricate *b*-oriented MFI thin membranes.

The SSF support was made by sintering of silica fibers (1-10 μm) followed by surface rubbing with 500 nm and 50 nm Stöber silica spheres. The top-view SEM image shown in **Figure 2.1b** indicated a smooth surface of the support after rubbing. The coated 50 nm silica spheres also served as silica source during the gel-less secondary growth. A ~50 nm thin layer of MFI-nanosheets was coated onto the support by filter-coating method. The coated nanosheets laid flat on the support with the *b*-out-of-plane orientation as shown in **Figure 2.1c**. To fill the non-selective gaps between the nanosheets, the gel-less secondary growth was performed by impregnating of 0.075 M TPABr and 0.075 M KOH aqueous solution into the nanosheets coated support followed by heating at 190 °C for 16 h. The resulting film exhibited uniform structure with intergrown and *b*-oriented crystals shown in **Figure 2.1d**. The cross-section SEM image in Figure 1e indicated the membrane thickness of 74 nm (21° tilted) after the secondary growth. These *b*-oriented thin membranes will be further used for the study of detemplation with mild conditions and all the membranes were made by the identical methods.

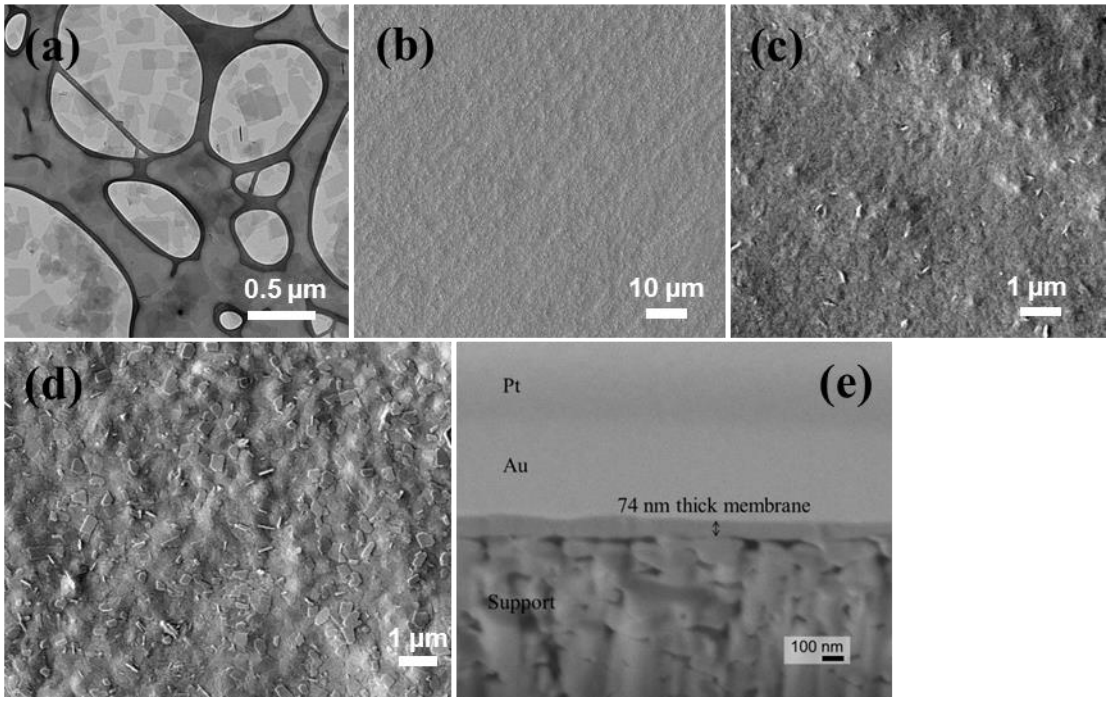

Figure 2.1. (a) TEM images of the b-out-of-plane oriented MFI-nanosheets. (b) Top-view SEM image of the 500 nm and 50 nm Stöber silica spheres coated SSF support. (c) Top-view SEM image of the MFI-nanosheets coated support. (d) Top-view and (e) cross-section SEM images of the membrane after gel-less secondary growth with impregnated 0.075 M TPABr and 0.075 M KOH aqueous solution at 190 °C for 16 h.

2.3.2 Low temperature thermal calcination

300 °C calcined membrane:

The as-synthesized membrane was first calcined at 300 °C for 8 h with heating and cooling rates of 0.5 °C/min. The calcined membrane showed slight yellowish color on the surface, which indicated the deposition of carbonaceous species during the calcination. The calcined membrane exhibited *p*-/*o*-xylene separation factor (SF) of 469 with corresponding *p*-xylene permeance of 8.0×10^{-8} mol m^{-2} s^{-1} Pa^{-1} at 150 °C. Our previous report described the membranes made by the same method (identical nanosheets coating with secondary growth at 190 °C for 16 h with 0.075 M TPABr and 0.075 M of KOH

aqueous solution, calcination at 450 °C for 4 h with cooling and heating rates of 0.5 °C/min) delivered a maximum SF of 185 with *p*-xylene permeances in the range 1.7-3.6×10^{-7} mol m^{-2} s^{-1} Pa^{-1} at 150 °C[13]. Thus, it can be concluded that the majority of the micropores were opened up after the calcination at 300 °C for 8 h. The relative low *p*-xylene permeance was probably due to the small quantity of remaining tetrapropylammonium cation (TPA^+) occluded in the micropores as well as the surface deposition of carbonaceous species.

The butane isomer separation was also investigated with the same membrane for xylene isomer separation study calcined at 300 °C. The feed stream contained equimolar *n*-butane and *iso*-butane isomer (~50 kPa each). As shown in **Figure 2.2**, the *n*-butane permeance increased from 3.7×10^{-8} mol m^{-2} s^{-1} Pa^{-1} (at 25 °C) to 2.6×10^{-7} mol m^{-2} s^{-1} Pa^{-1} (at 180 °C) with the increase of testing temperature, while the SF decreased from 71 (at 25 °C) to 28 (at 180 °C). Compared with the previous results[13], the SF was slightly higher for the 300 °C calcined membrane than that for the 450 °C calcined membrane.

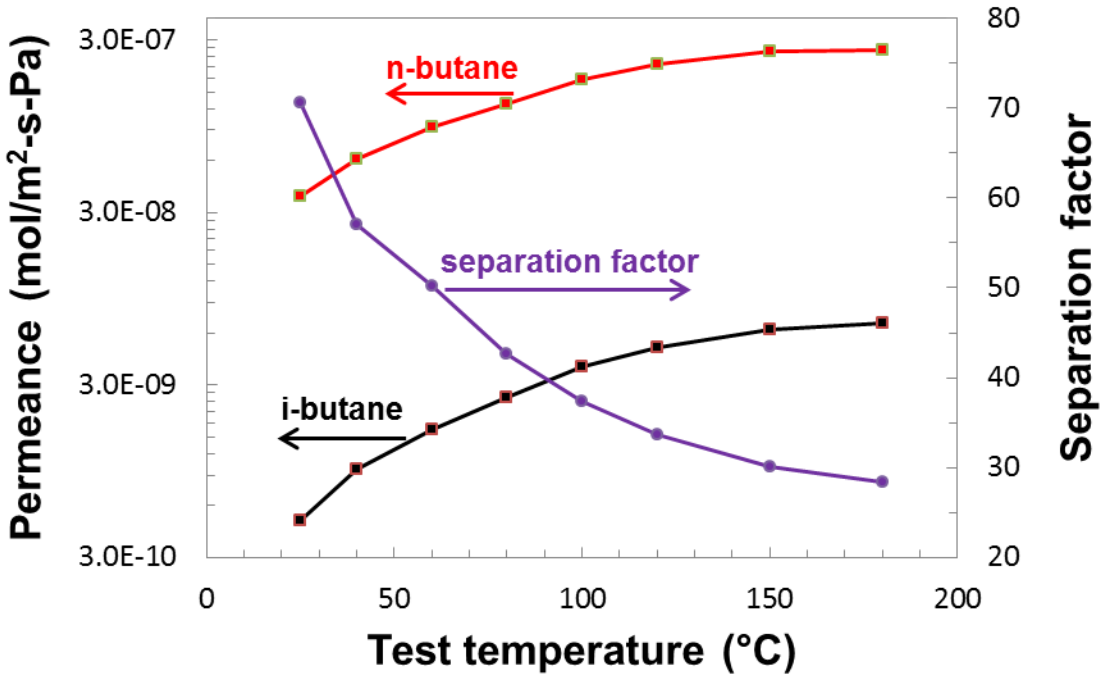

Figure 2.2. Butane isomer permeances and SF of the 300 °C calcined membrane at testing temperature ranging from 25 to 180 °C.

280 °C calcined membrane:

Since our aim is to investigate the lowest detemplation temperature for the *b*-oriented thin membrane, the calcination temperature was further decreased to 280 °C with the same duration time of 8 h and the same heating and cooling rates of 0.5 °C/min. The xylene isomer separation performance of the 280 °C calcined membrane was shown in **Figure 2.3a**. The permeance of *p*-xylene increased to the maximum value of 1.3×10^{-7} mol m^{-2} s^{-1} Pa^{-1} at the testing temperature of 150 °C with the maximum SF of 439. The high permeance and SF demonstrated the efficient template removal at calcination temperature as low as 280 °C. The butane isomer separation performance was also investigated and showed in **Figure 2.3b**. The *n*-butane permeance increased from 3.7×10^{-8} mol m^{-2} s^{-1} Pa^{-1}

(at 25 °C) to 3.2×10^{-7} mol m^{-2} s^{-1} Pa^{-1} (at 140 °C) with the SF decreased from 30 (at 25 °C) to 14 (at 140 °C). The high performance of both xylene and butane isomer separation demonstrated the sufficient removal of templates from the micropores at the calcination temperature at 280 °C. It should be also noted that the membranes calcined at 270 °C and 250 °C for 8 h with heating and cooling rates of 0.5 °C/min exhibited non-detectable permeance of xylene or butane isomer. Thus, it can be concluded that the lowest nominal detemplation temperature for such *b*-oriented thin membrane is 280 °C.

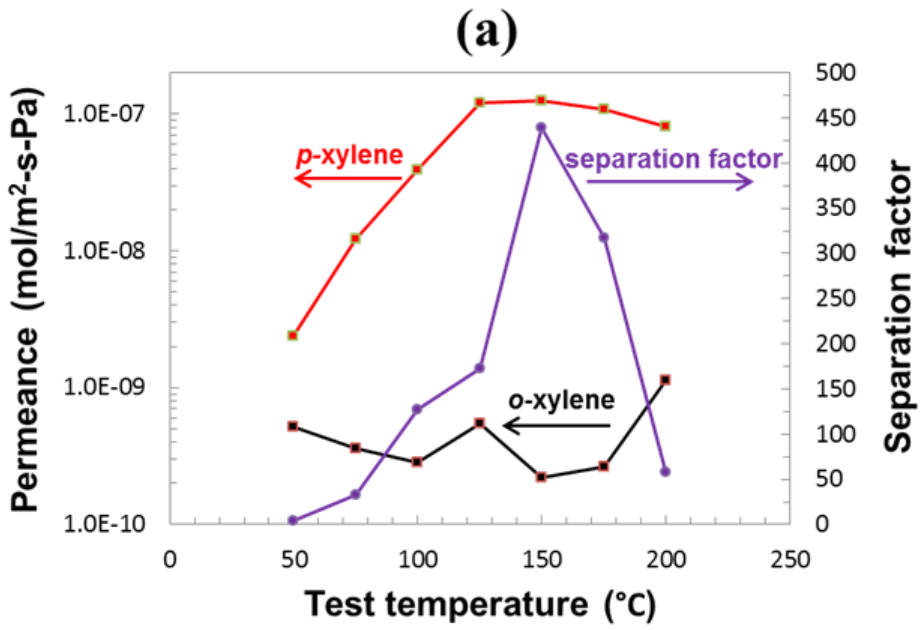

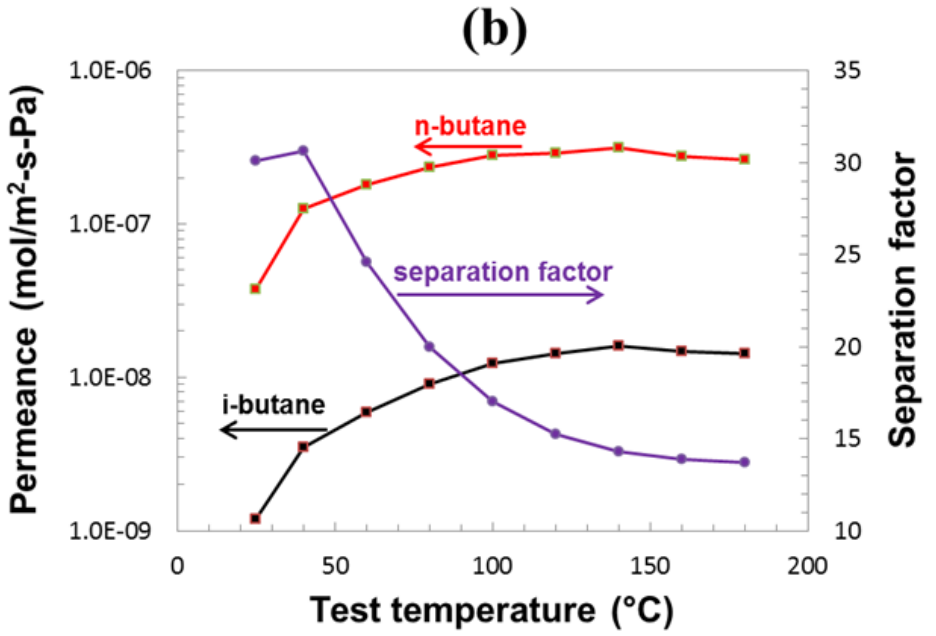

Figure 2.3. a) Xylene isomer permeances and SF of 280 °C calcined membrane with testing temperature ranging from 50 °C to 200 °C. b) Butane isomer permeances and SF of 280 °C calcined membrane with testing temperature ranging from 25 °C to 180 °C.

2.3.3 UV/ozone treatment

UV/ozone treatment is another alternative mild detemplation approach to remove the organic templates from the MFI membranes. The surface temperature during the treatment was around 80 °C. The membrane was put into a chamber (UVO-Cleaner, Model-42, Jelight Company Inc.) connected to an exhaust that has a fan pulling vacuum. The low pressure mercury UV lamp is located on the top inside the chamber which can generate UV irradiation with wavelength from 184 to 254 nm. During the treatment, ozone molecules are continuously generated by the UV radiation. Atomic oxygen is generated by dissociation of molecular oxygen by 184.9 nm waves and ozone by 253.7 nm waves. In addition, the hydrocarbon molecules can be activated by absorption of the

253.7 nm radiation, which is desirable to be destroyed by the atomic oxygen to generate volatile, simple molecules to escape from the micropores in MFI membrane layer.

To investigate the template removal process during UV/ozone treatment, the single gas permeance tests at room temperature were applied to track the detemplation process. After 2 h treatment, the nitrogen permeance was still very low (1.4×10^{-9} mol m^{-2} s^{-1} Pa^{-1}), as shown in **Figure 2.4**. However, when the total treatment time increased to 4 h, the nitrogen permeance significantly increased by an order of 2, to 1.5×10^{-7} mol m^{-2} s^{-1} Pa^{-1}. This result indicated the efficient micropore opening happened between 2 and 4 h of UV/ozone treatment. As the total treatment time increased to 6 h, the nitrogen permeance further increased to 1.3×10^{-6} mol m^{-2} s^{-1} Pa^{-1}, which indicated more micropores were opened. After 6 h treatment, the nitrogen permeance increased slightly with prolonged treatment time. The *n*-butane and *iso*-butane single gas permeances at room temperature were also investigated as shown in **Figure 2.4**. The *n*-butane single gas permeance increased from 2.0×10^{-7} mol m^{-2} s^{-1} Pa^{-1} after 4 h treatment to 4.6×10^{-7} mol m^{-2} s^{-1} Pa^{-1} after 10 h treatment with the n-/iso-butane ideal selectivity ranging from 103 to 158.

To study the mixed gases separation performance, another membrane made by the identical method was treated continuously by UV/ozone for 10 h. The resulting membrane exhibited *p*-xylene permeance of 7.7×10^{-7} mol m^{-2} s^{-1} Pa^{-1} with SF of 25 and *n*-butane permeance of 8.8×10^{-8} mol m^{-2} s^{-1} Pa^{-1} with SF of 71. All these results demonstrated the UV/ozone treatment is an efficient approach to detemplate the MFI membranes preserving both high permeance and selectivity. Similar as the low temperature treated membranes, the UV/ozone treated membrane also exhibited

yellowish color on the surface. To avoid the carbonaceous deposition, efficient fresh air or oxygen flow should be introduced into the chamber to further improve the gas permeance after treatment.

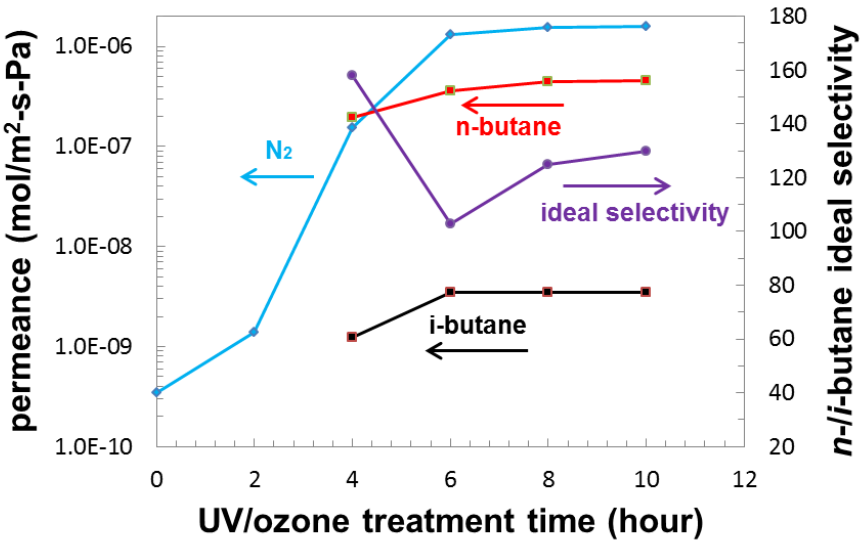

Figure 2.4. Room temperature single gas permeances of nitrogen, *n*-butane and *iso*-butane, and *n*-/*iso*-butane ideal selectivity as the function of UV/ozone treatment time. This figure was also published in literature[13].

2.4 Conclusion

In summary, two mild detemplation approaches with the *b*-oriented thin MFI membrane as the model were demonstrated: (i) low temperature thermal calcination; (ii) UV/ozone treatment. Calcination temperature as low as 280 °C or UV/ozone treatment after 6 h are efficient to remove the majority of organic templates from the membrane, leading to high permeable membrane for *p*-xylene and *n*-butane with high selectivity.

Chapter 3. MFI membrane supported on polymer support and mild detemplation

3.1 Introduction

Most of the currently used methods for the fabrication of zeolite membranes require a calcination step to completely remove the SDA inside the zeolite layer and thus inorganic ceramic supports are widely used due to their high thermal and mechanical properties. There are several reports that polymer supports were used for zeolite membrane fabrication in which SDA-free secondary growth were used and high temperature calcination was not needed. For example, high flux zeolite NaA membranes were fabricated with polyethersulfone hollow fibers as supports.[52] Faujasite membranes were fabricated on polyethersulfone supports covered with PDMS layers for CO_2/N_2 separation.[53] These polymer supported membranes are feasible because no SDA removal was required. However, no attempts have been reported for polymer supported Silicalite-1 (all silica type MFI zeolite) membranes since SDA is required for the secondary growth. For the successful growth of Silicalite-1 membrane on polymer support, the polymer used should be stable in basic solution and could withstand temperatures up to 100 °C.

In this chapter, polyethersulfone (PES), polybenzimidazole (PBI), and polyimide (PI) porous supports were used for the growth of Silicalite-1 membranes. Finally, the two mild detemplation methods identified in chapter 2 were applied to the membranes.

3.2 Experimental

3.2.1 Fabrication of free-standing PI and PES supports

The porous polymer supports were fabricated by non-solvent induced phase separation

(NIPS) method. The PI and PES were supplied from SABIC (EXTEM® XH1015-1000) and SOLVAY (Veradel® A-301), respectively. The solvent for both PI and PES was N-methyl-2-pyrrolidone (NMP). The non-solvent for the polymer solution was de-ionized (DI) water. The thickness of polymer solution casting film was fixed as 100 μm and a flat glass plate was used as a blade for solution casting. The fabrication conditions for both PI and PES were the same, including a polymer/NMP concentration of 15 wt%, pure DI water bath at 50 to 60 °C, and a room temperature air drying condition.

3.2.1 Fabrication of mesh supported PES and PBI supports

To improve the mechanical strength of the polymer support, a porous stainless steel mesh was used as backing. The mesh discs (stainless T316, 10 micron 2 layer sintered wire mesh) were purchased from TWP Inc. and with diameter of 22 mm. Similarly, the polymer solution was cast onto the mesh disc and immersed in water bath at 60 °C. After about 3 minutes, the membrane was then transferred into another water bath for solvent exchange for 1 day. The water bath was changed every 6 hours. The support was then allowed to dry at ambient temperature for one day. For PBI supports, they were thermally treated at 300 °C for 8 hours before use.

3.2.2 Nanosheet coating and secondary growth

The exfoliated MFI zeolite nanosheets suspension was fabricated according to the method described by Varoon et al.[36] followed by further purification by density gradient centrifugation to remove most of the un-exfoliated particles. Finally, the purified exfoliated nanosheets were dispersed in 1-octanol. The setup for nanosheet coating onto porous polymer support was shown in **Figure 3.1**. A disc shaped polymer support was

put onto a porous sintered stainless steel disc. The porous sintered stainless steel plate acted as a mechanical support to keep the polymer membrane flat during the coating process. The application of o-rings would ensure sufficient sealing. After the connection of vacuum to the bottom tube, zeolite nanosheet suspension was introduced onto the polymer membrane. When the 1-octanol solution drained out, the vacuum pump was closed and the coated membrane was carefully transferred into a glass petri dish and heated at 130 °C for 12 h to remove the remaining solution.

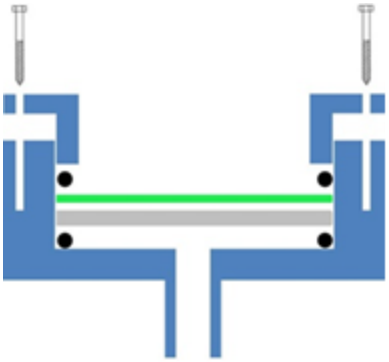

Figure 3.1. Cross section of the setup for vacuum coating. The black spot indicated o-ring; the green plate indicated porous polymer membrane; the grey plate indicated porous sintered stainless steel. The bottom tube was connected with vacuum pump. The zeolite nanosheets suspension was added to the top of polymer membrane. The 1-octanol solvent was removed via vacuum and the zeolite nanosheets were uniformly coated on the polymer membrane.

The secondary growth was performed according to the methods reported in the literature.[21] Typically, a synthesis sol with composition of 60 SiO_2 : 9 TPAOH : 8100 H_2O : 240 EtOH was obtained by hydrolysis of tetraethyl orthosilicate (TEOS) for 4 h at room temperature in the presence of tetrapropylammonium hydroxide (TPAOH) (1.0 M) and DI water. The synthesis gel was aged in a preheated oven at 90 °C for 6 h in a Teflon-lined autoclave. After the aging, the synthesis gel was cooled to room temperature

and filtered by 0.2 μm filter into a Teflon-liner. The nanosheets coated membrane was vertically placed in the filtered gel and heated at 90 °C (or 100 °C) for desired time. The membrane was then taken out from the solution after it was cooled down to ambient temperature and washed with DI water for 5 minutes. The membrane was then allowed to dry at ambient temperature overnight.

3.2.3 Mild detemplation treatment

The mesh-PES supported MFI membrane was treated inside Jelight UVO cleaner (Model 42) for desired time. For thermal treatment at low temperature, the PBI supported membrane was treated inside a tubular furnace with desired ramping rate.

3.3 Results and discussion

3.3.1 PI free-standing supports

The SEM images of the free-standing PI supports are shown in **Figure 3.2**. The surface of the membrane is smooth with surface pores of about 15 nm (**Figure 3.2A**). The thickness of the membrane is around 100 μm with the typical finger-type structure (**Figure 3.2B**). The width of the pore channel increases gradually from the top to the bottom layer, connecting directly through surface to bottom, which allowed the penetration of solvent (such as 1-octanol, the dispersion solvent for exfoliated nanosheets) through the membrane with less resistance. The bottom surface showed bigger pores with diameter of about 1 μm. The structure of this kind of PI porous membranes makes it suitable for vacuum filtration of zeolite nanosheets onto the surface. The smooth surface of the PI membranes could allow thinner, uniform, and complete coating of the zeolite nanosheets. Such thinner coating of zeolite nanosheets would lead

to thinner thickness of the zeolite membrane after secondary growth, which would further result in lower permeation resistance and finally contribute to a decrease of the membrane cost. In addition, the finger-type pore structure of polymeric support would have smaller transport resistance of molecules as compared with the inorganic supports, which consequently increases the membrane flux and would also result in the decrease of the cost.

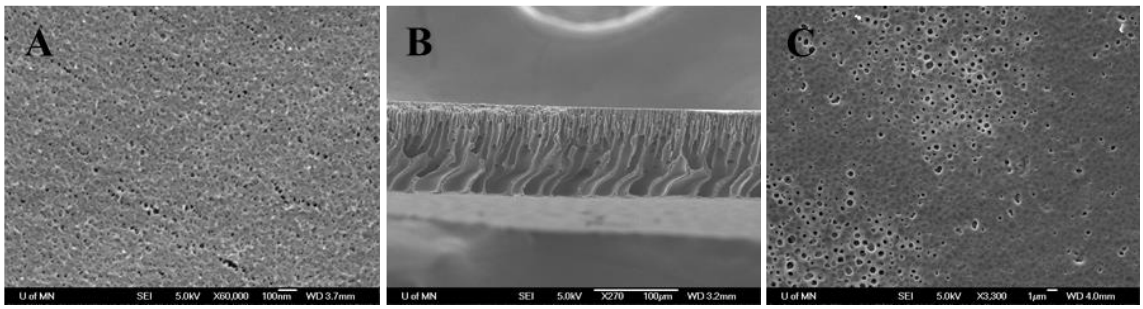

Figure 3.2. SEM images of PI porous membrane. (A) top surface; (B) cross section; (C) bottom surface. The experimental conditions: 15 wt% PI/NMP solution; DI water bath at 51 °C; air dried at room temperature.

3.3.2 PES free-standing supports

The fabrication conditions for PES porous membrane were almost the same as that of the PI membranes. The resulting porous PES membrane also has similar structures as that of PI membranes, except that the former has slightly bigger surface pore diameter of about 20 nm, which might be due to the higher water bath temperature at 60 °C (for PI membrane formation it was at 51 °C). Thus, the obtained PES membrane could also be a suitable support for the following deposition of zeolite nanosheets.

3.3.3 Coating of MFI nanosheets on porous polymer supports

Since the nanosheets have high aspect ratio, most of the nanosheets would horizontally

and uniformly coated on the polymer membrane surface, as showed in **Figure 3.3**, for both PI and PES membranes. The uniform and oriented coating of nanosheets originates from the large aspect ratio of the nanosheets, as well as the stable dispersion of nanosheets in the 1-octanol solution.

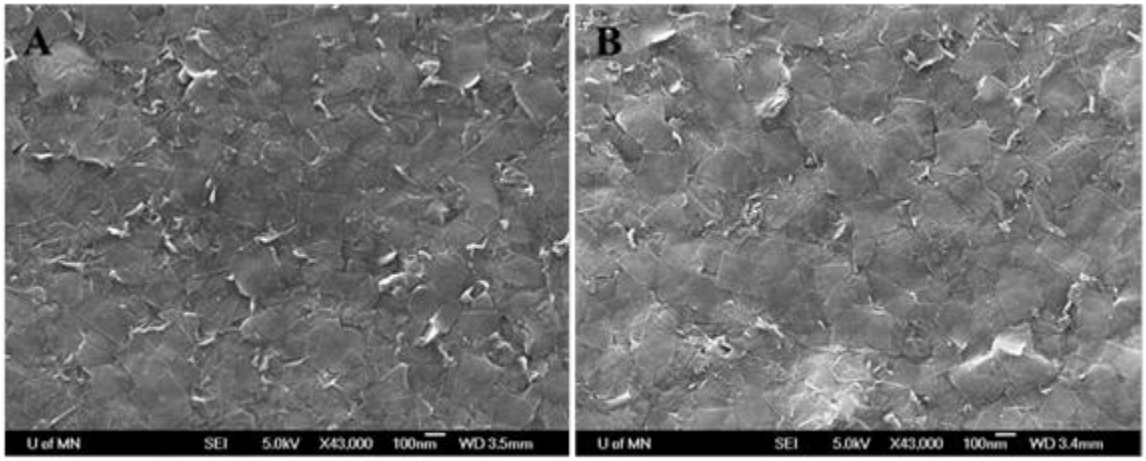

Figure 3.3. Zeolite nanosheets coating with porous PI (A) and PES (B) as support, respectively.

3.3.4 Secondary growth with free-standing PI as support

The secondary growth of nanosheets coated PI support was conducted at 90 °C for 4.5 h, which was the same condition as the literature[21]. The SEM image of the resulting membrane is shown in **Figure 3.4**. Obviously, the top layer of the PI membrane as well as all nanosheets coating has been removed out. This is due to the ring-opening reaction of polyimide chains in the alkaline solution at high temperature[54]. Actually, alkaline solution treatment of polyimide membrane is a general method to introduce carboxylic groups in the polyimide membrane. In the alkaline solution with high pH value (such as 14) at room temperature, the dense PI membranes would not be destroyed.[54] However,

the secondary growth solution applied here with the pH value of about 11, while the temperature was 90 °C, which was too high to retain the structure of the asymmetric PI membrane. The polymer chains with carboxylic groups can easily dissolve in the growth gel at high temperature. Thus, the PI support is not suitable for this secondary growth condition.

3.3.5 Secondary growth with free-standing PES as support

PES has excellent alkaline resistant property. The secondary growth of nanosheets coated PES membranes was conducted at higher temperature (100 °C,) for longer time (18 h). The resulted membrane was characterized by SEM and shown in **Figure 3.4**. It is obvious that the whole membrane is stable during the secondary growth and zeolite coating layer undergoes effective inter-growth to fill the voids between the nanosheets (**Figure 3.4A** and **B**). However, there are also several big cracks (about 10 μm) formed in the zeolite layer (**Figure 3.4C** and **D**). These cracks could be due to the shrinkage of the free-standing PES support during the drying step. The PES support might absorb water during the secondary growth step at high temperature and expand to a bigger size. Thereby the zeolite inter-growth took place on the expanded PES support. During the drying step, the absorbed water in the PES support gradually diffused out of the PES support, leading to the shrinkage of PES support. At the same time, the dimension change of the zeolite layer would be negligible compared with that of the PES support during drying. In this case, compressive stress in the zeolite layer was formed and gradually increased with the removal of water in the PES support. When the stress increased to a critical value, the zeolite layer could not bear the force and cracks were formed. In addition, the thickness

of the zeolite layer is about 800 nm as shown in **Figure 3.4D**.

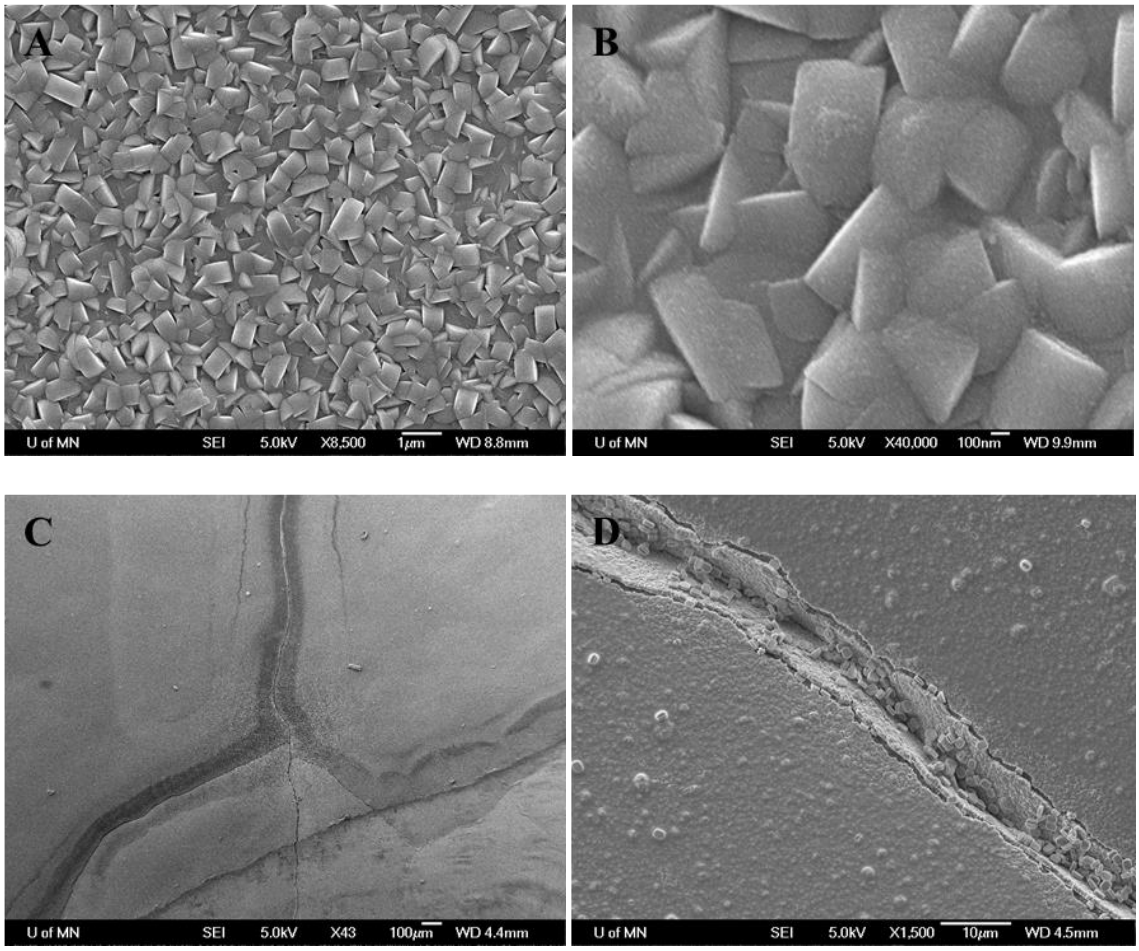

Figure 3.4. SEM images of nanosheets coated PES membrane after secondary growth at 100 °C for 18 h. (A) and (B) different magnification of the surface structure of zeolite layer after secondary growth. (C) and (D) cracks formed after drying at room temperature.

To further decrease the thickness of the intergrown zeolite layer, less amounts of nanosheets coating as well as shorter growth time (7 h) was investigated. The SEM images of the surface structure of the zeolite layer after secondary growth are shown in **Figure 3.5**. The thickness of the zeolite coating layer was about 100 nm and cracks still formed as shown in **Figure 3.5C** and **D**. However, the crack structure is different from

that of the previous one shown in **Figure 3.4**. More cracks of the latter with 100 nm of thickness formed than that of the previous one with thickness of 800 nm, while the width of the crack was smaller (about 1 μm) than that of the previous one (about 10 μm).

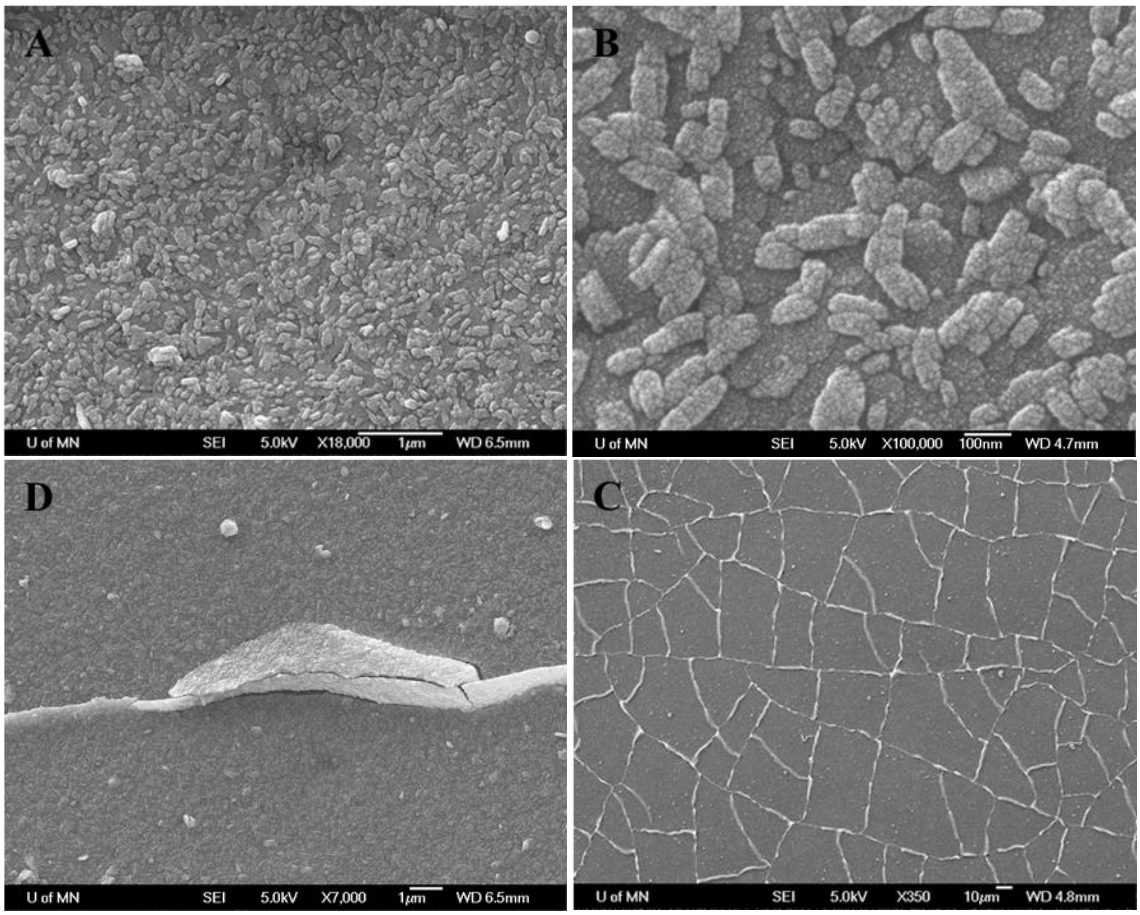

Figure 3.5. SEM images of nanosheets coated PES membrane after secondary growth at 100 °C for 7 h. (A) and (B) different magnification of the surface structure of zeolite layer after secondary growth. (C) and (D) cracks formed after drying at room temperature.

3.3.6 Secondary growth with mesh-PES as support

To prevent the cracks after secondary growth, the metal mesh was used as backing material to prevent the dimensional change of PES layer during and after the secondary growth. The PES top layer also had a porous structure as shown in **Figure 3.6**. The

nanosheet coating and secondary growth were the same as before. **Figure 3.7** showed the photo of bare mesh, mesh-PES support, and the mesh-PES supported MFI membrane after secondary growth.

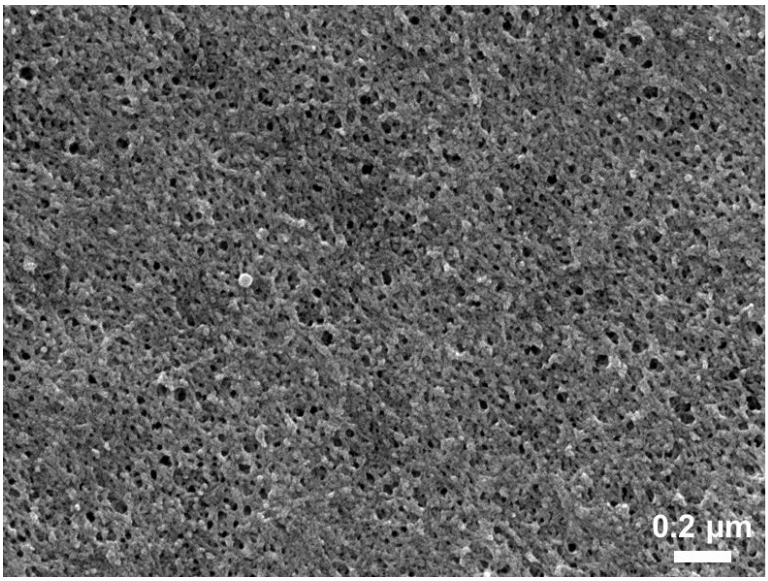

Figure 3.6. SEM image of top surface of the mesh-PES support.

Figure 3.7. Photo of the bare mesh disc before solution casting (left), after PES membrane coating (middle), and after membrane growth (right).

Figure 3.8 showed the SEM image of the MFI membrane after secondary growth at 90 °C

for 18 h. There were no cracks confirmed by SEM imaging. To further prove the successful intergrown of the MFI membrane, N_2 single gas permeance was measured. The N_2 permeance of this membrane at ambient temperature was 1.9×10^{-10} mol/m^2-s-Pa, which is comparable to the membrane grown on ceramic support before calcination, which demonstrated the successful secondary growth with the mesh-PES as support. Thus, it is ready to apply the two mild detemplation methods identified in chapter 2 to this membrane to remove the OSDA.

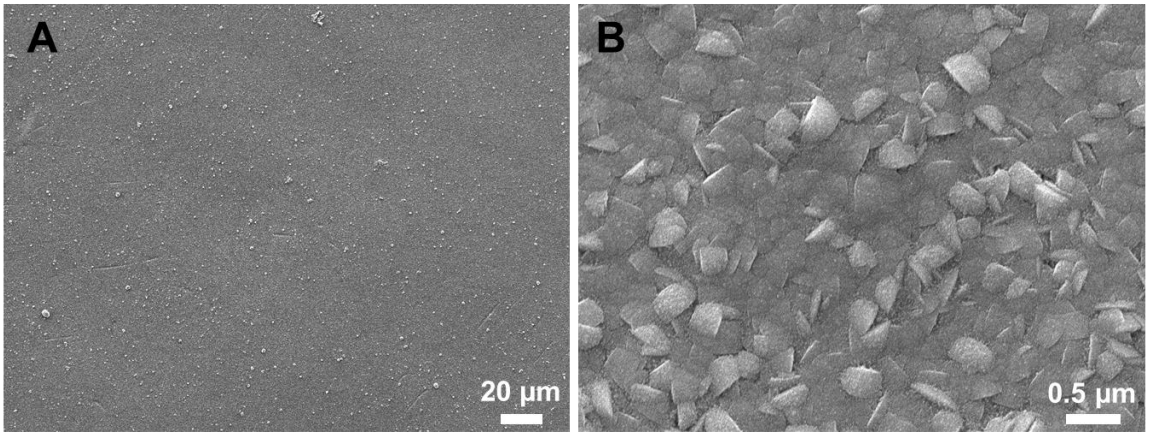

Figure 3.8. Low and high magnification SEM image of the top view MFI membrane after secondary growth at 90 °C for 18 h.

3.3.6 UV/ozone treatment

The mesh-PES supported MFI membrane was treated with UV/ozone treatment the same as reported in Chapter 2. After 1.5 h treatment, however, cracks formed as seen in **Figure 3.9**. As demonstrated in Chapter 2, 6 h UV/ozone treatment was required for a sub-100 nm MFI membrane. Obviously, 1.5 h is not sufficient. MFI membranes with thinner thickness by reducing the coating layer thickness and secondary growth time still could not prevent the formation of cracks.

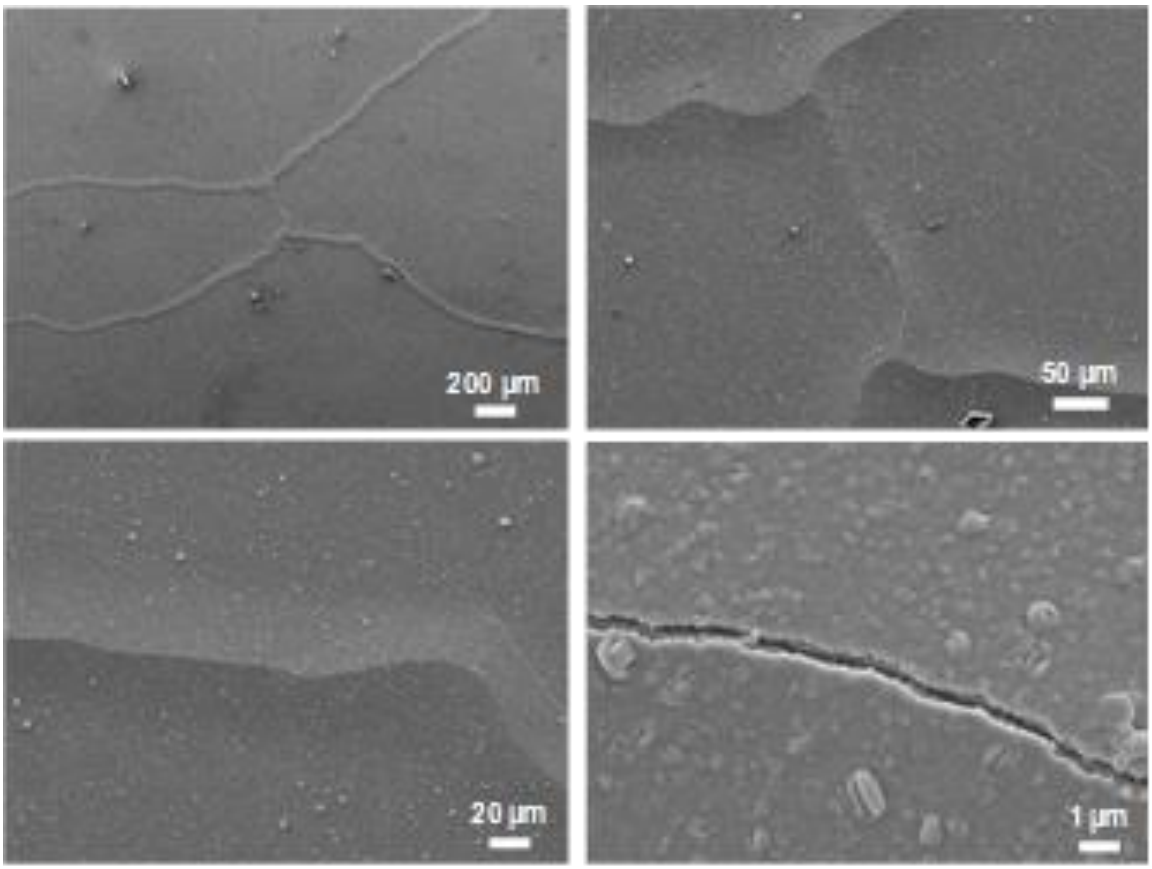

Figure 3.9. SEM images of the mesh-PES supported MFI membrane after UV/ozone treatment for 1.5 h.

A probable reason for the cracks could be the damage of PES layer. **Figure 3.10** showed the structure change of a bare PES membrane after UV/ozone treatment from 1 minute to 7 minutes. After about 7 minutes, the surface was seriously damaged and pores with several hundred nanometers were observed. Although the MFI membrane could protect the PES layer for some extent, it still could not survive after 6 h treatment. Thus, UV/ozone treatment is not feasible.

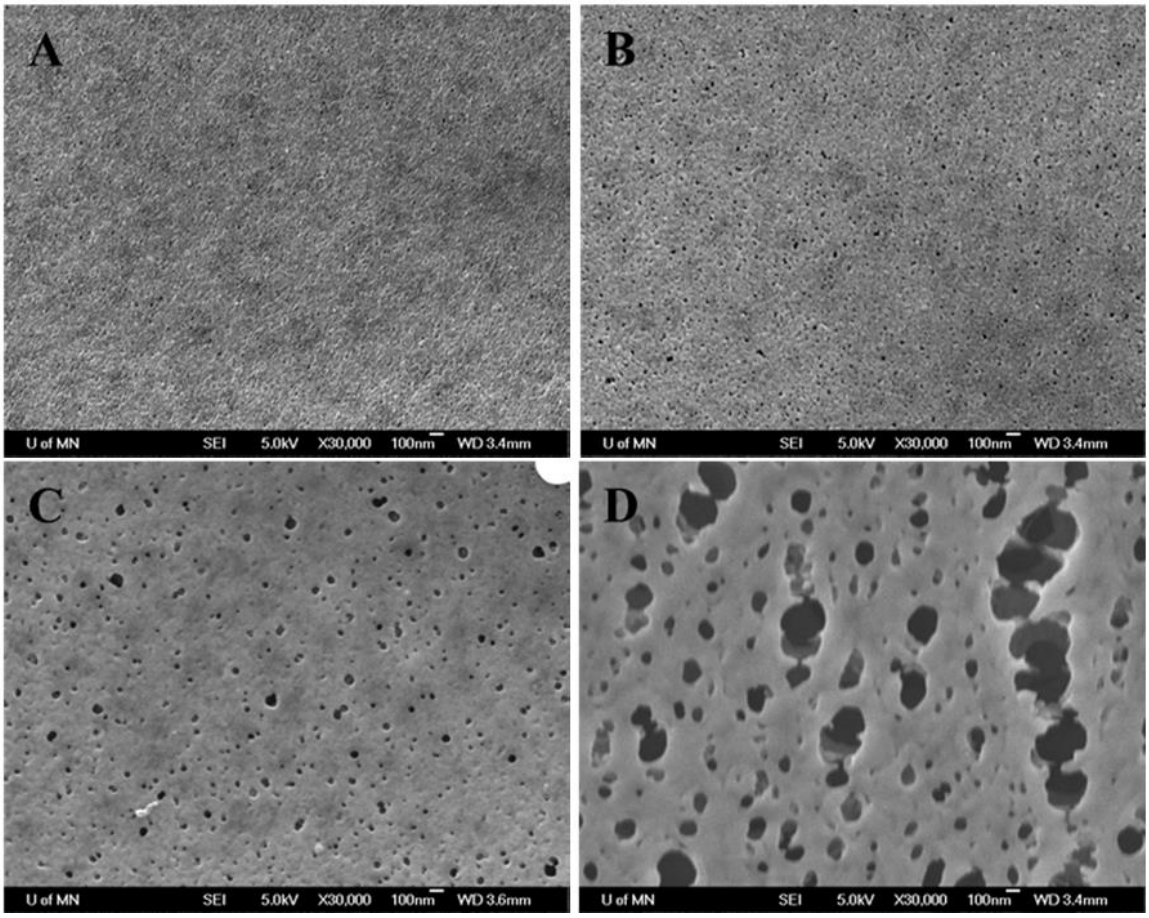

Figure 3.10. SEM images of PES membrane after UV-ozone treatment for (A) 1 min; (B) 3 min; (C) 5 min; (D) 7 min.

3.3.7 Low temperature thermal treatment

For low temperature thermal treatment, the polymer layer should be stable at 280 °C. Thus, PES is not suitable since its glass transition temperature is about 220 °C. Since PBI has much higher glass transition temperature up to 490 °C, it was selected as the support. The nanosheets used were open-pore MFI nanosheets (discussed in Chapter 4). After coating and dried at ambient temperature overnight, the membrane was treated in a tubular furnace at 250 °C for 8 h with ramping and cooling rate of 0.1 °C/min. However, cracks formed as shown in **Figure 3.11**. The reason could be the mismatch of linear

thermal expansion co-efficient between zeolite layer and polymer layer. Thus, low temperature treatment is not feasible neither.

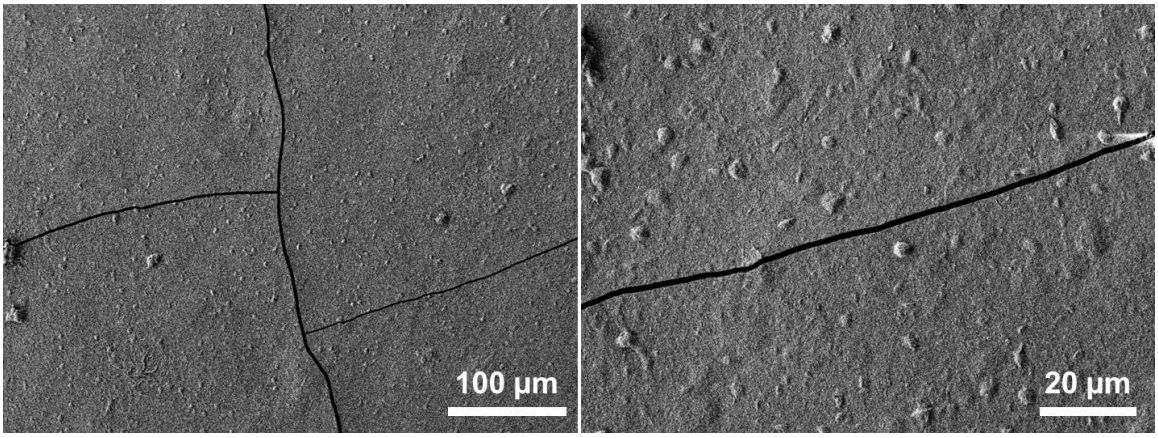

Figure 3.11. SEM images of MFI membrane supported on mesh-PBI support and treated at 250 °C for 8 h with ramping and cooling rate of 0.1 °C/min.

3.4 Conclusion

Defect-free MFI membrane has been successfully grown on mesh-PES support. The mesh backing layer could prevent the cracks after the secondary growth. However, the two mild detemplation methods created cracks during the treatment.

Chapter 4. Open-pore 2-dimensional zeolite MFI nanosheets and their use for the fabrication of hydrocarbon isomer-selective membranes on porous polymer supports

*Part of the work was done by Dr. Xiao Qiang, Dr. Xianghai Guo, Dr. Najun Li, and Prashant Kumar. Part of this chapter was adapted from Han Zhang, Qiang Xiao, Xianghai Guo, Najun Li, Prashant Kumar, Neel Rangnekar, Mi Young Jeon, Shaeel Al-Thabaiti, Katabathini Narasimharao, Sulaiman Nasir Basahel, Berna Topuz, Frank J. Onorato, Christopher W. Macosko, K. Andre Mkhoyan, and Michael Tsapatsis, *Angew. Chem. Int. Ed.* **2016**, 55, 7184-7187. Copyright 2016 Wiley-VCH Verlag GmbH & Co. KGaA, Weinheim.

4.1 Introduction

Suspensions of 2-dimensional (2D) zeolite nanosheets can provide building blocks for the fabrication of membranes and catalysts.[21,31,55–57] Multi-lamellar MFI (ML-MFI) zeolites with 1.5-unit-cell MFI nanosheets assembled along their *b*-axis, have been reported by Ryoo and co-workers.[35,58] They were synthesized using a class of OSDA composed of long-chain alkyl groups and two quaternary ammonium head groups spaced by a C6 alkyl linkage ($C_{22\text{-}6\text{-}6}$). The bi-ammonium part plays a structure-directing role for the formation of the MFI crystal structure, while the long-chain alkyl tails guide the formation of lamellar assemblies.[59,60] ML-MFI can be exfoliated to obtain single-layer 2D zeolite MFI nanosheets. Unlike other 2D materials (e.g., clays, graphene, MoS_2, BN, and WS_2 etc[61–65]), for which exfoliation can be achieved by various solution-based methods, exfoliation of ML-MFI has only been reported by a polymer-melt-blending technique.[21,36] According to this method, polystyrene (PS) is mixed with ML-MFI and then the mixture is melt-blended. During melt-blending, the polymer chains penetrate into the ML-MFI and, in combination with the shear force generated by the rotating screws, cause exfoliation. Exfoliated 2D MFI nanosheets are obtained after PS removal, purification by density

gradient centrifugation (DGC) and re-dispersion in organic solvents. The obtained MFI nanosheets are hydrophobic and can be dispersed in non-polar solvents like toluene and octanol but not in water. Dispersion in water is desirable because it will enable layer-by-layer deposition methods for nanocomposite and thin film fabrication.[66,67] Moreover, the exfoliated nanosheets contain OSDA in their micropores preventing their use as molecular sieves without further detemplation treatment for OSDA removal. Recently, we demonstrated that treatment with acid, according to a method reported earlier by Corma and co-workers, removes part of the OSDA and allows dispersion of the nanosheets in ethanol.[31,68] There is still approximately 8wt.% OSDA left after acid treatment and the partially detemplated nanosheets cannot be dispersed in water[31] and do not exhibit microporosity by cryogenic Ar-adsorption. Here, the main difference from this earlier work is the use of a concentrated sulfuric acid (H_2SO_4) and hydrogen peroxide (H_2O_2) (piranha solution, H_2SO_4 : H_2O_2 volume ratio of 3:1) to treat as-synthesized or exfoliated ML-MFI particles. Also, the synthesis method of pure silica ML-MFI was modified (Supplementary information) from the previous reports[21,35] and larger MFI nanosheet domains were obtained (**Figure 4.1a**), compared with those synthesized by the previously reported method[21] (**Figure 4.1b**).

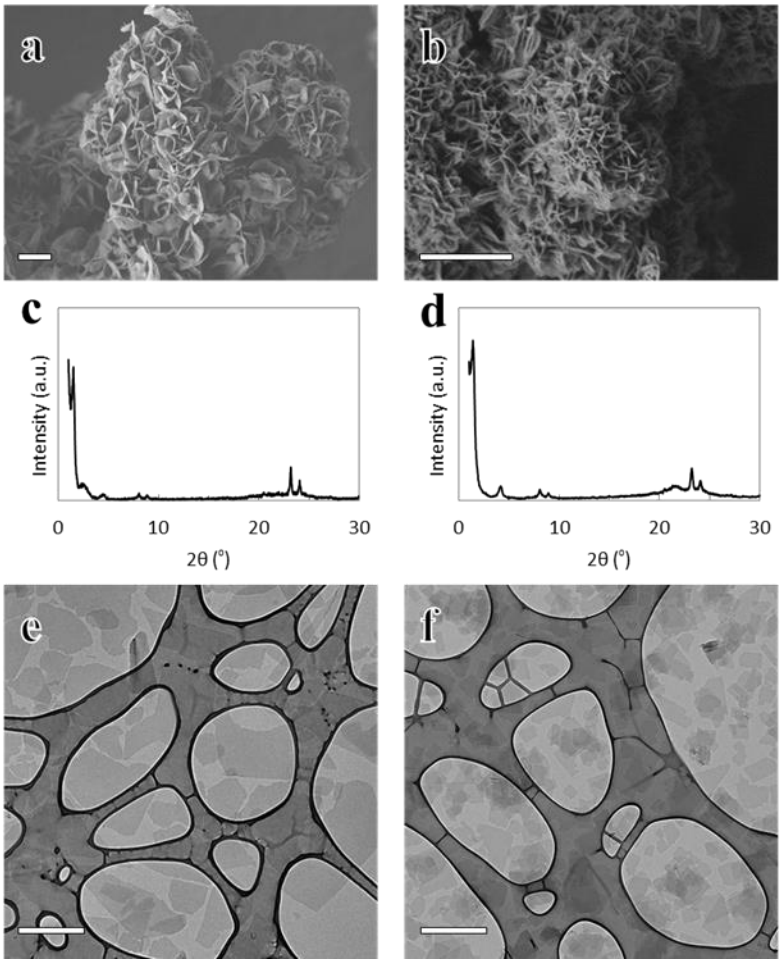

Figure 4.1. Characterization of ML-MFI and exfoliated nanosheets. a,c, SEM image (a) and XRD (c) pattern of the ML-MFI with larger lateral size by the modified synthesis method reported here. b,d, SEM image (b) and XRD pattern (d) of the smaller ML-MFI synthesized by the previously reported method[21]; scale bar is 1 μm. e, TEM images of the exfoliated nanosheets via melt-compounding (with oligomeric polystyrene resin, PiccolasticTM A75 (Mw~1,300), at 95 °C for 1 h) followed by the polystyrene removal from the larger ML-MFI (shown in a). f, TEM images of the exfoliated nanosheets via melt-compounding (with high molecular weight (Mw~45,000) polystyrene between 120 to 150 °C for 1.5 h[21]) followed by the polystyrene removal from the smaller ML-MFI (shown in b). Scale bars in a and b are 2 μm; scale bars in e and f are 0.5 μm.

4.2 Experimental

4.2.1 Synthesis of ML-MFI

ML-MFI zeolite was synthesized according to the previously reported procedure with some modifications[21,35]. Di-quaternary ammonium-type surfactant [$C_{22}H_{45}$–$N^+(CH_3)_2$–C_6H_{12}–$N^+(CH_3)_2$-C_6H_{13}](Br_2) ($C_{22\text{-}6\text{-}6}Br_2$) was used as OSDA. $C_{22\text{-}6\text{-}6}Br_2$ was synthesized by alkylation of *N,N,N',N'*-tetramethyl-1,6-diaminohexane (Sigma-Aldrich) with 1-bromodocosane (TCI) at 65 °C overnight followed by alkylation of the resultant product by 1-bromohexane (Sigma-Aldrich) at 85 °C overnight. For the synthesis of ML-MFI zeolite, tetraethyl orthosilicate (TEOS) (Sigma-Aldrich) was hydrolyzed in the presence of OSDA, sodium hydroxide (NaOH) (Sigma-Aldrich), sulfuric acid (H_2SO_4) (Sigma-Aldrich) and deionized (DI) water to obtain a gel composition of 100 SiO_2: 7.5 SDA: 24 NaOH: 18 Na_2SO_4: 400 EtOH: 4000 H_2O. After hydrolysis for 24 h at room temperature, the resultant gel was crystallized in a rotating Teflon-lined steel autoclave at 150 °C for 7 days. The product was obtained by centrifugation. The cake was washed with DI water and dried at 80 °C overnight. As a comparison, relatively smaller ML-MFI was synthesized according to a previous report.[21] The gel composition was 100 SiO_2: 15 $C_{22\text{-}6\text{-}6}(OH)_2$: 400 EtOH:4000 H_2O and the hydrothermal reaction was carried out in a Teflon-lined steel autoclave at 150 °C for 10 days.

4.2.2 Direct piranha solution treatment of ML-MFI

In a typical procedure, 0.1 g of the as-synthesized ML-MFI zeolite was dispersed in 12 mL of concentrated sulfuric acid (95~98%, Sigma-Aldrich) in a 50 mL Pyrex® glass bottle by bath sonication for 10 min. Then, 4 mL of hydrogen peroxide (30%, Fisher

Scientific) was dropped into the above suspension in a hood (CAUTION: The container will be very hot due to generation of heat!). The suspension was stirred for another 1 h. During the stirring period, the Pyrex® glass bottle was vented occasionally. Then, the Pyrex® glass bottle was protected in a secondary container and placed in an 80 °C oven for 24 h at a specially designated area with appropriate safety precautions and limited access to other lab members. After the secondary container and the Pyrex® glass bottle were completely cooled down to ambient temperature, the Pyrex® glass bottle was opened carefully in a hood. The suspension was transferred to 50 mL PTFE centrifuge tubes and centrifuged (Beckman Coulter, Model: Avanti J-20 XP equipped with JA25.50 rotor) at 40,000 *g* for 6 h to recover the solid. The resulting cake was treated with piranha solution for three more times the same way as described above. After the treatment, the cake was dispersed in approximately 50 mL of DI water. This aqueous suspension was sonicated in an ultrasonicator (Bransonic Ultrasonic cleaner, 1210) for 90 min, followed by horn sonication (Qsonica Q500, 500 watts, 1/4" micro-tip) for 10 min under the setting of 40% output intensity and 2 sec of pause for each 5 sec sonication sequence. The suspension was cooled in an ice bath to avoid temperature rise during the horn sonication.

4.2.3 Exfoliation of ML-MFI via melt-blending

The exfoliation of ML-MFI followed a previous report[21]. Typically, 0.6 g of ML-MFI was mixed with 14.4 g of oligomeric polystyrene (PS) (Eastman Chemical Company, Piccolastic™ A75 hydrocarbon resin, Mw~1,300 g/mol, Tg~35 °C) and added into the melt-compounder (Xplore® micro compounder MC15) at 95 °C and mixed for 1 h at 250

rpm. Then, 3 g of the extruded nanocomposite material was dissolved in 45 mL of filtered (0.22 μm filter) toluene inside a centrifuge tube and then centrifuged at 40,000 *g* for 3 h. The nanosheet cake collected at the bottom was then washed three times with fresh toluene to remove the residual PS and finally, a nanosheet cake was obtained at the bottom of the centrifuge tube.

4.2.4 Piranha solution treatment of the exfoliated nanosheets

The cake obtained from exfoliation via melt-blending (described above) was then treated with piranha solution for four times to remove the OSDA from the nanosheets, as shown in the schematic of Figure S8. Before piranha treatment, the cake was first washed with ethanol for two times and finally a cake was obtained at the bottom of the tube. This cake was then treated with piranha solution for four times successively via the same method discussed before (CAUTION: For safety, ethanol should be removed to a minimum before piranha treatment). Typically, 6 mL of concentrated H_2SO_4 (95~98%, Sigma-Aldrich) was added into the tube and sonicated for 2 min to fully disperse the cake. Then, 2 mL of H_2O_2 (30%, Fisher Scientific) was slowly dropped into the H_2SO_4 solution while shaking (CAUTION: The solution will become very hot!). The solution was stirred at ambient temperature for 1 h and then transferred into a capped Pyrex® glass bottle in a preheated oven at 80 °C overnight at a specially designated area with appropriate safety precautions and limited access to other lab members. After the bottle was fully cooled down to ambient temperature, the solution was transferred into a centrifuge tube and diluted to 45 mL with DI water. The suspension was centrifuged at 40,000 *g* for 6 h. The supernatant was then removed leaving a cake at the bottom of the tube. This piranha

solution treatment was then repeated for three more times. The cake was then washed with fresh DI water for five times and finally dispersed in 70 mL of DI water.

4.2.5 Fabrication of porous support

The porous PBI support was fabricated by casting of PBI solution onto a porous stainless steel mesh disc with non-solvent induced phase separation method. Typically, 20% PBI/Dimethylacetamide (DMAc) solution was diluted with DMAc to 15%. Then, PEG 400 (Sigma-Aldrich) was added into the 15wt.% PBI/DMAc solution resulting in the weight ratio of 15 PBI : 85 DMAc : 5 PEG. This solution was added into a capped glass bottle rotating at 75 °C overnight. The solution was allowed to cool down and stand statically for 1 day to degas. About 1 mL of the polymer solution was cast on the mesh disc (diameter of 22 mm, thickness of 370 μm) on a flat glass plate via a casting knife with a set thickness of 130 μm above the mesh surface. Immediately after casting, the membrane was gently transferred into a water bath with temperature set at 50 °C, where it was shaken for 3 min. Water was gradually exchanged out of the membrane in methanol and hexane baths and finally the membrane was dried under air flow.

4.2.6 Vacuum filtration of the OSDA-free nanosheets

A simple vacuum filtration method was used to coat the OSDA-free nanosheets onto porous PBI or silica support[13]. The silica support was made according to a previous report[13]. The coating was then dried at ambient temperature for 1 day.

4.2.7 Characterization

The powder XRD measurements were carried out using a Bruker-AXS (Siemens) D5005 diffractometer with a CuKα (λ = 0.15406 nm) radiation source with a step of 0.04° and

dwell time of 1s. Scanning electron microscopy (SEM) images were acquired using JEOL 6700 microscope operating at 5 kV. Prior to the observations, the suspension was drop-coated on a silicon wafer, which was attached to a platform by conductive tape, and dried at room temperature. Conventional transmission electron microscopy (CTEM) was performed on a FEI Tecnai G2 F30 (S)TEM with TWIN pole piece, a Schottky field-emission electron gun operating at 300 kV and equipped with a Gatan 4k × 4k Ultrascan CCD. Imaging and diffraction data collection was performed under low electron dose (< 2 e-/Å/s) to minimize electron beam damage of the zeolite sample. TEM samples were prepared by drop-casting suspensions of nanosheets in water on TEM grids (ultrathin carbon film on holey carbon support film, 400 mesh Cu, Ted Pella). The grid was dried at room temperature and imaged. Thermogravimetric analysis (TGA) was performed using a ShimadzuTGA-50 analyzer. Analysis was carried out by heating about 6 mg of the samples in air flow (100 mL/min) from 100 to 750 °C at a heating ramp rate of 10 °C/min. Atomic force microscopy (AFM) was carried out in tapping mode in the repulsive regime using a Bruker Nanoscope V Multimode 8 AFM[31]. The supported nanosheets were prepared in a Langmuir-trough following the procedure of ref[31] and they were calcined in air flow at 400 °C for 4 h. Argon adsorption–desorption isotherms were obtained using a Quantachrome Autosorb-iQ instrument at 87 K. Samples were degassed at 120 °C for 12 h under vacuum prior to the analysis. For the butane isomer single-component gas permeance measurements, the PBI membrane coated with OSDA-free nanosheets was glued onto a metal washer with an epoxy. The pressure rise in a fixed volume permeate side was recorded and used to calculate the permeance and ideal

selectivity.[9]

4.3 Results and discussion

First, it was determined that sonication-only did not alter significantly the multi-lamellar stacking. Mild acid treatments followed by sonication showed similar outcomes. These failed attempts directed us to explore more aggressive approaches. Piranha solution is known as one of the strongest oxidizing agents used to remove organic residues. It was used here to decompose the OSDA in ML-MFI. The as-synthesized ML-MFI was treated with the fresh piranha solution at 80 °C for 1 day. Thermogravimetric analysis (TGA) indicates that the weight loss (in the 120~700 °C range) decreased from ~35% (as-synthesized ML-MFI) to 12.7% after the first piranha solution treatment (**Figure 4.2**). The weight loss further decreased to 6.0% when the above as-obtained product was treated by piranha solution for a second time under the same conditions and ultimately to 2.6% after the fourth treatment (**Figure 4.2**).

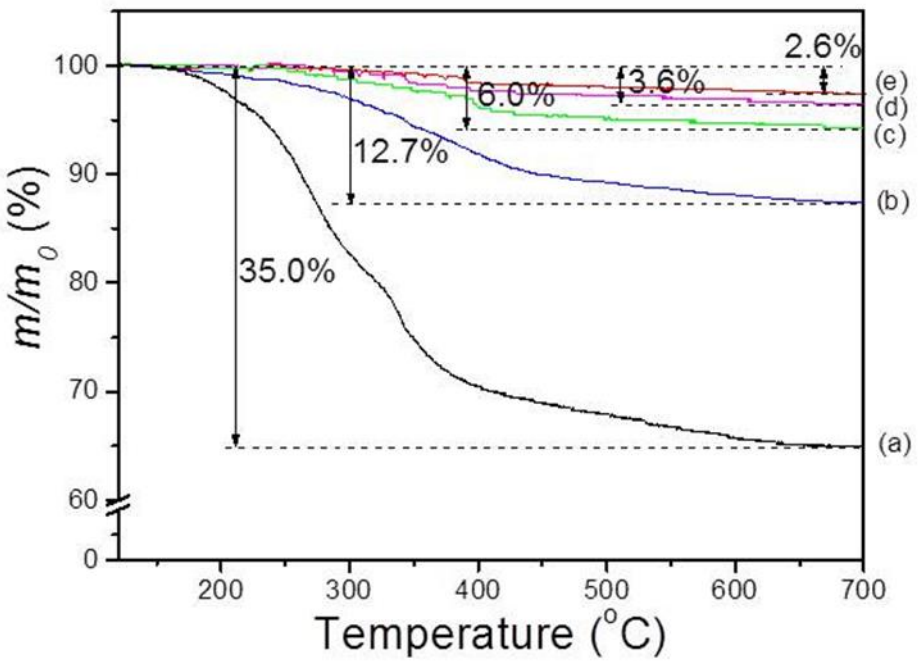

Figure 4.2. Thermogravimetry (TG) curves of ML-MFI zeolites before and after piranha solution treatment. a, as-synthesized ML-MFI. b-e, after piranha solution treatment at 80 °C for 1 d repeated for: one (b), two (c), three (d), and four times (e).

Argon adsorption shows increasing micropore volume after four times treatment (**Figure 4.3**). The same sample calcined at 550 °C exhibits similar micropore volume. These results suggest that most of the organic species were removed and the majority of the micropores were opened after the repeated piranha solution treatment.

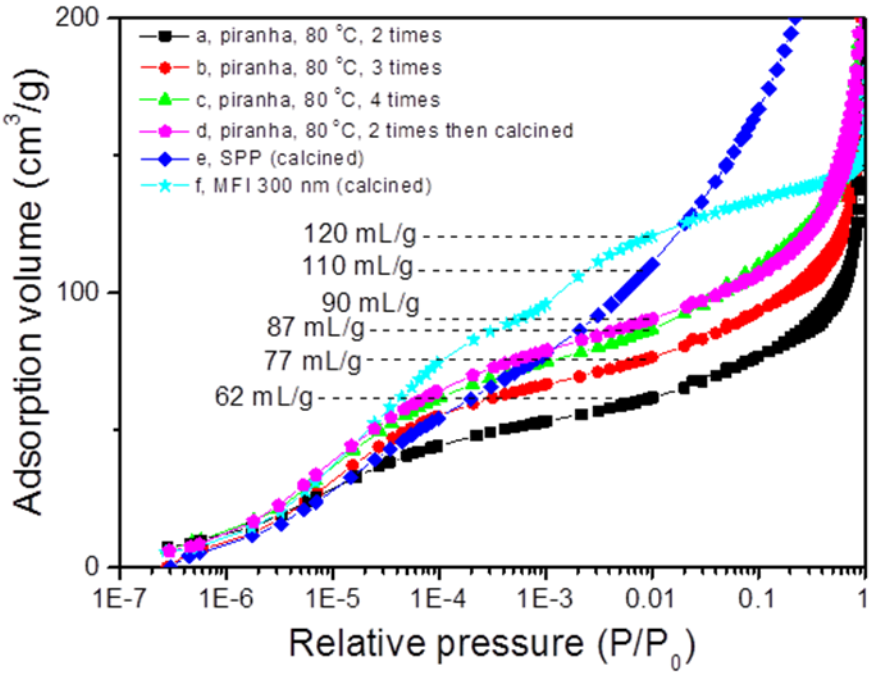

Figure 4.3. 87 K Argon adsorption isotherms of treated ML-MFI. a-c, Argon adsorption isotherms of ML-MFI zeolites after repeated piranha solution treatment at 80 °C for 1 d repeated for: two (a), three times (b), and four times (c). d-f, Argon adsorption isotherms of two-times piranha treated ML-MFI followed by calcination (d), calcined SPP (single unit cell self-pillared MFI) (e), and calcined 300 nm MFI zeolite (f).

Additionally, the piranha solution treated samples preserved the MFI crystallinity at all treatment stages, as confirmed by the presence of MFI-peaks in the wide-angle XRD region (**Figure 4.4**). ^{29}Si MAS NMR data (**Figure 4.5**) indicated that the Q3/(Q3+Q4) ratio in the piranha treated samples decreased in comparison to that of the as-synthesized ML-MFI (0.17 vs. 0.21) and remained unaltered as the number of piranha treatments increased. At the same time, the low angle XRD peaks, which correspond to the layered structure, completely disappeared after four times treatment, indicating the loss of multi-lamellar stacking. A six times piranha treated ML-MFI sample did not show changes in

XRD (**Figure 4.4**) and ^{29}Si MAS NMR (**Figure 4.5**).

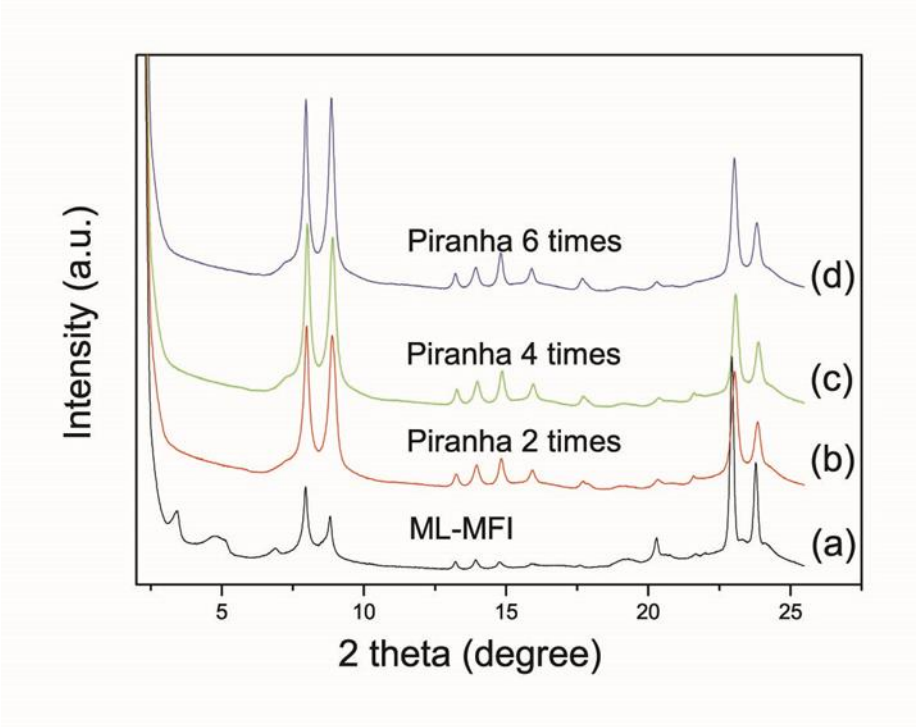

Figure 4.4. XRD patterns of as-synthesized and piranha solution treated ML-MFI. a, As-synthesized. b-d, after piranha solution treatment at 80 °C for 1 d repeated for: two (b), four (c), and six times (d).

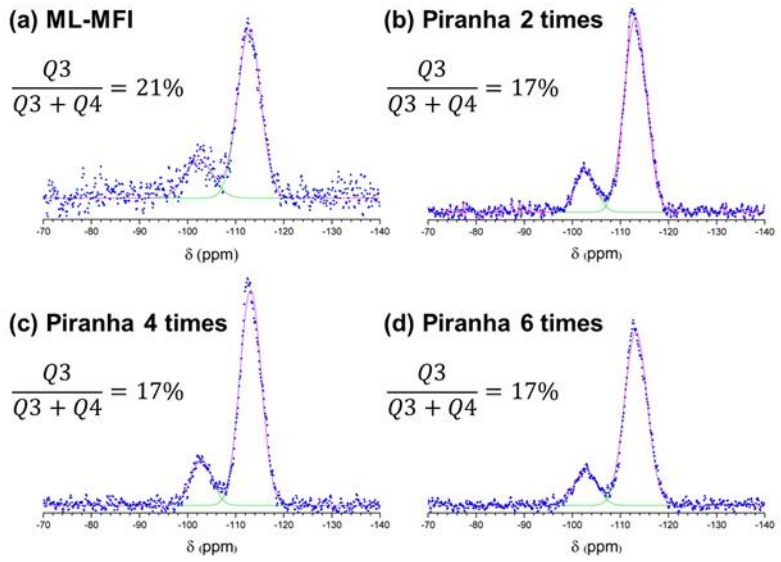

Figure 4.5. ^{29}Si MAS NMR of as-synthesized and piranha treated ML-MFI. a, As-synthesized. b-d, after piranha solution treatment at 80 °C for 1 d repeated for: two (b), four (c), and six times (d). The Q3/(Q3+Q4) ratios are indicated in the Figure. ^{29}Si MAS NMR spectra were obtained with 2000 sec recycle delay (a) and 60 sec recycle delay (b-d). These solid-state ^{29}Si MAS NMR spectra were recorded at 99.4 MHz using a 4 mm Bruker MAS probe with samples spinning at 8 kHz on a Bruker DSX-500 (11.7 T) spectrometer. A $\pi/2$ pulse of 4 μs and strong ^{1}H decoupling pulse with two pulse phase modulation (TPPM) were employed for signal averaging.

After treating ML-MFI with piranha solution, single-layer exfoliated nanosheets (**Figure 4.6a**) were obtained mixed with larger aggregates (**Figure 4.6b**). The exfoliated nanosheets have lateral dimensions of up to 1 μm. 1.5-unit-cell MFI nanosheets with in-plane size larger than 1 μm have not been reported before (earlier reports indicate basal dimensions up to 200 nm[36]).

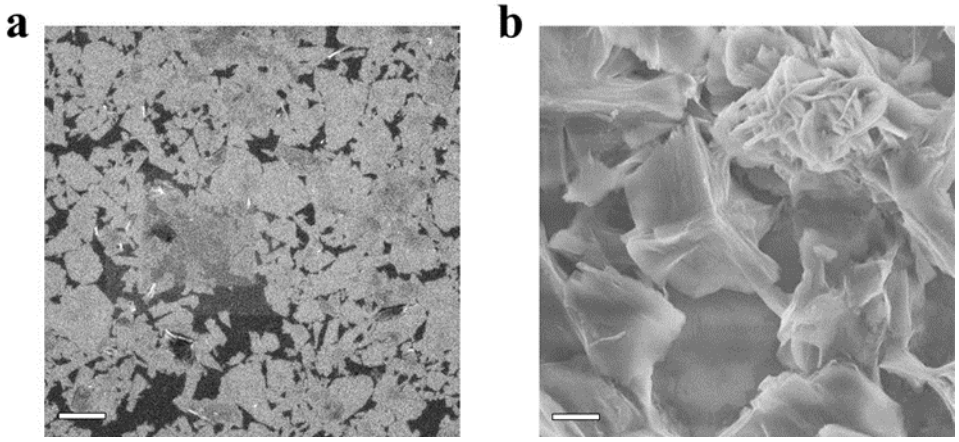

Figure 4.6. SEM images of the particles obtained after direct piranha solution treatment of ML-MFI. a, Exfoliated single layer MFI nanosheets. b, Remaining non-exfoliated particles. Scale bars are 1 µm.

Conventional transmission electron microscopy (CTEM) shows the co-existence of non-exfoliated ML-MFI with individual layers stacked together (**Figure 4.7a**) and exfoliated nanosheets (**Figure 4.7b**). For the non-exfoliated portion, the MFI layers are arranged with a rotational misorientation about the [010] direction, visible by the circular streaking of spots shown in the [010]-zone-axis selected-area-electron-diffraction (SAED) pattern shown in **Figure 4.7c**. The exfoliated nanosheets exhibit the expected SAED pattern (**Figure 4.7d**) suggesting that the MFI crystal structure is preserved, which is further confirmed by high resolution transmission electron microscopy (HRTEM) imaging (**Figure 4.7e**).

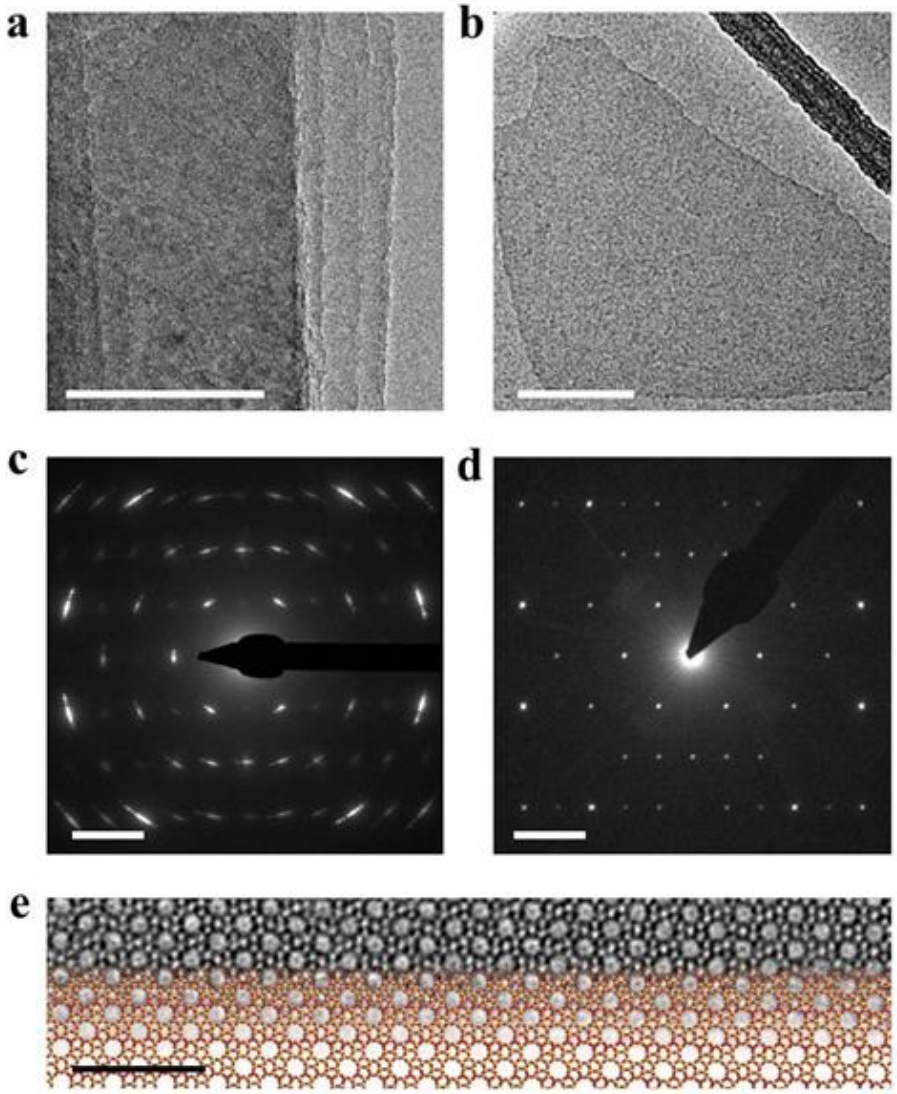

Figure 4.7. (a), (b) Conventional transmission electron microscopy (CTEM) image of non-exfoliated ML-MFI showing multiple sheets stacked together (a) and exfoliated MFI nanosheet (b); (c),(d) [010] zone axis diffraction patterns of non-exfoliated ML-MFI (c) and exfoliated nanosheets (d); (e) High resolution Weiner filtered BF-TEM image of exfoliated MFI nanosheet with overlaid crystal structure viewed along the *b*-axis of MFI. Scale bars in (a) and (b) are 100 nm, (c) and (d) are 1 nm^{-1}, (e) is 5 nm.

AFM imaging shows that the uniform thickness of exfoliated nanosheets is 3.2 nm

(corresponding to 1.5-unit-cell-thick) in good agreement with earlier report (data not

shown here).[31,69,70] Bath sonication followed by horn sonication can cause further exfoliation of the piranha solution treated samples, while vortexing and shaking are not effective (**Figure 4.8**). These results demonstrate that direct piranha solution treatment of ML-MFI removed the majority of the OSDA from both inside and between the MFI nanosheets leading to the formation of exfoliated MFI nanosheets with open pores. However, a fraction of non-exfoliated particles remained.

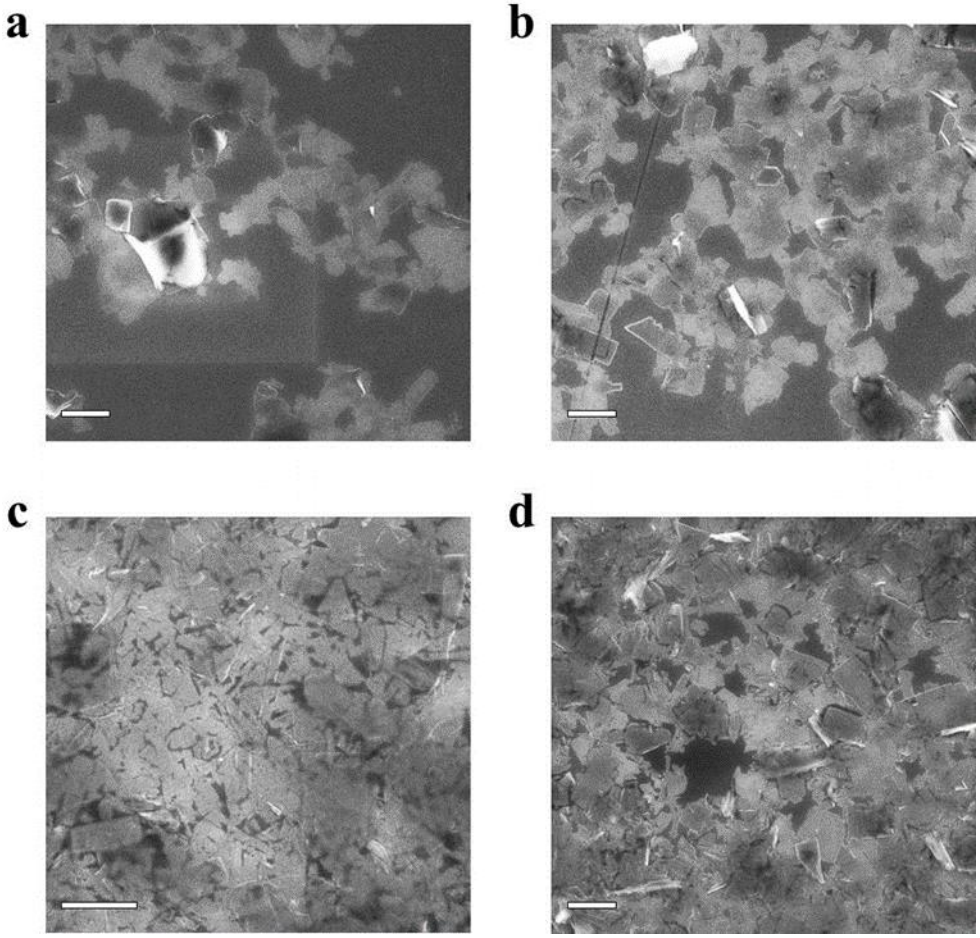

Figure 4.8. SEM images of MFI nanosheets in water suspension prepared by piranha solution treatment of ML-MFI followed by different agitation methods. a, Vortexing for 10 min, repeated three times. b, Shaking for 12 h. c, Horn sonication, 10 min. d, Bath sonication, 90 min. All the suspensions were allowed to sediment for 3 days and then each supernatant was drop-coated on a silicon wafer for SEM observation. Scale bars in a, b and d are 1 μm; scale bar in c is 0.5 μm.

A 3 μm coating on a porous polybenzimidazole (PBI) support was made by vacuum filtration of the aqueous suspension produced after piranha treatment of ML-MFI for four times (**Figure 4.9**). However, butane isomer single gas permeation tests showed no *n*-/*i*-butane ideal selectivity. This could be attributed to defects formed by the remaining non-exfoliated particles (**Figure 4.6b**).

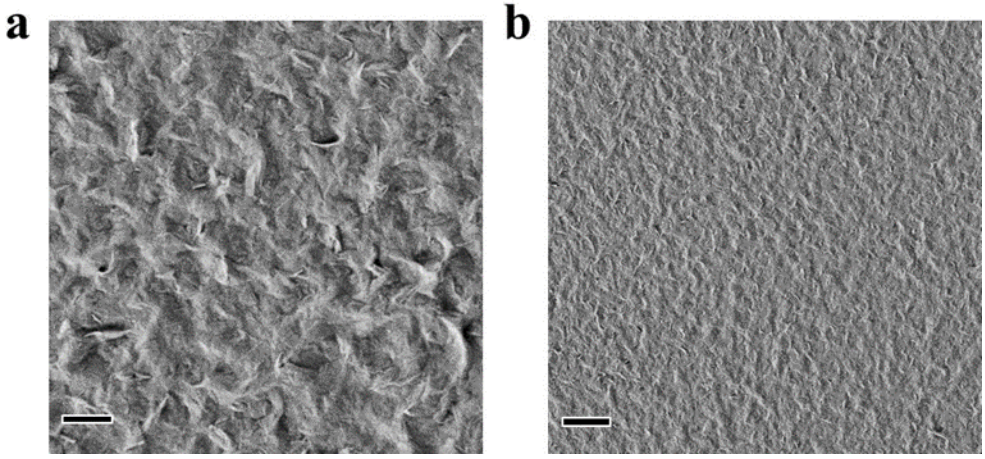

Figure 4.9. Different magnification SEM top-view images of the coating deposited on porous PBI support by filtering the aqueous suspension prepared by four-time piranha solution treatment of ML-MFI. Scale bar in a is 2 μm; scale bar in b is 10 μm.

Future work on purification of exfoliated nanosheets may overcome this problem, but here we decided to add a polymer melt-blending step before the piranha solution treatments (**Figure 4.10a**), attempting to reduce the amount of remaining non-exfoliated particles.

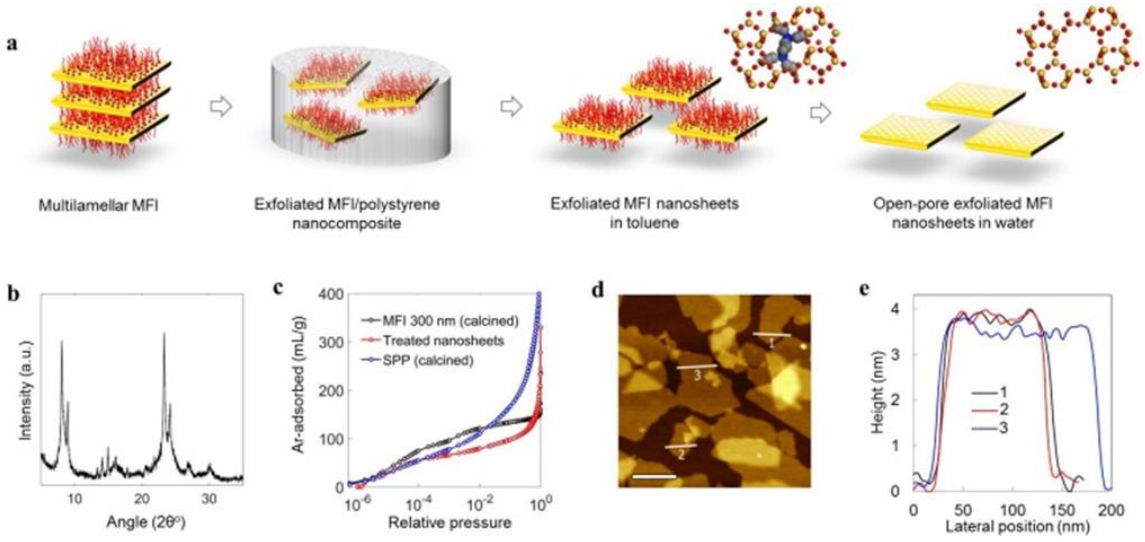

Figure 4.10. (a) Schematic of procedure for the preparation of OSDA-free MFI nanosheet aqueous suspension by the application of piranha solution treatment to exfoliated nanosheets. The ML-MFI is exfoliated by melt-blending with polystyrene (PS). After PS removal, the suspension of exfoliated MFI nanosheets in toluene is obtained. The exfoliated MFI nanosheets are further treated with piranha solution for four times to remove the OSDA from the micropores; (b) XRD pattern of the OSDA-free nanosheets after four-time piranha solution treatment; (c) Argon adsorption isotherms of calcined 300 nm MFI particles, calcined self-pillared single unit cell MFI (SPP) particles, and four time piranha solution treated exfoliated nanosheets; (d) AFM (tapping mode) topographical image of OSDA-free nanosheets (exfoliation followed by four piranha solution treatments) coated on Si wafer by the use of a Langmuir trough; scale bar is 200 nm; (e) Plots of the height vs. length data along the lines highlighted in (d).

The ML-MFI samples were mixed with oligomeric PS (M_w~1,300 g/mol) inside a melt-compounder and the obtained nanocomposite was dissolved in toluene and washed by repeated centrifugation to remove the PS oligomer. The ethanol-washed cake of exfoliated nanosheets was further treated with piranha solution for four times followed by washing and finally, dispersed in deionized (DI) water (**Figure 4.11**). The resulting nanosheets preserved the MFI crystallinity as confirmed by their XRD pattern (**Figure 4.10b**). Argon adsorption (80 mL/g adsorbed at $P/P_0 = 0.01$) is somewhat lower than that

of typically calcined MFI and coincides with the adsorption isotherm of calcined 2D-MFI (SPP)[71] below $P/P_0 \sim 3\times10^{-4}$ (**Figure 4.10c**). The thickness of the resulting nanosheets is 3.2 nm as confirmed by AFM (**Figure 4.10d**), which is the typical 1.5-unit-cell-thick of the single layer nanosheets in ML-MFI. TEM imaging and electron diffraction (**Figure 4.12**) also confirmed the uniform thickness and MFI crystallinity after the treatment.

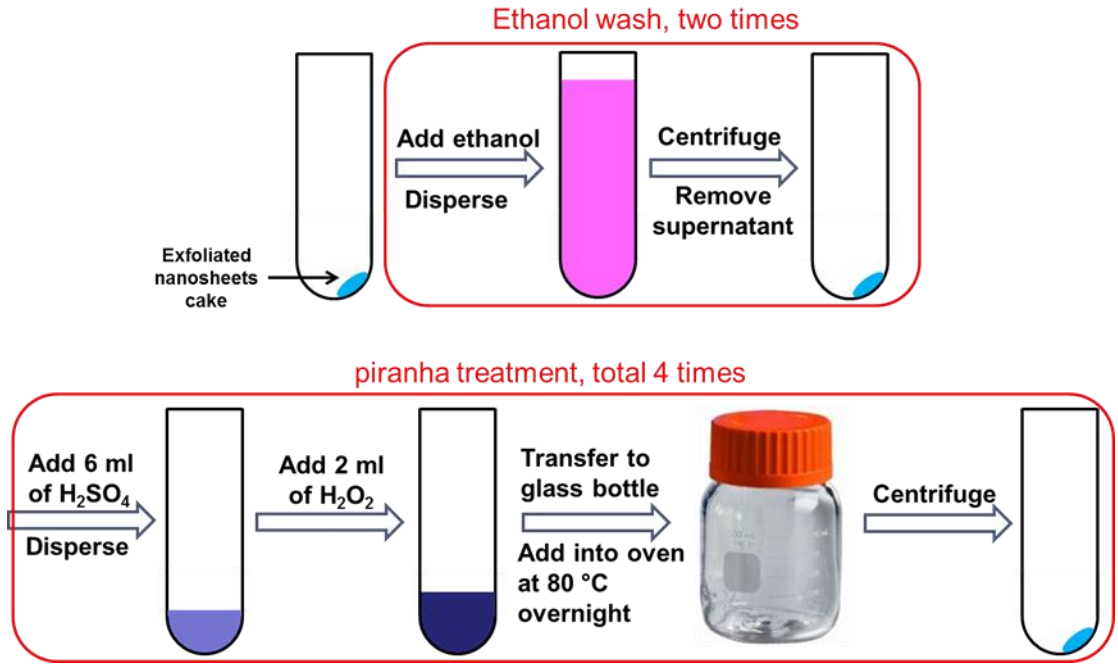

Figure 4.11. Schematic of procedure for piranha solution treatment of nanosheets exfoliated by melt-compounding.

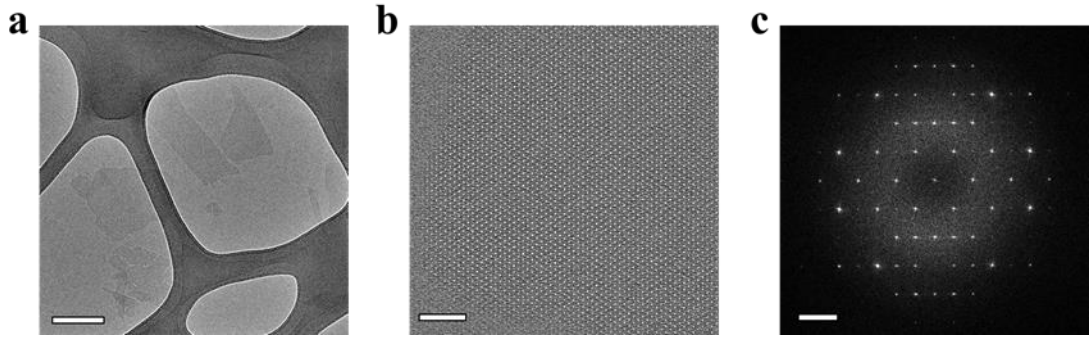

Figure 4.12. TEM imaging of OSDA-free nanosheets via piranha solution treatment of exfoliated (by melt-blending) nanosheets. a, TEM image of exfoliated MFI nanosheets obtained by melt-blending followed by Piranha treatment. Scale bar is 200 nm. b, High-resolution Weiner filtered TEM image of a nanosheet. Scale bar is 10 nm. c, Fast fourier transform (FFT) of image in b showing spots typical of MFI crystal structure down [010]-zone axis. Scale bar is 1 nm^{-1}.

The OSDA-free nanosheet suspension can be used to form self-standing and supported films. For example, it was used to coat nanosheets onto porous silica support via vacuum filtration followed by drying at 80 °C for 3 h. A transparent film was formed that spontaneously peeled off from the silica support surface. This self-standing film (**Figure 4.13a**) is flat and crack-free. The cross-section SEM image (**Figure 4.13b**) shows that its thickness is about 5 µm and it consists of closely packed oriented nanosheets.

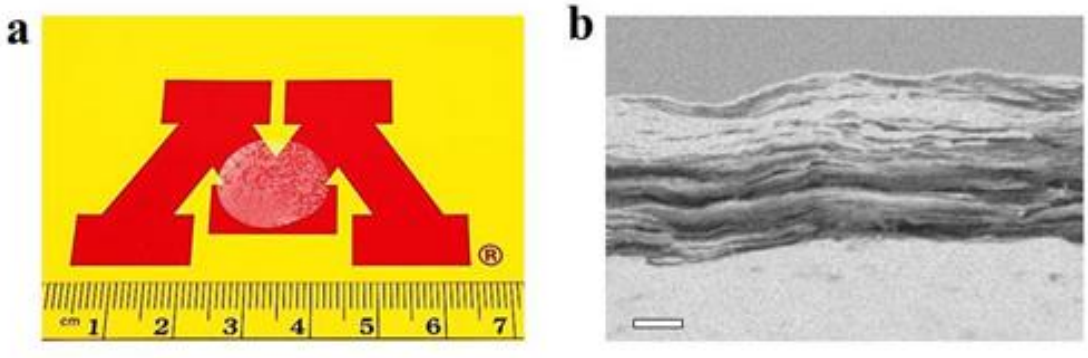

Figure 4.13. (a) Photograph of self-standing disc peeled off from a porous silica support after its formation by filtration; (b) Cross-section SEM image shows

thickness of approximately 5 µm; scale bar is 1 µm.

The suspension can also be used to form films that do not peel-off their supports. **Figure 4.14** shows photos and SEM images of a porous PBI support before and after nanosheet deposition. A uniform and well-packed nanosheet coating covers the PBI support (**Figure 4.14b**). It does not peel-off and, without any further treatment (i.e., without secondary growth and calcination), exhibits membrane separation performance that is characteristic of MFI micropores with *n*-butane over *i*-butane selectivity of 5.4 (**Table 4.1**). This ideal selectivity is about one order of magnitude smaller than that (47~62) achieved by well-intergrown MFI membranes made by secondary hydrothermal growth of a nanosheet deposit on ceramic supports followed by calcination.[72] However, it provides clear evidence that isomer selective molecular sieving from a membrane made by 2D porous layers is feasible. The permeances obtained by the current membranes are comparable to the ones obtained by intergrown membranes. Further characterization is required to assess the reasons for the lower selectivity. Most likely, the cause of lower selectivity is a combination of defects in between the layers providing non-selective transport pathways and partial blocking of selective pathways by overlapping nanosheets. Although gas separations using graphene oxide,[73,74] MOF exfoliated layers,[75] and calcined zeolite flake composite films[9] have been reported, selectivity for hydrocarbon isomers from directly deposited molecular sieves have not been demonstrated. Since no secondary growth and high temperature post-activation are required, such OSDA-free nanosheets open the opportunity of large-scale membrane fabrication on low-cost polymer supports (flat sheets or hollow fibers), which could drastically reduce membrane manufacturing

cost.[76] Further improvements in nanosheet aspect ratio and packing are likely to result in better performance. Moreover, the water/nanosheet dispersions can be used with other film formation approaches beyond the filtration-coating demonstrated here, including layer-by-layer, slip-coating, and Langmuir-trough based methods to form MFI films for membrane and other applications. They can also be used in the formation of nanocomposites including “selective flake” mixed matrix membranes.[9,77]

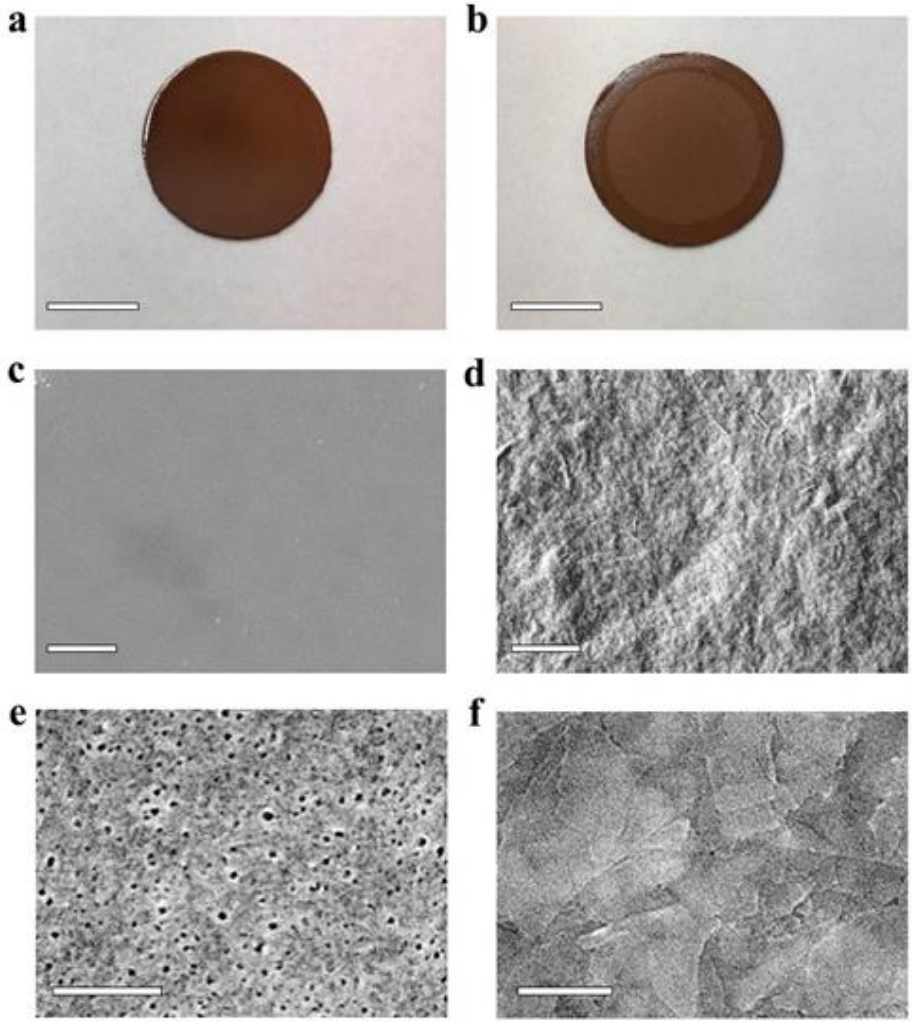

Figure 4.14. (a),(b) Photographs of porous PBI support before (a) and after (b) filtration of aqueous suspension of OSDA-free MFI nanosheets; (c),(d) Top-view

SEM images of porous PBI support before (c) and and after (d) filtration of aqueous suspension of OSDA-free MFI nanosheets; (e),(f) High magnification views of portions of (c) and (d), respectively. Scale bars in (a) and (b) are 10 mm; scale bars in (c) and (d) are 2 μm; scale bars in (e) and (f) are 200 nm.

Table 4.1 *n*-/*iso*-Butane single gas ideal selectivity and permeance of the OSDA-free nanosheets coated on PBI porous support (room temperature and atmospheric pressure feed). Data from five different membranes are shown.

Membrane	n-Butane permeance (mol/m^2-s-Pa)	Ideal selectivity
1	3.7×10^{-7}	5.5
2	3.8×10^{-7}	5.5
3	3.5×10^{-7}	5.4
4	3.3×10^{-7}	5.4
5	3.2×10^{-7}	5.3
Average	$(3.5\pm0.3)\times10^{-7}$	5.4±0.1

4.4 Conclusion

A method for template-free zeolite MFI nanosheets has been demonstrated. The templates were removed by piranha solution treatment while the crystallinity was still preserved. The deposit of these open-pore nanosheets on porous polybenzimidazole support without further treatment exhibited n-/i-butane ideal selectivity of 5.4 with n-butane permeance of 3.5×10^{-7} mol/m^2-s-Pa.

Chapter 5. Polybenzimidazole Ultrafiltration Hollow Fiber Membranes Fabricated from High Temperature Coagulation Bath

* To be submitted

5.1 Introduction

Polybenzimidazole (PBI), typically synthesized via condensation reaction of aromatic tetraamines and dicarboxylates, is a generic name for a family of aromatic heterocyclic polymers containing benzimidazole units. Since the first successful synthesis of highly thermo-chemically stable and mechanically robust aromatic polybenzimidazoles[78], extensive researches have been carried out to optimize and utilize their high performance properties.

In the membrane community, PBIs have been explored for various separation purposes especially at elevated temperatures and in harsh environments. Many efforts were dedicated to develop PBI semi-permeable membranes for reverse osmosis[79–83], fuel cells[84–89], nanofiltration[90–96], forward osmosis[97,98], pervaporation[99–104], gas separation[105–109], ultrafiltration[110–113], etc.

As for ultrafiltration PBI membranes, only limited papers and patents are present in the literature[110–113], most of which have flat sheet configuration. Sansone and co-workers[110] studied the fabrication of PBI flat membranes for ultrafiltration applications. The prepared membranes are promising with respect to their highly thermal and chemical resistance and improved mechanical strength. Xing et al.[111] fabricated PBI flat ultrafiltration membranes using an ionic liquid, 1-ethyl-3-methylimidazolium acetate ([EMIM]OAc), as a green solvent. [EMIM]OAc is more environmentally friendly compared to the conventional organic solvents used in membrane fabrication processes.

Bhagat et al.[112] prepared PBI flat ultrafiltration membranes containing *t*-butyl group (PBI-BuI). The pure water permeance and molecular weight cut-off (MWCO) of the prepared membrane fall under ultrafiltration category.

Compared with flat sheet configuration, hollow fiber membrane modules have much higher surface area to volume ratio, thus representing the optimal configuration for membrane applications. As far as we know, only one patent[113] described the fabrication of PBI hollow fiber membrane applicable for ultrafiltration. The fabricated hollow fiber membrane is claimed to be porous with surface pores greater than about 0.05 μm and less than about 1 μm, and further crosslinked with dibromobutane (DBB) to be solvent resistant. However, microporous membranes may sometimes be insufficient in applications where the required membrane pore sizes are less than 50 nm. Here, we will show a facile approach for chemically and mechanically stable PBI hollow fiber membranes with surface pore sizes ranging from 2 to 40 nm.

5.2 Experimental

5.2.1 Materials

PBI/DMAc solution (20 wt%, IV=1.1, without LiCl) was purchased from PBI Performance Products, Inc (Charlotte, NC). Chemicals including *N*,*N*-dimethylacetamine (DMAc), n-methyl-2-pyrrolidone (NMP), polyvinylpyrrolidone (PVP), n-propanol, ethylene glycol (EG), methanol, hexane, dibromobutane (DBB), methyl isobutyl ketone (MIBK), poly(ethylene glycol) (PEG) (with molecular weights of 400, 4,000, 40,000) and poly(ethylene oxide) (PEO) (with molecular weights of 100,000, 200,000, 300,000, 400,000), were purchased from Sigma-Aldrich.

5.2.2 PBI hollow fiber spinning

The compositions of dope and bore solutions were summarized in **Table 5.1**. The dope solution was prepared inside an air-tight glass bottle rotated in oven at 70 °C for 24 h. The solution was then transferred to the dope reservoir and rest for 24 h to remove the bubbles. The bore solution was mixed with magnetic stirring for 1 h. For hollow fiber membrane spinning, dope and bore solutions were co-extruded through a spinneret (as shown in **Figure 5.1**) by two pumps, respectively. The extruded liquid passed through an air gap and then into a water coagulation bath. If needed, the coagulation bath temperature was increased to 60 °C or 80 °C by circulating heated water for at least 12 h before spinning. The collected fibers were cut into 30 cm pieces and soaked in water for 36 h, followed by immersion in methanol for 36 h, and last in hexane for 36 h. During the soaking in each solvent, the solvent was refreshed every 12 h. The fibers were then dried at ambient temperature overnight.

Table 5.1. Dope and bore compositions

Solutions		Batch I	Batch II	Batch III	PBI-60	PBI-80
Dope	PBI	16.8%	16.8%	16.8%	16.8%	16.8%
	DMAc	76.5%	76.5%	76.5%	76.5%	76.5%
	PEG400	2.4%	4.2%	4.2%	4.2%	4.2%
	PVP	1.8%	0	0	0	0
	n-Propanol	2.1%	2.1%	2.1%	2.1%	2.1%
	H_2O	0.4%	0.4%	0.4%	0.4%	0.4%
Bore	EG	50%	50%	0	0	0
	DMAc	50%	50%	86%	86%	86%
	H_2O	0	0	14%	14%	14%

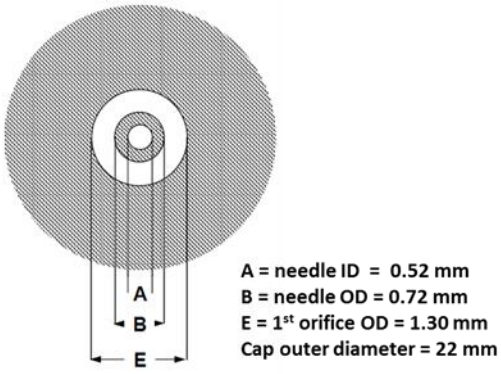

Figure 5.1. Dimensions of the spinneret.

5.2.3 Post-thermal treatment

Before further gas permeation and ultrafiltration test, the PBI hollow fiber membranes were thermally treated at 300 °C with air flow at 110 ml/min for 8 h with both ramping and cooling rates of 0.5 °C/min. The thermally treated fiber became highly organic solvent stable and resistant to the deformation after dried directly from water.

5.2.4 Gas permeation test

A piece of hollow fiber with length of ~2 cm was used for the N_2 gas permeation test. One end of the fiber was blocked with epoxy, and the other end was connected to a glass tube with epoxy. The N_2 gas was fed outside the hollow fiber. The glass tube was connected to a vacuum pump so that the inner side of hollow fiber was under vacuum. To measure the N_2 permeance, the hollow fiber and vacuum pump was disconnected by a valve and the pressure increase of the inner side of the hollow fiber was recorded as a function of time, which was further used to calculate the N_2 permeance.

5.2.5 Ultrafiltration experiments

The pore sizes were characterized by ultrafiltration of 200 ppm PEG or PEO aqueous solution with outside-in mode. A piece of hollow fiber with length of ~30 cm was sealed

inside a module with one end fully blocked by epoxy[114]. Before ultrafiltration experiments, pure DI water was used to wash the hollow fiber for 1 h with feed pressure of 20 psi. Feed solution (PEG or PEO aqueous solution, 200 ppm) was then introduced into the hollow fiber membrane module by a peristaltic pump (Grainger, item#: 3HHF4) with constant pressure (gauge) at 25 psi controlled by a needle valve at the retentate side. The permeate and retentate were collected into the feed reservoir to maintain the feed concentration during stabilization for at least 1 h. The permeance of membrane was calculated by **Eq. 5.1**,

$$Permeance = \frac{Q}{\Delta P A} = \frac{Q}{\Delta P \pi D l} \tag{5.1}$$

where Q is the flux (L/h), ΔP is the pressure difference (bar) between feed side and permeate side across the membrane, A is the effective surface area (m^2) of hollow fiber, D is the outer diameter (m) of the hollow fiber, l is the effective fiber length (m) inside the module. The concentration of PEG or PEO in feed or permeate was determined by total organic carbon (TOC) analyzer (Shimadzu TOC-L analyzer paired with Shimadzu OCT-L 8-Port Sampler). The rejection of the membrane was calculated by **Eq. 5.2**:

$$R = \left(1 - \frac{C_P}{C_F}\right) \times 100\% \tag{5.2}$$

where C_F is the total organic carbon concentration of feed solution, Cp is the total organic carbon concentration of permeate solution. According to previous study[115–117], a straight line is yielded when the rejections and corresponding solute diameters were plotted on a log-normal probability paper. The solute diameter can be determined by Einstein-Stokes diameters of PEO and PEG calculated by **Eq. 5.3** for PEG and **Eq. 5.4** for PEO[116,117]:

$$a = 16.73\times10^{-10}M^{0.557} \quad (5.3)$$

$$a = 10.44\times10^{-10}M^{0.587} \quad (5.4)$$

where a is Einstein-Stoke diameter with unit of cm, *M* is molecular weight of solute with unit of g/mol. From the straight line of rejection vs. solute diameter, the molecular weight cut-off (MWCO) of the membrane is the solute molecular weight corresponding to R=90%, and the mean pore size (μ_p) of membrane is corresponding to the solute size when R=50%. The standard deviation (σ_p) is the ratio of solute size at R=84.13% and that at R=50%. With μ_p and σ_p determined, the pore size distribution curves and probability density function curves of the membrane can then be determined[116,117].

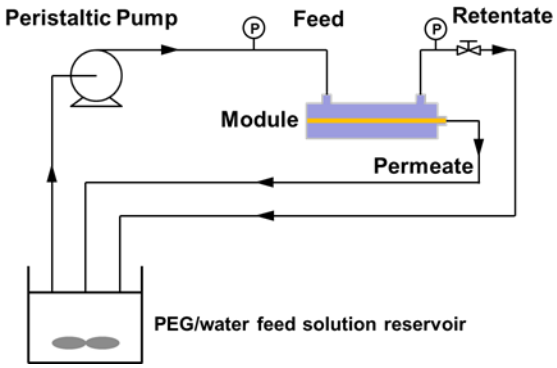

Figure 5.2. Schematic of PBI hollow fiber ultrafiltration test set-up.

5.2.6 Scanning electron microscopy

SEM images were acquired using JEOL 6700 microscope operating at 5 kV and 10 µA with SEI mode. All the hollow fiber samples were sputter coated with 30 Å Pt layer before examination. The cross section of the sample was made by fracture of the fiber in liquid nitrogen.

5.2.7 Mechanical property

The two ends of the hollow fiber were sandwiched by two cardboards with epoxy, with effect length of about 4 cm between the two epoxy ends. The two ends were then griped by the metal fixture in the RSA G2 Solids Analyzer (TA instruments) for tensile stress test. For each sample, the tests were repeated 3 times.

To prepare the crosslinked hollow fibers as comparison[113], the fiber was soaked in 5% dibromobutane (DBB) dissolved in methyl isobutyl ketone (MIBK) at 100 °C for 16 h, followed by air-dried for 1 h. It was then heated at 150 °C for 3 hours.

5.3 Results and discussion

5.3.1 PBI hollow fibers spun from coagulation bath at ambient temperature

The geometry and properties of the hollow fiber membranes were controlled by several spinning parameters including dope solution flow rate, bore solution flow rate, gap distance, take-up speed, and coagulation bath temperature. The dope and bore solution compositions were shown in **Table 5.1**. The spinning parameters, corresponding fiber dimensions, and N_2 permeance were summarized in **Table 5.2**.

First, the hollow fibers spun with coagulation bath at ambient temperature (batch I, II, and III) were examined by SEM imaging. The outer diameter (OD), inner diameter (ID), and wall thickness were summarized in **Table 5.2**. The OD of the samples ranged from 525 μm to 1600 μm, the ID ranged from 366 μm to 733 μm, with wall thickness ranged from 80 μm to 494 μm. In general, higher dope and bore solution flow rates, lower take-up speed resulted in larger OD, while higher dope to bore solution flow rate ratio and lower take-up speed led to thicker wall. The typical SEM images of outer surface and

cross section were shown in **Figure 5.3** taken from sample I-#1. The outer surface shown in **Figure 5.3a** was tight without visible surface pores. The cross section was spongy type (**Figure 5.3c**) with finger-type macropores near the outer surface (**Figure 5.3b**). The outer surfaces and cross sections of all the fibers spun from batch I, II, and III were similar (tight surface and spongy-type cross section), although with different dope and bore solution compositions. The inner surface structure was mostly determined by dope solution composition. The inner surface of batch III fibers had higher surface porosity with dope solution of 86% DMAc and 14% H_2O (**Figure 5.4c**), compared with batch I and II fibers with dope composition of 50% DMAc and 50% EG (**Figure 5.4a** and **b**). This was also confirmed by the much higher N_2 permeance (92.5 and 140.0×10^{-7} mol/(Pa-s-m^2)) from batch III fibers. Specifically, sample II-#1 and III-#1 had the same dope solution composition and spinning parameters, but different bore solution composition, while the N_2 permeance of sample III-#1 was ~50 times higher than that of sample II-1. Thus, according to all these results, tight surface and spongy type cross section were obtained when the coagulation bath temperature was at room temperature, although with different dope and bore solution compositions. The inner surface became more porous with higher DMAc concentration in bore solution.

Table 5.2. Spinning parameters for batch I, II, III, PBI-60, and PBI-80

Sample	Bath temperature (°C)	Gap (mm)	Dope speed (ml/min)	Bore speed (ml/min)	Dope speed: Bore speed	Take-up speed (m/min)	N_2 permeance (10^7 mol/(Pa-s-m^2))	Outer diameter (μm)	Inner diameter (μm)	Wall thickness (μm)
I-#1	24	18	3.0	1.5	2	3.0	1.8	1000.8	660.3	170.3
I-#2	24	18	3.0	1.5	2	6.12	1.8	706.3	460.8	122.8
I-#3	24	18	3.0	1.5	2	9.4	1.0	525.1	365.7	79.7
I-#4	24	18	6.0	3.0	2	3.0	3.1	1357.1	~733.3*	~311.9
I-#5	24	18	6.0	3.0	2	6.2	1.2	1600.1	612.8	493.7
I-#6	24	18	6.0	3.0	2	9.4	0.37	862.9	559.4	151.8
I-#7	24	18	6.0	3.0	2	12.2	0.48	672.3	407.2	132.6
I-#8	24	18	6.0	1.5	4	3.0	3.0	1309.5	~495.2*	~407.2
I-#9	24	18	3.0	3.0	1	3.0	3.2	1166.1	876.1	145.0
I-#10	24	18	3.0	3.0	1	6.2	3.9	713.2	503.9	104.7
I-#11	24	18	6.0	0.75	8	3.0	6.5	1321.7	~343.5*	~489.1
II-#1	24	18	3.6	1.2	3	4.5	1.9	844.4	440.7	201.9
II-#2	24	10	3.6	0.9	4	4.5	2.9	801.9	403.7	199.1
II-#3	24	10	3.6	1.2	3	4.5	3.9	838.9	468.5	185.2
III-#1	24	18	3.6	1.2	3	4.5	92.5	872.9	373.8	249.6
III-#2	24	18	3.6	1.8	2	4.5	140.0	981.5	490.7	245.4
PBI-60	60	18	3.6	2.1	1.7	7.8	275.0	760.9	421.7	169.6
PBI-80	80	18	3.6	2.1	1.7	9.4	565.0	717.4	400.1	158.7

*the shape of lumen is not round.

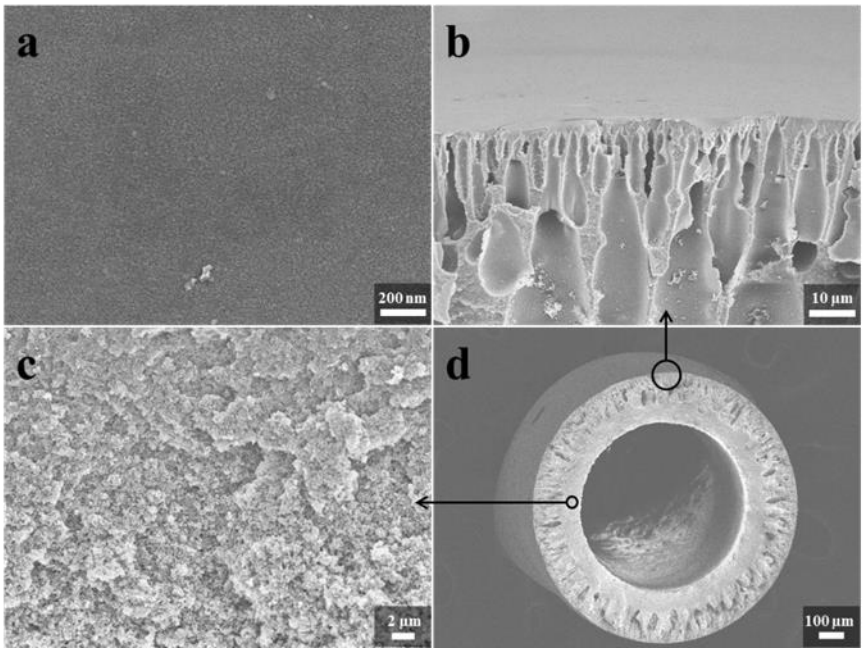

Figure 5.3. SEM images of hollow fiber sample I-#1. a) Outer surface; b), c) and d) cross section with different magnifications and locations.

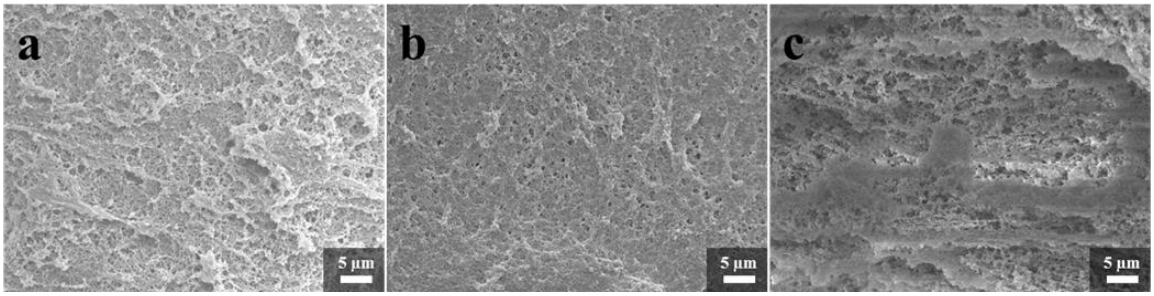

Figure 5.4. SEM images of inner surfaces from sample a) I-#1; b) II-#1; c) III-#2.

5.3.2 PBI hollow fiber spun from coagulation bath at high temperatures

The outer surface structures of the samples from batch I, II, and III were the same, i.e. without observable surface pores, preventing their application for ultrafiltration. Rather than adjustment of dope or bore solution compositions, it was demonstrated that porous outer surface structures with surface pore diameters up to ~40 nm could be achieved, simply by the increase of coagulation bath temperatures, as discussed below.

The dope and bore solution compositions and spinning parameters were shown in **Table 5.1** and **5.2**, which were the same as that of bath III. PBI-60 denoted hollow fibers fabricated with coagulation bath temperature of 60 °C, while PBI-80 denoted that with coagulation bath temperature of 80 °C. The dope and bore solution compositions for PBI-60 and PBI-80 were the same. As shown in **Figure 5.5a**, the outer surface of PBI-60 was porous with surface pore diameter of ~5 nm. Such porous structure was attributed to the increased coagulation bath temperature at 60 °C, considering the tight surface of sample III-#1 from the same dope and bore solution compositions, and similar spinning parameters, except bath temperature at ambient temperature. As the coagulation bath temperature increased further to 80 °C, the outer surface pore diameter also increased to ~15 nm as shown in **Figure 5.6a** for PBI-80. The cross section structures became finger-

type across the whole membrane, compared with spongy-type structures in batch I, II, and III samples (fabricated with coagulation bath at ambient temperature). The inner surfaces of PBI-60 and PBI-80 also became much more porous (**Figure 5.5c** and **5.6c**) compared with those from ambient temperature (**Figure 5.4**). Thus, simply increasing the coagulation bath temperature could result in much more porous outer and inner surfaces, and finger-type structure across the membrane.

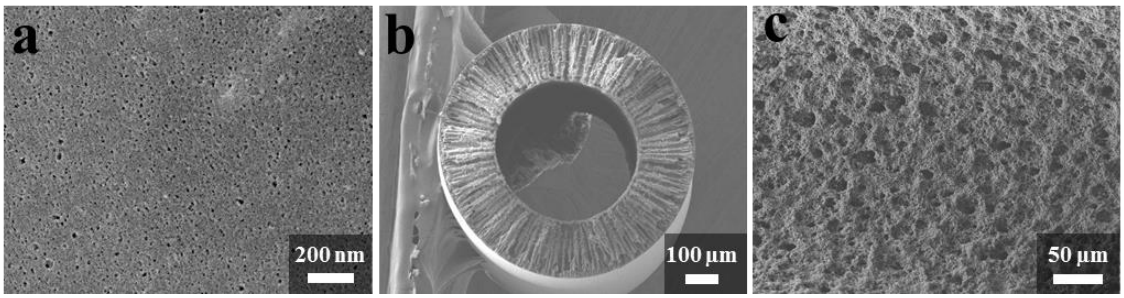

Figure 5.5. SEM images of hollow fiber sample PBI-60. a) outer surface; b) cross section; c) inner surface.

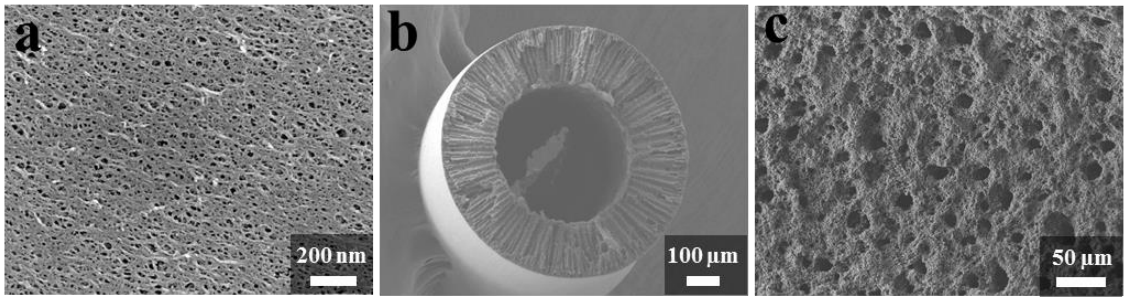

Figure 5.6. SEM images of hollow fiber sample PBI-80. a) outer surface; b) cross section; c) inner surface.

5.3.3 Post-thermal treatment

The neat PBI hollow fiber could deform seriously (right-hand-side fiber shown in **Figure 5.7**) if the water-wetted fiber was allowed to dry directly (without solvent exchange to

hexane), due to the high surface tension of water. This problem can be solved by chemically crosslinking with a crosslinker[94,95,113]. However, this treatment involves multi-step soaking and washing in organic solvents, making it environmentally and economically undesirable. Here, we demonstrated that a simple post-thermal treatment at 300 °C could considerably increase its solvent resistance and mechanical stability to prevent the deformation. As shown in **Figure 5.7** left-hand-side, the thermally treated fiber preserved its geometry after dried directly from water. We hypothesized that PBI underwent crosslinking during the thermal treatment, which should be confirmed in future study. Besides, the thermally treated fiber maintained its geometry and pore structure (proved by SEM imaging, not shown here) after it was soaked in NMP solution at 100 °C for three days, comparing that the neat hollow fiber dissolved within several minutes in NMP solution at ambient temperature.

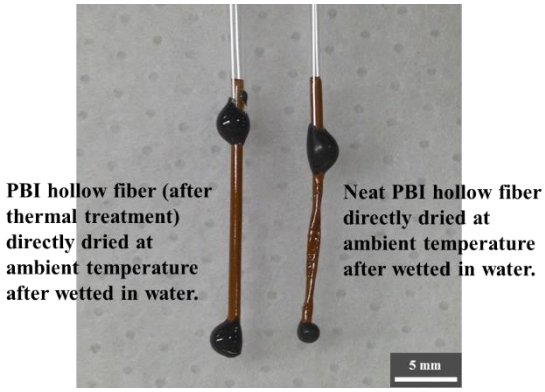

Figure 5.7. Photograph of PBI hollow fibers directly dried at ambient temperature after wetted in water. The left-hand-side fiber, previously treated at 300 °C, kept its original geometry. The right-hand-side fiber, without thermal treatment at 300 °C, deformed seriously.

5.3.4 PBI hollow fiber ultrafiltration performance

The ultrafiltration properties of PBI-60 and PBI-80 were evaluated with PEG and PEO

aqueous solutions with various molecular weights. The results were summarized in **Table 5.3** for PBI-60 and **Table 5.4** for PBI-80. For the ultrafiltration with PEG 6,000 aqueous solution (column of "PEG 6,000" in **Table 5.3**), three PBI-60 fibers with effective length of ~20 cm were individually sealed inside three modules for ultrafiltration test. One module was then assembled into the permeation set-up shown in **Figure 5.2**. First, the fiber was washed with pure water continuously for 1 h to remove the remaining organic species out from the hollow fiber and module. The complete removal of remaining organic species was confirmed by the negligible total organic carbon concentration (<1 ppm) measured from TOC analyzer. The pure water permeance (PWP) was calculated by **Eq. 5.1**. Then, feed solution was changed to PEG 6,000 aqueous solution with total volume of 2 L. After 2 h stabilization, the feed solution and permeate solution (~10 g for each) were collected for measurement by TOC analyzer to determine the PEG concentration. The rejection of PEG 6,000 was then calculated via **Eq. 5.2**. As shown in **Table 5.3**, the solute rejection of PBI-60 increased from 16.0% to 97.6% as the solute molecular weight increased from 6,000 to 100,000. The PEG solution permeance (PEGP) decreased with the increase of solute molecular weight, due to the partial blockage of outer surface. The PEGP was smaller than PWP, which was due to the slow feed solution flow rate of 2.6 L/h in the ultrafiltration experiments, compared with 159 L/h used in the literature[116]. Under such low flow rate, PEG or PEO molecules could easily accumulate on the fiber surface and partially block the surface pores. This pore blockage was more significant with higher PEO molecular weight. Compared the ultrafiltration data of PBI-60 and PBI-80, PBI-80 exhibited higher PWP and smaller solution rejection (with the

same solute molecular weight), indicating bigger surface pore size and higher porosity, which was in consistent with the conclusion from SEM images (**Figure 5.5a** and **Figure 5.6a**).

Table 5.3. PBI-60 ultrafiltration results of pure water permeance (PWP), PEG and PEO solution permeance (PEGP), ratio between PEGP to PWP, and solute rejection.

	PEG 6,000			PEG 20,000		PEO 40,000			PEO 100,000	
Pure water permeance (PWP) (L/(bar-h-m²))	104.7	86.6	102.4	213.9	236.6	155.6	174.0	187.2	134.5	235.6
	Average: 97.9			**Average: 225.3**		**Average: 172.3**			**Average: 185.0**	
PEG or PEO solution permeance (PEGP) (L/(bar-h-m²))	31.5	22.4	22.5	34.5	41.4	14.7	18.7	24.3	12.7	13.1
	Average: 25.5			**Average: 38.0**		**Average: 19.2**			**Average: 12.9**	
Ratio between PEGP to PWP (%)	30.1	25.9	22.0	16.1	17.5	9.5	10.7	13.0	9.4	5.6
	Average: 26.0			**Average: 16.8**		**Average: 11.0**			**Average: 7.5**	
Rejection (%)	9.9	19.6	18.4	37.4	29.1	71.4	85.2	62.7	99.3	95.8
	Average: 16.0			**Average: 33.3**		**Average: 73.1**			**Average: 97.6**	

Table 5.4. PBI-80 ultrafiltration results of pure water permeance (PWP), PEG and PEO solution permeance (PEGP), ratio between PEGP to PWP, and solute rejection.

	PEG 20,000		PEO 40,000		PEO 100,000		PEO 300,000	
Pure water permeance (PWP) (L/(bar-h-m²))	228.3	273.1	314.5	284.2	255.4	284.9	252.1	239.0
	Average: 250.7		**Average: 300.4**		**Average: 270.2**		**Average: 245.6**	
PEG or PEO solution permeance (PEGP) (L/(bar-h-m²))	87.3	58.9	45.9	40.1	13.8	12.8	8.2	9.1
	Average: 73.1		**Average: 43.0**		**Average: 13.3**		**Average: 8.6**	
Ratio between PEGP to PWP (%)	38.3	21.6	14.6	14.1	5.4	4.5	3.2	3.8
	Average: 30.0		**Average: 14.4**		**Average: 4.6**		**Average: 3.5**	
Rejection (%)	2.9	3.6	17.7	19.5	93.3	88.6	98.7	97.8
	Average: 3.3		**Average: 18.6**		**Average: 91.0**		**Average: 98.3**	

To further calculate the mean pore size (μ_p) and MWCO from the PEG or PEO ultrafiltration data, the rejection vs. solute size plots were drawn on a log-normal

probability paper as shown in **Figure 5.8**. The Stokes radii of PEG and PEO were calculated using **Eq. 5.2** and 5.3[116,117]. All these values were summarized in **Table 5.5**. The PBI-60 had smaller MWCO and mean pore size (μ_p) than that of PBI-80. The cumulative pore size distribution and probability density curves for PBI-60 and PBI-80 were shown in **Figure 5.9a** and **b**, which indicated that PBI-60 had a narrower pore size distribution than that of PBI-80.

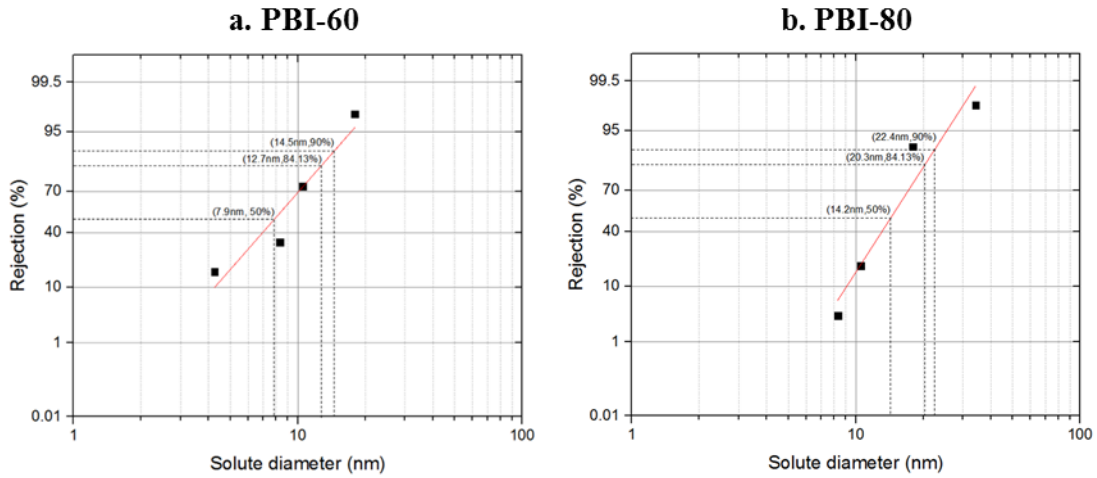

Figure 5.8. Rejections vs. solute diameters plotted on a log-normal probability paper for a) PBI-60 and b) PBI-80.

Table 5.5. MWCO, mean pore size μ_p, and standard deviation σ_p of PBI-60 and PBI-80 calculated from PEG and PEO ultrafiltration data.

Membrane	MWCO (kDa)	Mean pore size μ_p (nm)	Standard deviation σ_p (nm)
PBI-60	70.0	7.9	1.6
PBI-80	145.5	14.2	1.4

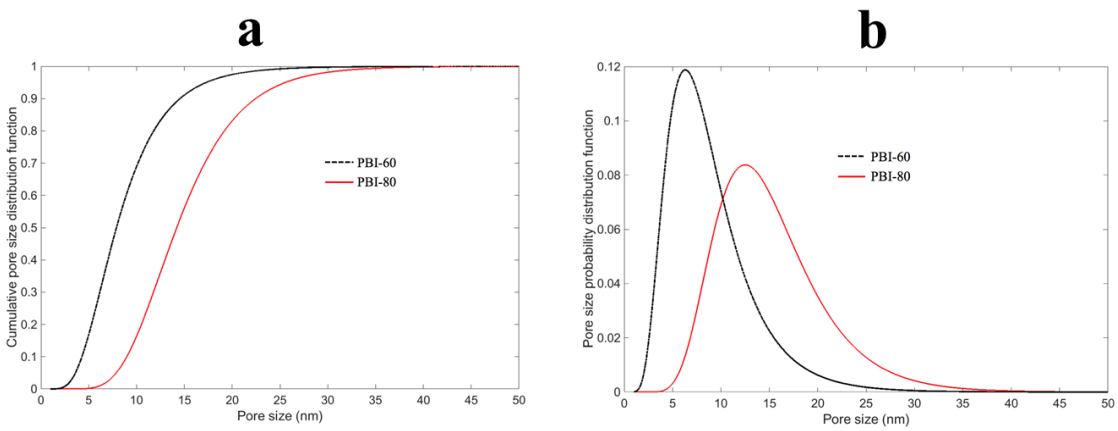

Figure 5.9. Cumulative pore size distribution curves (a) and probability density function curves for PBI-60 (black curves) and PBI-80 (red curves) calculated from ultrafiltration data.

5.3.5 Mechanical property

The tensile stresses and strains at break were summarized in **Table 5.6**. Four samples, original hollow fiber, thermally treated at 300 °C, crosslinked with DBB, thermally treated and then crosslinked, were tested. The tensile stresses for all the samples were similar. The stains at break had the order of original > crosslinked >thermally treated and crosslinked > thermally treated.

Table 5.6. Tensile stresses and strains at break for original, thermally treated, crosslinked, thermally treated and crosslinked fibers

Hollow fiber sample	Run	Initial length (mm)	Final length (mm)	Strain at break (%)		Force at break (g)	Tensile stress (MPa)	
Original	1	32.79	35.40	8.0	Average 7.3	170.8	3.2	Average 3.0
	2	35.12	37.33	6.3		149.2	2.8	
	3	41.33	44.53	7.7		162.4	3.0	
Thermally treated	1	34.52	35.61	3.2	Average 3.4	170.0	3.2	Average 3.1
	2	34.72	35.97	3.6		164.2	3.0	
	3	61.87	64.02	3.5		170.0	3.2	
Crosslinked	1	45.76	48.30	5.6	Average 5.1	184.1	3.4	Average 3.3
	2	41.83	44.04	5.3		176.4	3.3	
	3	48.36	50.52	4.5		171.8	3.2	
Thermally treated and crosslinked	1	40.57	42.30	4.3	Average 4.9	168.6	3.1	Average 3.1
	2	36.64	38.84	6.0		165.0	3.1	
	3	42.04	43.86	4.3		163.4	3.0	

5.4 Conclusion

We have demonstrated the fabrication of PBI ultrafiltration hollow fiber membranes with highly chemical and mechanical stabilities from coagulation bath with various temperatures and post-thermal treatment at 300 °C. The fibers fabricated with coagulation bath at ambient temperature showed tight outer surface without visible pores observed by SEM imaging and spongy-type cross section. While the fibers spun from coagulation bath at 60 and 80 °C exhibited porous outer surface and finger-type cross section. The ultrafiltration data indicated MWCO of 70 kDa and mean pore size of 7.9 nm for fibers obtained from coagulation bath at 60 °C, while the fibers spun from coagulation bath at 80 °C exhibited MWCO of 145 kDa and mean pore size of 14.2 nm. The post-thermal treated fibers preserved their geometry and porous structures after soaking in hot NMP

solution, or directly dried from water, indicating excellent chemical and mechanical stabilities.

Chapter 6. Exfoliation of multi-layer MFI nanosheets

*To be submitted.

6.1 Introduction

The MFI nanosheets were originally produced by exfoliation of multilamellar MFI nanosheets in a melt-compounder with polystyrene. The polystyrene has a molecular weight of 45,000 and the processing temperatures were ranging from 120 to 200 °C.[21] However, the exfoliation yield was small. It was demonstrated that lower molecular weight polystyrene could promote the clay exfoliation and dispersion by melt compounding.[21] In this chapter, a low molecular weight polystyrene was used to improve the MFI nanosheet exfoliation yield. The exfoliation process was further studied with clay and polystyrenes with different molecular weights.

6.2 Experimental

6.2.1 Materials

Cloisite 20A (C20A), a natural Na-MMT modified by a dimethyldehydrogenated-tallow quaternary ammonium surfactant (cation exchange capacity = 95 miliequivalents per 100g) was purchased from Southern Clay Products, USA. Two polystyrene samples, denoted as PS13K and PS21k, were synthesized by anionic polymerization. A bimodal polystyrene (PSbi) was bought from Sigma-Aldrich (331651 ALDRICH), and a polystyrene oligomer was provided from Eastman (Piccolastic™ A75).

6.2.2 Exfoliation of multilamellar MFI and clay

Exfoliation of multilamellar MFI was studied with oligomer polystyrene (Piccolastic™ A75) in 15 ml melt compounder (Xplore® micro compounder MC15). Exfoliation

procedure is similar to that reported in Chapter 4. The powder zeolite and oligomer polystyrene (Piccolastic™ A75) were added into melt compounder at 85 °C with 4% zeolite loading. The desired temperature was set by the control panel and mixed for 1 h at 250 rpm. The temperature was controlled by occasionally flowing tap water when the desired temperature was lower than 80 °C.

Clay exfoliation with different polystyrenes was conducted in 5 ml melt compounder (Xplore® micro compounder MC5). The procedure is the same as zeolite exfoliation.

6.2.3 Characterization

Shear rheology of samples was investigated with a rheometer (ARES-2, TA Instruments). All tests were done under a nitrogen environment using 25 mm plates with a ~1 mm gap. Oligomer samples were characterized at 90 °C, all others were characterized at 150 °C. Samples were held at quiescent conditions for fifteen minutes prior to any measurements in order to minimize the deformation history associated with sample loading and to achieve an augmented rheological stability. Strain sweep experiments from 0.1 to 100% at 0.1 rad/s were then used to determine the linear viscoelastic region of each sample. All subsequent tests were conducted within this region of strain. Samples were allowed five minutes to recover after strain sweep experiments before frequency sweep from 100 to 0.01 rad/s was conducted. The complex viscosities of all virgin polymer materials were measured at 1 rad/s and 5% strain.

The MFI nanosheets and clay nanosheets were collected after dissolving the nanocomposite in toluene and washing with toluene.[36] TEM specimens were prepared by drop-casting the nanosheet suspension onto TEM grids (Ultrathin Carbon Film on Lacey

Carbon Support Film, 400 mesh Cu, product number: 01824, Ted Pella) and dried at ambient temperature overnight. TEM images were obtained using FEI Tecnai T12 at 120 kV.

6.3 Results and discussion

6.3.1 Exfoliation of multilamellar MFI

The exfoliation of layered materials relies on the diffusion of polymer and shear stress generated by the twin screws. Better diffusion and higher shear stress would result in higher exfoliation yield. At lower processing temperature, lower diffusion rate and higher shear stress (also viscosity) were expected. The final exfoliation yield would be a result of the combination of diffusion and shear stress.

The plateau value of elastic modulus (G') has been used as an indicator for exfoliation yield of clay by melt compounding with clay.[118] This method is much easier and could characterize the overall property of the sample, compared to the local characterization techniques such as TEM imaging. **Table 6.1** summarizes the processing temperature, speed, normal force during mixing, G' plateau value, and the nanosheet size (determined by TEM imaging) for 5 batches of nanocomposites obtained after melt compounding. With the increase of processing temperatures from 60 to 130 °C, the normal forces decreased from 3000 N to 60 N, which is the result of decreased viscosities and thus the shear stresses with the increase of processing temperatures. The G' plateau values also decreased as the increase of processing temperatures. Thus, the exfoliation yields also decreased. According to these results, the shear stress dominated the exfoliation yield, rather than the polymer diffusion in this case.

Table 6.1. Processing conditions, G' plateau values of nanocomposite, and nanosheet sizes.

Entry	Chamber T (°C)	Speed (rpm)	Force (N)	$G'_{plateau}$ (Pa)	Size of nanosheets (nm)
1	60 ~ 80	250	3000 ~ 2300	100	~500
2	85	250	910	10	~600
3	95	250	445	10	800~1000
4	95	50	200	0.1~1	~1000
5	130	250	80~60	0.1~10	>1000

The nanocomposite was then dissolved in toluene and washed with toluene 3 times. The obtained zeolite particles were examined by TEM imaging. As shown in **Figure 6.1**, the particle sizes increased with the increase of processing temperatures, which is the indication of particle breakdown by high shear stress during processing. Also, much more exfoliated single layer nanosheets and smaller amount of non-exfoliated big particles were observed at lower processing temperatures, indicating higher exfoliation yields at lower processing temperatures, which is consistent with the result from rheological characterization.

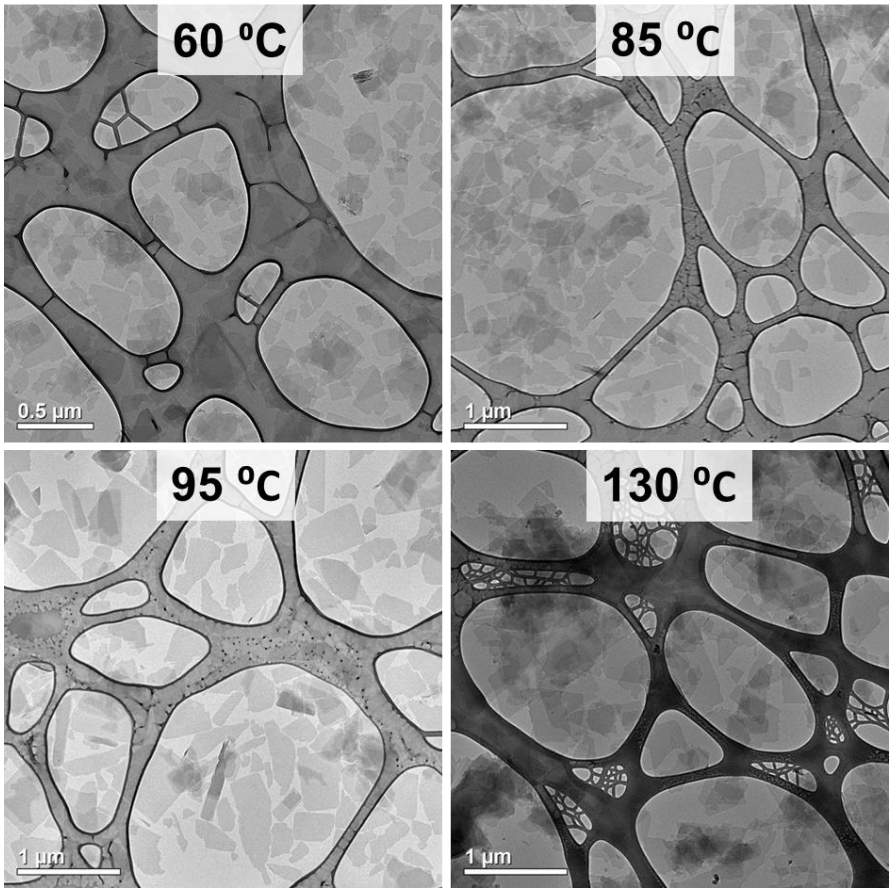

Figure 6.1. TEM images of the obtained exfoliated nanosheets at processing temperatures of 60, 85, 95, 130 °C.

The yield of exfoliated nanosheets could be estimated by coating a certain amount of nanosheet suspension onto porous alumina support. The nanosheet coating layer thickness, the volume of coating suspension, and the total volume of obtained nanosheet suspension after DGC purification could be used to calculate the total amount of purified nanosheets. The yield of exfoliated nanosheet after DGC purification was ~5%, when high molecular weight PS (45,000) was used. A yield of 16% was estimated when oligomeric PS was used at processing temperature of 60 °C, demonstrating the improved exfoliation. To further utilize the exfoliated nanosheets, the cake obtained after DGC

purification was recycled. After recycling for 6 times, the total yield increased to 35%.

6.3.2 Exfoliation of clay via polystyrene with various molecular weights

The multilamellar MFI zeolite has intergrown connections between the nanosheets due to the 90° rotational intergrowths of the MFI framework, which makes the exfoliation more complex. To further study and understand the melt compounding exfoliation process, commercially available clay particles are used, which have regular stacking of clay nanosheets. The effects of molecular weights of polystyrene, processing viscosities, and twin screws rotation speeds were explored.

Four polystyrenes, with molecular weights of 1.3k (Piccolastic™ A75, denoted as PS1.3K), 13k (synthesized by anionic polymerization, denoted as PS13K), 21k (synthesized by anionic polymerization, denoted as PS21K), and 35k (bought from Sigma-Aldrich, a mixture of 1.1k and 130k, denoted as PSbi), were used in the study. Their molecular weights were characterized by GPC and the results were listed in **Table 6.2** and **Figure 6.2**.

Table 6.2. Summary of the molecular weights from GPC

Polymer	Mn	Mw	Mp	PDI
PS1.3K	60	1252	884	1.9
PS13k	10111	12592	15334	1.2
PS21k	20022	22215	23437	1.1
PSbi*	59244	130160	104048	2.2
	743	1127	840	1.5

*PSbi has an overall Mw of 35k.

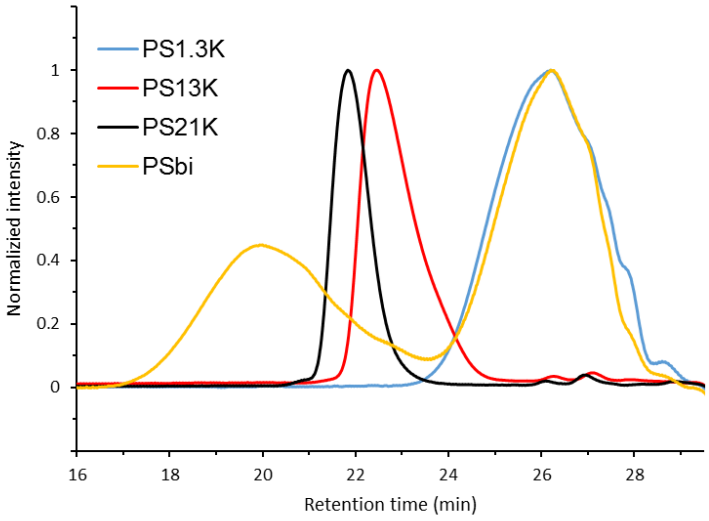

Figure 6.2. Representative GPC traces of PS1.3K, PS13K, PS21K, and PSbi.

According to the proposed mechanism for clay exfoliation during melt mixing, both shear stress and polymer diffusion play important roles for high yield exfoliation.[119] Here, inspired by previous research from Dr. Michail Dolgovskij,[118] constant viscosity mixing strategy was adopted to decouple the effects of shear stress and polymer diffusion. **Figure 6.3** shows the complex viscosity as a function of temperatures for PS1.3K, PS13K, PS21K, and PSbi at 5% strain and 1 rad/s. Mixing viscosities of 100, 1,000, and 10,000 Pa·s were selected and their corresponding mixing temperatures were summarized in **Table 6.3**. Clay loading for each melt compounding was 1% with 15 min processing time and 100 rpm rotation speed.

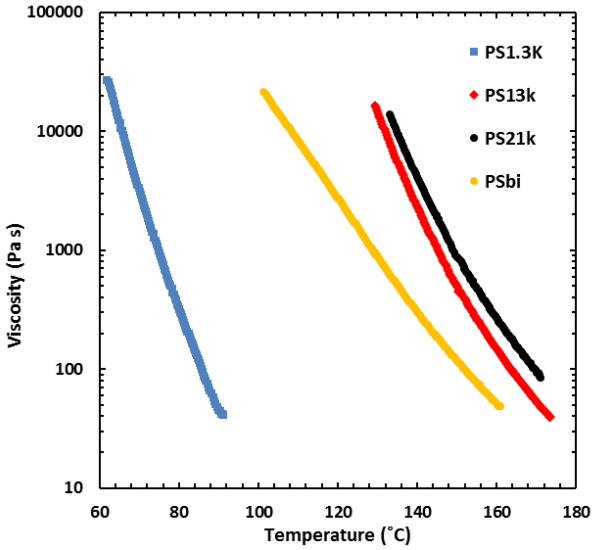

Figure 6.3. Complex viscosities for neat PS1.3K, PS13K, PS21K, and PSbi at 5% strain and 1 rad/s.

Table 6.3. Mixing conditions for PS1.3K, PS13K, PS21K, and PSbi.

Polymer	Viscosity (Pa·s)	Mixing temperature (°C)
PS1.3K	100	86
	1,000	75
	10,000	68
PS13K	100	164
	1,000	145
	10,000	132
PS21K	100	170
	1,000	149
	10,000	135
PSbi	100	152
	1,000	129
	10,000	108

Figure 6.4 showed G' vs. frequency curves for all blends processed with constant

viscosity mixing. For blends of PS1.3K and P13K, higher viscosities led to higher G' plateau, which indicated sufficient shear stress was required for exfoliation. For PS21K blends, however, their storage moduli were independent of mixing viscosities, possibly due to much lower diffusivities (because of higher molecular weight) at the mixing temperatures. On the other hand, for PSbi blends, the emergence of G' plateau only happened for blend from 10,000 Pa·s mixing, which was possibly due to the contribution from low molecular weight (1.1k) polystyrene for higher diffusivity.

The highest G' plateau value (indicating the highest exfoliation yield) was identified from the PS13K blend with processing viscosity of 10,000 Pa·s, which was possibly due to the best performance of combined high shear stress and diffusivity of PS13K processed at 132 °C. It is worth noting that the entanglement molecular weight for polystyrene is about 13,000.[120] Thus, we hypothesized that polystyrene with entanglement molecular weight (PS13K) has the best exfoliation yield compared with other molecular weight polystyrenes at the same mixing viscosity because combined high shear stress and diffusivity could be achieved at the same time. For polystyrene with molecular weights lower than 13,000, high mixing viscosity (which was required for sufficient shear stress) required much lower temperature which resulted in lower diffusivity and compromised the exfoliation performance. While for polystyrenes with molecular weights higher than 13,000 (for example, PS21K), the diffusion of polymer chains into the space between nanosheets was hindered, resulting in less or no exfoliation.

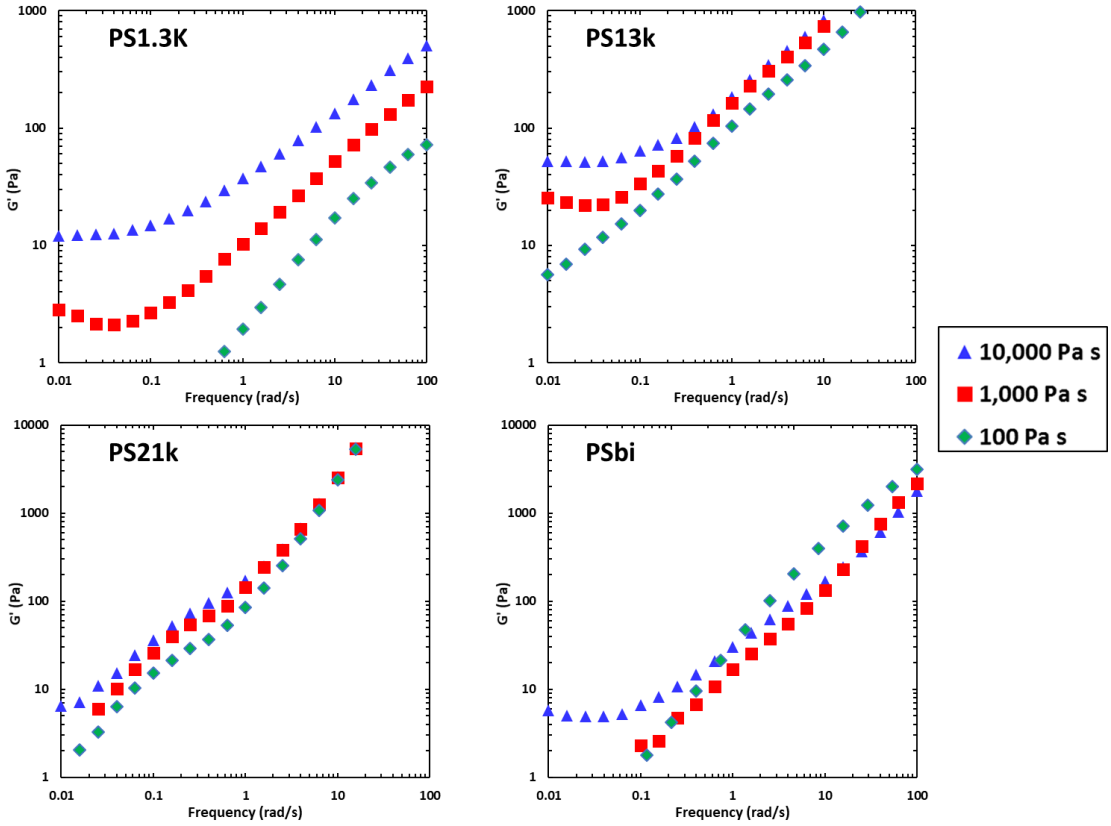

Figure 6.4. G' vs. frequency for the constant viscosity mixing. All blends were processed with 1% clay and 100 rpm for 15 min. Data for PS1.3K blends were measured at 90 °C. All others were measured at 150 °C.

The effects of mixing time were also studied for PS1.3K and PSbi blends. As shown in **Figure 6.5**, for PS1.3K, all the three blends showed G' plateau, whose values were enhanced significantly than those of blends after 15 min processing (**Figure 6.4**, PS1.3K). While for PSbi, the G' plateau was enhanced for 10,000 Pa·s blends and no emergence of G' plateau for other two blends.

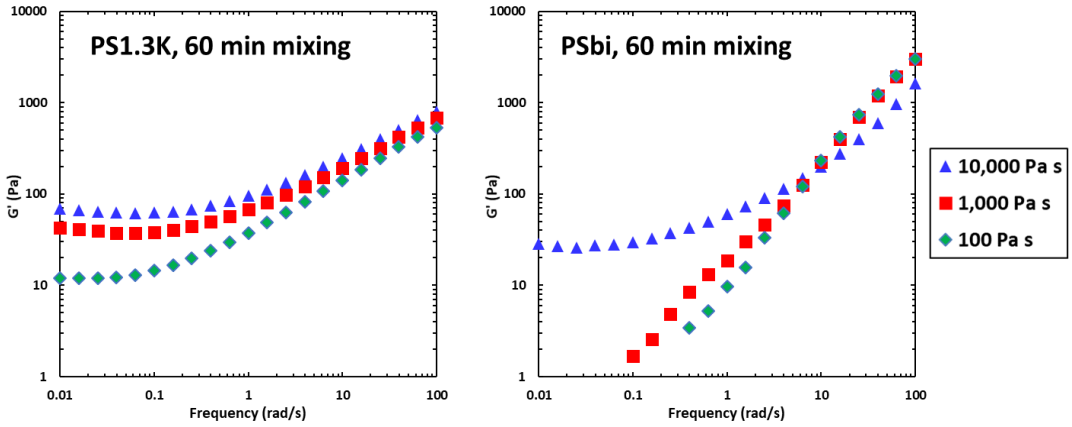

Figure 6.5. G' vs. frequency for the constant viscosity mixing. All blends were processed with 1% clay and 100 rpm for 60 min. Data for PS1.3K blends were measured at 90 °C. All others were measured at 150 °C.

Higher rotation speed of the twin screws also could enhance the exfoliation, as shown in **Figure 6.6** for PS1.3K blends. With viscosity of 100 Pa·s, G' plateau emerged when rotation speed increased to 200 and 300 rpm. For blends from processing viscosity of 10,000 Pa·s, rotation speeds of 200 and 300 rpm exhibited similar plateau values.

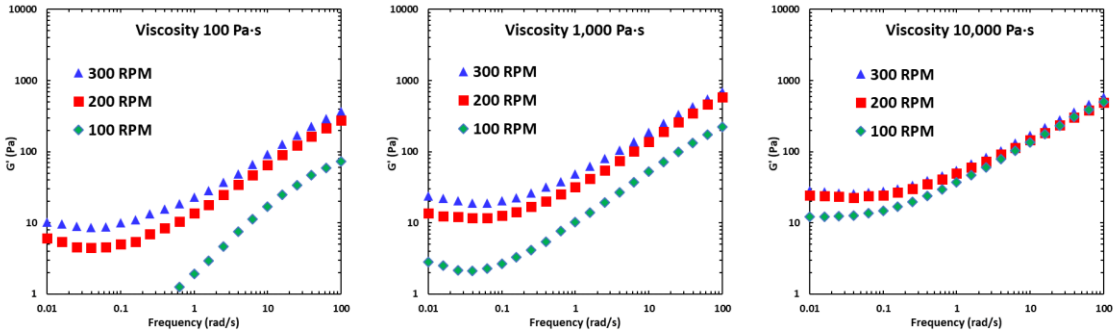

Figure 6.6. G' vs. frequency for the constant viscosity mixing with PS1.3K at various rotation speeds. All blends were processed with 1% clay for 60 min. Data were measured at 90 °C.

6.4 Conclusion

Oligomeric polystyrene (PS1.3K) was used to improve the exfoliation yield of

multilamellar MFI zeolite by melt compounding. The shear force, and thus the processing temperature dominated the exfoliation yield. Lower processing temperature resulted in higher exfoliation yield. A total exfoliation yield of 35% was obtained by recycling the cake after DGC purification. The exfoliation process was further studied with clay and various polystyrenes. The optimum molecular weight was found to be the entanglement molecular weight. Mixing viscosity, processing time, and rotation speed could enhance the final exfoliation yield.

Chapter 7. Final comments

Chapter 4 demonstrated a process for selective MFI membrane supported on polymer support without the need of secondary growth and detemplation. The simple deposit of open-pore MFI nanosheets exhibited butane isomer selectivity. This process provides a possible way for low cost and scalable MFI membranes.

Future work will focus on the improvement of membrane selectivity and permeance. Efforts should be made to purify the open-pore nanosheet suspension to remove un-exfoliated big particles. This could be achieved by a DGC purification step before piranha solution treatment, or by a filter with uniform pores as reported for graphene oxide purification.[121]

Another approach for selectivity improvement is defect sealing. High permeable polymer materials, such as polydimethylsiloxane (PDMS) and poly(1-trimethylsilyl-1-propyne) (PTMSP), could be considered for defect blocking. The surface of deposit or open-pore nanosheets probably requires modification by silane agents to increase the affinity between nanosheets and sealing polymers.

Hollow fiber membrane geometry has much higher surface to volume ratio, which is beneficial in industrial applications. Nanosheet coating onto polymer hollow fiber membranes will be studied. Efforts will focus on the condition for uniform coating, adhesion between polymer and nanosheet coating layer, long term stability, and membrane packing.

Bibliography

1. http://america.iza-structure.org/IZA-SC/ftc_table.php.
2. Cundy, C. S. & Cox, P. A. The Hydrothermal Synthesis of Zeolites : History and Development from the Earliest Days to the Present Time. *Chem. Rev.* **103,** 663–702 (2003).
3. Davis, M. E. Ordered porous materials for emerging applications. *Nature* **417,** 813–821 (2002).
4. Oak Ridge National Laboratory. *Materials for Separation Technologies: Energy and Emission Reduction Opportunities*. (2005).
5. Sholl, D. S. & Lively, R. P. Seven chemical separations to change the world. *Nature* **532,** 435–437 (2016).
6. Poshusta, J. C., Tuan, V. A., Falconer, J. L. & Noble, R. D. Synthesis and permeation properties of SAPO-34 tubular membranes. *Ind. Eng. Chem. Res.* **37,** 3924–3929 (1998).
7. Tomita, T., Nakayama, K. & Sakai, H. Gas separation characteristics of DDR type zeolite membrane. *Microporous Mesoporous Mater.* **68,** 71–75 (2004).
8. Zhou, M., Korelskiy, D., Ye, P., Grahn, M. & Hedlund, J. A uniformly oriented MFI membrane for improved CO2 separation. *Angew. Chemie - Int. Ed.* **53,** 3492–3495 (2014).
9. Choi, J. & Tsapatsis, M. MCM-22/silica selective flake nanocomposite membranes for hydrogen separations. *J. Am. Chem. Soc.* **132,** 448–449 (2010).
10. Wirawan, S. K. *et al.* H2/CO2 permeation through a silicalite-1 composite membrane. *J. Membr. Sci.* **375,** 313–322 (2011).
11. Sebastián, V. *et al.* A new titanosilicate umbite membrane for the separation of H2. *Chem. Commun.* 3036–3037 (2005).
12. Tuan, V. A., Falconer, J. L. & Noble, R. D. Isomorphous substitution of Al, Fe, B, and Ge into MFI-zeolite membranes. *Microporous Mesoporous Mater.* **41,** 269–280 (2000).
13. Agrawal, K. V. *et al.* Oriented MFI Membranes by Gel-Less Secondary Growth of Sub-100 nm MFI-Nanosheet Seed Layers. *Adv. Mater.* **27,** 3243–3249 (2015).
14. Coronas, J., Falconer, J. L. & Noble, R. D. Characterization and permeation properties of ZSM-5 tubular membranes. *Aiche J.* **43,** 1797–1812 (1997).
15. Xomeritakis, G., Nair, S. & Tsapatsis, M. Transport properties of alumina-supported MFI membranes made by secondary (seeded) growth. *Microporous Mesoporous Mater.* **38,** 61–73 (2000).
16. Bowen, T. C., Noble, R. D. & Falconer, J. L. Fundamentals and applications of pervaporation through zeolite membranes. *J. Membr. Sci.* **245,** 1–33 (2004).
17. Wee, S.-L., Tye, C.-T. & Bhatia, S. Membrane separation process—Pervaporation through zeolite membrane. *Sep. Purif. Technol.* **63,** 500–516 (2008).
18. Elyassi, B. *et al.* Ethanol/water mixture pervaporation performance of b -oriented silicalite-1 membranes made by gel-free secondary growth. *AIChE J.* **62,** 556–563 (2016).
19. Korelskiy, D. *et al.* High flux MFI membranes for pervaporation. *J. Membr. Sci.*

427, 381–389 (2013).
20. Lai, Z. *et al.* Microstructural optimization of a zeolite membrane for organic vapor separation. *Science* **300,** 456–460 (2003).
21. Varoon, K. *et al.* Dispersible Exfoliated Zeolite Nanosheets and Their Application as a Selective Membrane. *Science* **334,** 72–75 (2011).
22. Pham, T. C. T., Kim, H. S. & Yoon, K. B. Growth of Uniformly Oriented Silica MFI and BEA Zeolite Films on Substrates. *Science* **334,** 1533–1538 (2011).
23. Snyder, M. & Tsapatsis, M. Hierarchical Nanomanufacturing: From Shaped Zeolite Nanoparticles to High-Performance Separation Membranes. *Angew. Chemie Int. Ed.* **46,** 7560–7573 (2007).
24. Bonilla, G. *et al.* Zeolite (MFI) Crystal Morphology Control Using Organic Structure-Directing Agents. *Chem. Mater.* **16,** 5697–5705 (2004).
25. Fan, W. *et al.* Hierarchical nanofabrication of microporous crystals with ordered mesoporosity. *Nat. Mater.* **7,** 984–991 (2008).
26. Lee, P. *et al.* Sub-40 nm Zeolite Suspensions via Disassembly of Three-Dimensionally Ordered Mesoporous-Imprinted Silicalite-1. *J. Am. Chem. Soc.* **133,** 493–502 (2011).
27. Maheshwari, S. *et al.* Layer Structure Preservation during Swelling, Pillaring, and Exfoliation of a Zeolite Precursor. *J. Am. Chem. Soc.* **130,** 1507–1516 (2008).
28. Zhang, H. *et al.* Open-Pore Two-Dimensional MFI Zeolite Nanosheets for the Fabrication of Hydrocarbon-Isomer-Selective Membranes on Porous Polymer Supports. *Angew. Chemie Int. Ed.* **55,** 7184–7187 (2016).
29. Yoon, K. B. Organization of zeolite microcrystals for production of functional materials. *Acc. Chem. Res.* **40,** 29–40 (2007).
30. Wee, L. H. *et al.* Silicalite-1 films with preferred orientation. *Microporous Mesoporous Mater.* **116,** 22–27 (2008).
31. Rangnekar, N. *et al.* 2D zeolite coatings: Langmuir-Schaefer deposition of 3 nm thick MFI zeolite nanosheets. *Angew. Chemie Int. Ed.* **54,** 6571–6575 (2015).
32. Kulak, A., Lee, Y.-J., Park, Y. S. & Yoon, K. B. Orientation-Controlled Monolayer Assembly of Zeolite Crystals on Glass and Mica by Covalent Linkage of Surface-Bound Epoxide and Amine Groups. *Angew. Chemie Int. Ed.* **39,** 950–953 (2000).
33. Li, X., Peng, Y., Wang, Z. & Yan, Y. Synthesis of highly b-oriented zeolite MFI films by suppressing twin crystal growth during the secondary growth. *CrystEngComm* **13,** 3657–3660 (2011).
34. Pham, T. C. T., Nguyen, T. H. & Yoon, K. B. Gel-Free Secondary Growth of Uniformly Oriented Silica MFI Zeolite Films and Application for Xylene Separation. *Angew. Chemie Int. Ed.* **52,** 8693–8698 (2013).
35. Choi, M. *et al.* Stable single-unit-cell nanosheets of zeolite MFI as active and long-lived catalysts. *Nature* **461,** 246–249 (2009).
36. Agrawal, K. V. *et al.* Solution-processable exfoliated zeolite nanosheets purified by density gradient centrifugation. *AIChE J.* **59,** 3458–3467 (2013).
37. Ishikawa, A., Chiang, T. H. & Toda, F. Separation of water–alcohol mixtures by permeation through a zeolite membrane on porous glass. *J. Chem. Sociaty, Chem.*

Commun. 764–765 (1989). doi:10.1039/C39890000764
38. Morigami, Y., Kondo, M., Abe, J., Kita, H. & Okamoto, K. The first large-scale pervaporation plant using tubular-type module with zeolite NaA membrane. *Sep. Purif. Technol.* **25,** 251–260 (2001).
39. Sato, K. & Nakane, T. A high reproducible fabrication method for industrial production of high flux NaA zeolite membrane. *J. Membr. Sci.* **301,** 151–161 (2007).
40. Sato, K., Sugimoto, K. & Nakane, T. Mass-production of tubular NaY zeolite membranes for industrial purpose and their application to ethanol dehydration by vapor permeation. *J. Membr. Sci.* **319,** 244–255 (2008).
41. Sato, K., Sugimoto, K. & Nakane, T. Synthesis of industrial scale NaY zeolite membranes and ethanol permeating performance in pervaporation and vapor permeation up to 130?C and 570kPa. *J. Membr. Sci.* **310,** 161–173 (2008).
42. Gascon, J. *et al.* Practical Approach to Zeolitic Membranes and Coatings: State of the Art, Opportunities, Barriers, and Future Perspectives. *Chem. Mater.* **24,** 2829–2844 (2012).
43. Caro, J., Noack, M., Kölsch, P. & Schäfer, R. Zeolite membranes – state of their development and perspective. *Microporous Mesoporous Mater.* **38,** 3–24 (2000).
44. Lin, Y. S., Kumakiri, I., Nair, B. N. & Alsyouri, H. Microporous inorganic membranes. *Sep. Purif. Methods* **31,** 229–379 (2002).
45. Morigami, Y., Kondo, M., Abe, J., Kita, H. & Okamoto, K. The first large-scale pervaporation plant using tubular-type module with zeolite NaA membrane. *Sep. Purif. Technol.* **25,** 251–260 (2001).
46. Jirka, I., Sazama, P., Zikánová, a., Hrabánek, P. & Kocirik, M. Low-temperature thermal removal of template from high silica ZSM-5. Catalytic effect of zeolitic framework. *Microporous Mesoporous Mater.* **137,** 8–17 (2011).
47. Li, Q., Amweg, M. L., Yee, C. K., Navrotsky, A. & Parikh, A. N. Photochemical template removal and spatial patterning of zeolite MFI thin films using UV/ozone treatment. *Microporous Mesoporous Mater.* **87,** 45–51 (2005).
48. Parikh, A. N. *et al.* Non-thermal calcination by ultraviolet irradiation in the synthesis of microporous materials. *Microporous Mesoporous Mater.* **76,** 17–22 (2004).
49. Zhao, J. *et al.* Highly selective zeolite membranes as explosive preconcentrators. *Anal. Chem.* **84,** 6303–6307 (2012).
50. Stöber, W., Fink, A. & Bohn, E. Controlled growth of monodisperse silica spheres in the micron size range. *J. Colloid Interface Sci.* **26,** 62–69 (1968).
51. Choi, J., Ghosh, S., King, L. & Tsapatsis, M. MFI zeolite membranes from a- and randomly oriented monolayers. *Adsorption* **12,** 339–360 (2006).
52. Ge, Q., Wang, Z. & Yan, Y. High-Performance Zeolite NaA Membranes on Polymer?Zeolite Composite Hollow Fiber Supports. *J. Am. Chem. Soc.* **131,** 17056–17057 (2009).
53. Wang, B. *et al.* Rapid synthesis of faujasite/polyethersulfone composite membrane and application for CO 2 /N 2 separation. *Microporous Mesoporous Mater.* **208,** 72–82 (2015).

54. Wu, Z., Wu, D., Yang, W. & Jin, R. Preparation of highly reflective and conductive metallized polyimide films through surface modification: processing, morphology and properties. *J. Mater. Chem.* **16,** 310–316 (2006).
55. Díaz, U. & Corma, A. Layered zeolitic materials: an approach to designing versatile functional solids. *Dalt. Trans.* **43,** 10292–10316 (2014).
56. Tsapatsis, M. 2-Dimensional zeolites. *AIChE J.* **60,** 2374–2381 (2014).
57. Kim, W. G. & Nair, S. Membranes from nanoporous 1D and 2D materials: A review of opportunities, developments, and challenges. *Chem. Eng. Sci.* **104,** 908–924 (2013).
58. Na, K., Park, W., Seo, Y. & Ryoo, R. Disordered assembly of MFI zeolite nanosheets with a large volume of intersheet mesopores. *Chem. Mater.* **23,** 1273–1279 (2011).
59. Messinger, R. J., Na, K., Seo, Y., Ryoo, R. & Chmelka, B. F. Co-development of crystalline and mesoscopic order in mesostructured zeolite nanosheets. *Angew. Chemie Int. Ed.* **54,** 927–931 (2015).
60. Na, K. *et al.* Pillared MFI zeolite nanosheets of a single-unit-cell thickness. *J. Am. Chem. Soc.* **132,** 4169–4177 (2010).
61. Nicolosi, V., Chhowalla, M., Kanatzidis, M. G., Strano, M. S. & Coleman, J. N. Liquid exfoliation of layered materials. *Science* **340,** 1226419 (2013).
62. Han, J. T. *et al.* Extremely efficient liquid exfoliation and dispersion of layered materials by unusual acoustic cavitation. *Sci. Rep.* **4,** 5133 (2014).
63. Coleman, J. N. *et al.* Two-dimensional nanosheets produced by liquid exfoliation of layered materials. *Science* **331,** 568–571 (2011).
64. Ogino, I., Yokoyama, Y. & Mukai, S. R. Sonication-free exfoliation of graphite oxide via rapid phase change of water. *Top. Catal.* **58,** 522–528 (2015).
65. Chalasani, R., Gupta, A. & Vasudevan, S. Engineering new layered solids from exfoliated inorganics: a periodically alternating hydrotalcite - montmorillonite layered hybrid. *Sci. Rep.* **3,** 3498 (2013).
66. Srivastava, S. & Kotov, N. A. Composite layer-by-layer (LBL) assembly with inorganic nanoparticles and nanowires. *Acc. Chem. Res.* **41,** 1831–1841 (2008).
67. Priolo, M. A., Holder, K. M., Guin, T. & Grunlan, J. C. Recent advances in gas barrier thin films via layer-by-layer assembly of polymers and platelets. *Macromol. Rapid Commun.* **36,** 866–879 (2015).
68. Corma, A., Díaz, U., García, T., Sastre, G. & Velty, A. Multifunctional hybrid organic−inorganic catalytic materials with a hierarchical system of well-defined micro- and mesopores. *J. Am. Chem. Soc.* **132,** 15011–15021 (2010).
69. Varoon, K. *et al.* Dispersible exfoliated zeolite nanosheets and their application as a selective membrane. *Science* **334,** 72–75 (2011).
70. Kumar, P., Agrawal, K. V., Tsapatsis, M. & Mkhoyan, K. A. Quantification of thickness and wrinkling of exfoliated two-dimensional zeolite nanosheets. *Nat. Commun.* **6,** 7128 (2015).
71. Zhang, X. *et al.* Synthesis of self-pillared zeolite nanosheets by repetitive branching. *Science* **336,** 1684–1687 (2012).
72. Agrawal, K. V. *et al.* Oriented MFI membranes by gel-less secondary growth of

sub-100 nm MFI-nanosheet seed layers. *Adv. Mater.* **27,** 3243–3249 (2015).
73. Kim, H. W. *et al.* Selective gas transport through few-layered graphene and graphene oxide membranes. *Science* **342,** 91–95 (2013).
74. Li, H. *et al.* Ultrathin, molecular-sieving graphene oxide membranes for selective hydrogen separation. *Science* **342,** 95–98 (2013).
75. Peng, Y. *et al.* Metal-organic framework nanosheets as building blocks for molecular sieving membranes. *Science* **346,** 1356–1359 (2014).
76. Brown, A. J. *et al.* Interfacial microfluidic processing of metal-organic framework hollow fiber membranes. *Science* **345,** 72–75 (2014).
77. Rodenas, T. *et al.* Metal–organic framework nanosheets in polymer composite materials for gas separation. *Nat. Mater.* **14,** 48–55 (2015).
78. Vogel, H. & Marvel, C. S. Polybenzimidazoles, new thermally stable polymers. *J. Polym. Sci.* **50,** 511–539 (1961).
79. Model, F. S. & Lee, L. A. in *Reverse Osmosis Membrane Research, Ed. by H. K. Londale and H. E. Podall* 285 (Plenum Press, New York, 1972).
80. Brinegar, W. Reverse osmosis process employing polybenzimidazole membranes. U.S. Patent 3,720,607. (1973).
81. Ram, M. Process for forming hollow polybenzimidazole filaments for reverse osmosis applications. U. S. Patent 3,851,025. (1974).
82. Belohlav, L. R. Polybenzimidazole. *Die Angew. Makromol. Chemie* **40,** 465–483 (1974).
83. Sawyer, L. C. & Jones, R. S. Observations on the structure of first generation polybenzimidazole reverse osmosis membranes. **20,** 147–166 (1984).
84. Wainright, J. S., Wang, J.-T., Weng, D., Savinell, R. F. & Litt, M. Acid-Doped Polybenzimidazoles: A New Polymer Electrolyte. *J. Electrochem. Soc.* **142,** L121-123 (1995).
85. Jones, D. J. & Rozière, J. Recent advances in the functionalisation of polybenzimidazole and polyetherketone for fuel cell applications. *J. Membr. Sci.* **185,** 41–58 (2001).
86. Mecerreyes, D. *et al.* Porous Polybenzimidazole Membranes Doped with Phosphoric Acid: Highly Proton-Conducting Solid Electrolytes. *Chem. Mater.* **16,** 604–607 (2004).
87. Li, Q., He, R., Jensen, J. O. & Bjerrum, N. J. PBI-Based Polymer Membranes for High Temperature Fuel Cells – Preparation, Characterization and Fuel Cell Demonstration. *Fuel Cells* **4,** 147–159 (2004).
88. Asensio, J. A. & Gómez-Romero, P. Recent Developments on Proton Conduc-ting Poly(2,5-benzimidazole) (ABPBI) Membranes for High Temperature Polymer Electrolyte Membrane Fuel Cells. *Fuel Cells* **5,** 336–343 (2005).
89. Li, Q., Jensen, J. O., Savinell, R. F. & Bjerrum, N. J. High temperature proton exchange membranes based on polybenzimidazoles for fuel cells. *Prog. Polym. Sci.* **34,** 449–477 (2009).
90. Wang, K. Y. & Chung, T.-S. Polybenzimidazole nanofiltration hollow fiber for cephalexin separation. *AIChE J.* **52,** 1363–1377 (2006).
91. Wang, K. Y., Xiao, Y. & Chung, T. S. Chemically modified polybenzimidazole

nanofiltration membrane for the separation of electrolytes and cephalexin. *Chem. Eng. Sci.* **61,** 5807–5817 (2006).
92. Wang, K. Y. & Chung, T. S. Fabrication of polybenzimidazole (PBI) nanofiltration hollow fiber membranes for removal of chromate. *J. Membr. Sci.* **281,** 307–315 (2006).
93. Wang, K. Y., Chung, T. S. & Rajagopalan, R. Novel polybenzimidazole (PBI) nanofiltration membranes for the separation of sulfate and chromate from high alkalinity brine to facilitate the chlor-alkali process. *Ind. Eng. Chem. Res.* **46,** 1572–1577 (2007).
94. Xing, D. Y., Chan, S. Y. & Chung, T.-S. The ionic liquid [EMIM]OAc as a solvent to fabricate stable polybenzimidazole membranes for organic solvent nanofiltration. *Green Chem.* **16,** 1383–1392 (2014).
95. Valtcheva, I. B., Kumbharkar, S. C., Kim, J. F., Bhole, Y. & Livingston, A. G. Beyond polyimide: Crosslinked polybenzimidazole membranes for organic solvent nanofiltration (OSN) in harsh environments. *J. Membr. Sci.* **457,** 62–72 (2014).
96. Chen, D., Yu, S., Zhang, H. & Li, X. Solvent resistant nanofiltration membrane based on polybenzimidazole. *Sep. Purif. Technol.* **142,** 299–306 (2015).
97. Wang, K. Y., Chung, T. S. & Qin, J. J. Polybenzimidazole (PBI) nanofiltration hollow fiber membranes applied in forward osmosis process. *J. Membr. Sci.* **300,** 6–12 (2007).
98. Wang, K. Y., Yang, Q., Chung, T. S. & Rajagopalan, R. Enhanced forward osmosis from chemically modified polybenzimidazole (PBI) nanofiltration hollow fiber membranes with a thin wall. *Chem. Eng. Sci.* **64,** 1577–1584 (2009).
99. Wang, Y., Gruender, M. & Chung, T. S. Pervaporation dehydration of ethylene glycol through polybenzimidazole (PBI)-based membranes. 1. Membrane fabrication. *J. Membr. Sci.* **363,** 149–159 (2010).
100. Han, Y. J., Wang, K. H., Lai, J. Y. & Liu, Y. L. Hydrophilic chitosan-modified polybenzoimidazole membranes for pervaporation dehydration of isopropanol aqueous solutions. *J. Membr. Sci.* **463,** 17–23 (2014).
101. Wang, Y., Gruender, M. & Xu, S. Polybenzimidazole (PBI) Membranes for Phenol Dehydration via Pervaporation. *Ind. Eng. Chem. Res.* **53,** 18291–18303 (2014).
102. Han, Y. J., Su, W. C., Lai, J. Y. & Liu, Y. L. Hydrophilically surface-modified and crosslinked polybenzimidazole membranes for pervaporation dehydration on tetrahydrofuran aqueous solutions. *J. Membr. Sci.* **475,** 496–503 (2015).
103. Wang, Y., Chung, T. S., Neo, B. W. & Gruender, M. Processing and engineering of pervaporation dehydration of ethylene glycol via dual-layer polybenzimidazole (PBI)/polyetherimide (PEI) membranes. *J. Membr. Sci.* **378,** 339–350 (2011).
104. Shi, G. M., Wang, Y. & Chung, T.-S. Dual-layer PBI/P84 hollow fibers for pervaporation dehydration of acetone. *AIChE J.* **58,** 1133–1145 (2012).
105. Kumbharkar, S. C., Karadkar, P. B. & Kharul, U. K. Enhancement of gas permeation properties of polybenzimidazoles by systematic structure architecture. *J. Membr. Sci.* **286,** 161–169 (2006).
106. Hosseini, S. S. & Chung, T. S. Carbon membranes from blends of PBI and

polyimides for N2/CH4 and CO2/CH4 separation and hydrogen purification. *J. Membr. Sci.* **328,** 174–185 (2009).
107. Hosseini, S. S., Peng, N. & Chung, T. S. Gas separation membranes developed through integration of polymer blending and dual-layer hollow fiber spinning process for hydrogen and natural gas enrichments. *J. Membr. Sci.* **349,** 156–166 (2010).
108. Kumbharkar, S. C., Liu, Y. & Li, K. High performance polybenzimidazole based asymmetric hollow fibre membranes for H2/CO2 separation. *J. Membr. Sci.* **375,** 231–240 (2011).
109. Ullah, R. *et al.* Synthesis, characterization and evaluation of porous polybenzimidazole materials for CO2 adsorption at high pressures. *Adsorption* **22,** 247–260 (2016).
110. Sansone, M. J. Process for the production of polybenzimidazole ultrafiltration membranes U.S. Patent 4693824. (1985).
111. Xing, D. Y., Chan, S. Y. & Chung, T.-S. Molecular interactions between polybenzimidazole and [EMIM]OAc, and derived ultrafiltration membranes for protein separation. *Green Chem.* **14,** 1405–1412 (2012).
112. Bhagat, D., Mule, B., Mandlekar, N., Pandare, K. & Kharul, U. PBI-BuI and PAN-PSSALi based UF membranes: Effects of solute and membrane surface interactions on rejection and flux. *Desalination* **333,** 45–51 (2014).
113. Barss, R. P. *et al.* Solvent-resistant microporous polybenzimidazole membranes U.S. Patent 6623639. (1999).
114. Omole, I. C. Crosslinked polyimide hollow fiber membranes for aggressive natural gas feed streams. Dissertation. Georgia Tech. (2008).
115. Michaels, A. S. Analysis and Prediction of Sieving Curves for Ultrafiltration Membranes: A Universal Correlation? *Sep. Sci. Technol.* **15,** 1305–1322 (1980).
116. Singh, S., Khulbe, K. C., Matsuura, T. & Ramamurthy, P. Membrane characterization by solute transport and atomic force microscopy. *J. Membr. Sci.* **142,** 111–127 (1998).
117. Khayet, M., Feng, C. Y., Khulbe, K. C. & Matsuura, T. Preparation and characterization of polyvinylidene fluoride hollow fiber membranes for ultrafiltration. *Polymer* **43,** 3879–3890 (2002).
118. Dolgovskij, M. K. Dispersing layered silicates in polymer melts: using melt rheology to determine dispersion. University of Minnesota, 2007.
119. Fornes, T. D., Yoon, P. J., Keskkula, H. & Paul, D. R. Nylon 6 nanocomposites : the effect of matrix molecular weight. *Polymer* **42,** 09929–09940 (2001).
120. Fetters, L. J., Lohse, D. J., Richter, D., Witten, T. A. & Zirkel, A. Macromolecules. *Macromolecules* **27,** 4639–4647 (1994).
121. Chen, J. *et al.* Size Fractionation of Graphene Oxide Sheets via Filtration through Track-Etched Membranes. *Adv. Mater.* **27,** 3654–3660 (2015).